Interacting Dark Matter: Decay and Bremsstrahlung Processes

Ahmad Jacob Galea

Submitted in total fulfilment of the requirements

of the degree of Doctor of Philosophy

February 2013

School of Physics

The University of Melbourne

Abstract

Though there is substantial indirect astrophysical evidence for the existence of dark matter (DM), it has yet to be directly detected. Consequently, little is known about its internal structure. It is possible that there is a small but finite non-gravitational interaction between dark matter and the Standard Model (SM) which may have observable consequences. The purpose of this thesis is the exploration of some of these interactions and consequences. In particular we consider the possibility that dark matter is unstable on long timescales, as motivated by discrepancies between simulation and observation of structure on sub-galactic scales. We also consider the consequences of electroweak radiative corrections to annihilation processes involving dark matter, as such corrections are necessarily present in many well motivated models. We consider this possibility in the contexts of dark matter annihilation in galactic halos, and production in colliders.

Chapter 1 provides an introduction to dark matter, including some of its astrophysical and particle aspects. As a motivation for the following sections, we begin by briefly outlining some of the observational evidence for dark matter. We go on to discuss structure formation, and the cold dark matter distribution on galactic scales. Next we discuss the possibility of non-gravitational interactions involving dark matter, including decay, annihilation, scattering off nuclei, and production. Finally we discuss the determination of the relic abundance in the early Universe, including a discussion of models involving coannihilation.

Late decaying dark matter has been proposed as a solution to the small scale

structure problems inherent to cold dark matter cosmology. In these models the parent dark matter particle is unstable, and decays into a daughter with near degenerate mass, plus a relativistic final state. In Chapter 2 we review the observational constraints on decaying dark matter, and construct explicit particle physics models to realize this scenario. To achieve this, we introduce a pair of fermionic dark matter candidates and a new scalar field, which obey either a $\mathbb{Z}_4$, or a $U(1)$ symmetry. Through the spontaneous breaking of these symmetries, and coupling of the new fields to standard model particles, we demonstrate that the desired decay process may be obtained. We also discuss the dark matter production processes in these models.

In Chapter 3 we investigate electroweak radiative corrections to dark matter annihilation into leptons, in which a W or Z boson is also radiated. In many dark matter models the annihilation rate into fermions is helicity suppressed. We demonstrate that bremsstrahlung processes can remove this helicity suppression, causing the branching ratios Br($\ell\nu W$), Br($\ell^+\ell^- Z$), and Br($\bar{\nu}\nu Z$) to dominate over Br($\ell^+\ell^-$) and Br($\bar{\nu}\nu$). We find this effect to be most significant in the limit where the dark matter mass is nearly degenerate with the mass of the boson which mediates the annihilation process.

Finally, in Chapter 4, we investigate a mono-Z process as a potential dark matter search strategy at the Large Hadron Collider (LHC). In this channel a single Z boson recoils against missing transverse momentum attributed to dark matter particles, χ, which escape the detector. For illustrative purposes we consider the process $q\bar{q} \to \chi\chi Z$ in a toy dark matter model, where the Z boson is emitted from either the initial state quarks, or from the internal propagator. We look for muonic decays of the Z, showing the Standard Model backgrounds to this process to be easily removable with modest selection cuts. We compare signal with Standard Model backgrounds and demonstrate that there exist regions of parameter space

where the signal may be clearly visible above background in future LHC data.

Parts of this thesis have been published in the references that can be found in the 'Publications' section at the end of the thesis.

Declaration

This is to certify that:

(i) the thesis comprises of my original work towards the PhD except where indicated in the Preface,

(ii) due acknowledgement has been made in the text to all other material used,

(iii) the thesis is less that 100,000 words in length, exclusive of tables, maps, bibliographies, appendices and footnotes.

Ahmad Jacob Galea

Date:

Preface

This thesis is comprised of five main chapters (not including supplementary material such as the bibliography). Chapter 1 is an original literature review. Chapter 2 is based on Publications 1 and 2, Chapters 3 and 4 are based on Publications 3 and 4 respectively. Chapter 5 is the conclusion.

These publications were done in collaboration with Nicole F. Bell (Publications 1, 2, 3 & 4), James B. Dent (Publications 3 & 4), Thomas D. Jacques (Publications 3 & 4), Lawrence M. Krauss (Publications 3 & 4), Kallia Petraki (Publication 1), Raymond R. Volkas (Publication 2), and Thomas J. Weiler (Publications 3 & 4). While N. Bell, J. Dent, L. Krauss and T. Weiler are responsible for the original inspiration for many of these projects, all calculations, results, and analyses presented within this thesis are my own work unless stated otherwise, with the exception of Section 2.2.2 which contains reference to work by Kallia Petraki, Section 3.2.2 which is work done by Thomas J. Weiler, and the constraints in Section 4.3.2, which are the work of James B. Dent and Thomas D. Jacques.

Acknowledgements

My sincerest gratitude goes to my supervisor Nicole Bell, for her guidance and patience, and for giving me the opportunity to work on such interesting projects. I have been fortunate to learn from one who holds such a high standard in research and collaboration. Similarly, I would like to thank our collaborators, James B. Dent, Thomas D. Jacques, Lawrence M. Krauss, Kallia Petraki, Raymond R. Volkas, and Thomas J. Weiler. It has been a great pleasure to work with and learn from you all, and I look forward to continuing collaboration into the future. To my advisory panel including Raymond Volkas and Andrew Greentree, thank you for your valuable perspective and advice. I would like to thank all those whose advice made this work a success, namely, F. Melia, J. Beacom, H. Yuksel, M. Drewes, E. Barberio, B. Dutta, T. Kamon, M. White, A. Limosani and N. Setzer among others. Many thanks to The Center of Excellence for Particle Physics at the Terascale (CoEPP) for providing an environment conducive to cross collaboration between theory and experiment, and thanks to all those within the center who have lent support and advice throughout my Ph.D. Last but not least, I would like to thank my family, for all of your love and support. Without you I would not be where I am today.

Contents

List of Figures

1

Introduction to Dark Matter

In this chapter we give some background to this project. We will also introduce some calculation techniques key to enabling an understanding of the latter chapters.

In Section 1.1 we outline some important astrophysical concepts, and discuss the evidence for dark matter and its structure on extra galactic and galactic scales. In Section 1.2 we discuss the possibility that dark matter has non gravitational interactions, and possible ways of constraining those interactions. Finally, in Section 1.3 we consider the production of dark matter in the early Universe, and perform an explicit calculation of the abundance of a thermal relic.

1.1 Dark Matter: Evidence and Structure

In this section we will outline some of the astrophysical foundations of dark matter. Section 1.1.1 pertains to some of the experimental motivations for dark matter. In Section 1.1.2 we discuss the formation of structure on intermediate scales, with the consequent distribution of dark matter within galaxies outlined in Section 1.1.3.

1.1.1 Evidence for Dark Matter

Galactic Rotation Curves

The first, and one of the most compelling, pieces of evidence for the existence of dark matter is the measurement of the rotation curves of nearby galaxies. If luminous matter, that is, stars and interstellar gas, were to constitute the entirety of galactic mass, the brightness of a galaxy should be indicative of the mass contained within. This should in turn lead to an accurate prediction of the angular velocity of material as a function of radius from the galactic center. Observations, however, show a much slower radial decrease in angular velocity than expected. This can be clearly seen in Fig. 1.1 which displays a composite rotation curve created from a large scale galactic survey [1]. This discrepancy indicates either a breakdown in gravitational theory on galactic scales, or the presence of a large quantity of invisible mass. Good agreement can be found between theory and observation if the galactic disc resides inside a sphere (halo) of matter which only interacts gravitationally with visible matter, as demonstrated in Fig. 1.1.

Merger Events

The previous evidence, while compelling, is not alone, enough to justify the existence of dark matter over a modification of gravity on galactic scales. In order for dark matter to be an appealing model, its effects need to be observed over a wide range of length scales. To this end, one can look to clusters of galaxies, and specifically at merger events. The majority of the visible matter in galactic clusters is in the form of intergalactic gas, which readily interacts in a merger event, emitting in the X-ray. A prime example of this can be seen object 1E0657-558 [10], otherwise known as the Bullet cluster merger. A composite image of visible light [2],

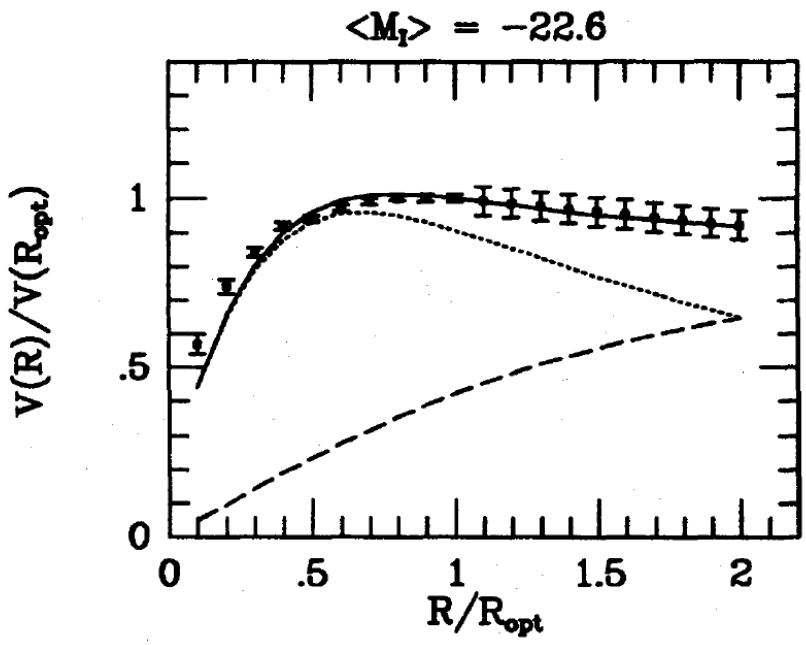

Figure 1.1: Observed rotation curve (points), alongside expected velocity profile without dark matter (dotted), profile for dark matter alone (dashed), and combined expected profile (solid) [1].

X-rays [3], and a lensing map [2] can be found in Fig. 1.2. The intergalactic gas interacts and produces a shock front, as is clear from the red contribution to Fig. 1.2. Gravitational lensing of background galaxies can be used to determine the location of the bulk of the mass in the clusters, as indicated in blue in Fig. 1.2. The dominant fraction of the mass in the clusters is clearly following the galaxies, and is separated from the intergalactic gas. It is very difficult to modify Newtonian gravity in such a way as to be consistent with this spacial separation between the bulk of the mass in the clusters and the intergalactic gas [10], further indicating the existence of particulate dark matter.

In apparent contradiction to this evidence is the Abell 520 merger event [11], in which a large DM density is seen to be spatially separated from the galaxies inside the colliding clusters. Several possible explanations for this behavior are presented

Figure 1.2: Bullet Cluster merger event. Visible image courtesy of [2], X-ray (red) [3], lensing map (blue) [2].

in Ref. [11], including the possibility of collisional dark matter, a concept explored further in Refs. [12, 13]. However, a recent analysis by Clowe et.al. [14] has refuted the earlier claims of a discrepancy between the Abell 520 and Bullet clusters.

Cosmic Microwave Background

The total energy density in the Universe is parametrized by the fraction $\Omega = \rho/\rho_c$, where $\rho_c = 1.06 \times 10^4\,\mathrm{eV\,cm^{-3}}$, and is the energy density required for a flat Universe. The relative contributions to Ω from different sources can be ascertained by a variety of methods, one of which is analysis of the Cosmic Microwave background (CMB). The CMB is the near homogeneous background of photons produced in the early Universe, which last interacted/scattered when the electron proton plasma cooled to the point where neutral hydrogen was able to form. The spectrum of this radiation is very close to that of a black body whose peak temperature has

red-shifted to a current value of 2.726 K. The homogeneity of the matter-radiation distribution was, however, broken by density perturbations left over from cosmic inflation [15–19], planting the seed for the growth of structure. This resulted in the CMB power spectra deviating from a black body; the nature of this deviation provides useful information about the relative contributions from different types of energy density at the time of CMB decoupling. High precision analysis of the CMB power spectra by the WMAP collaboration [20], coupled with analyses of baryonic acoustic oscillations [21], and the Hubble expansion rate [22], have shown the value of Ω_{tot} to be close to unity, and contain the following contributions [23]

$$\begin{aligned} \Omega_\Lambda &= 0.725 \pm 0.016, & \Omega_{DM}h^2 &= 0.1126 \pm 0.0036, \\ \Omega_b h^2 &= 0.0255 \pm 0.00054, & \Omega_r h^2 &\sim 0, \end{aligned} \tag{1.1}$$

where h is the Hubble parameter, defined by $h = H_0/100\,\text{km}^{-2}$ s Mpc.

1.1.2 Structure Formation in the Universe

The energy density of radiation scales like a^{-4}, while that of matter scales as a^{-3}, where a is the scale factor which quantifies the expansion of the Universe, satisfying the the condition

$$\frac{\dot{a}}{a} = H, \tag{1.2}$$

where H is the Hubble expansion rate. Consequently, at some point in the evolution of the Universe, the energy density of matter overtook that of radiation. At this point gravitational interactions between dark matter particles became important, and structure began to form.

At this epoch the Universe was homogeneous and isotropic, with the exception of small density perturbations left over from cosmic inflation [15–19]. The gravitational interaction between dark matter particles caused the growth of these

density perturbations, eventually evolving into the large scale filamentary structure we observe today. The growth of structure was highly sensitive to whether or not the dark matter was relativistic at the beginning of structure formation.

Large scale N-body simulations of gravitationally interacting systems [24–31], indicate that scenarios in which dark matter was relativistic at the time of structure formation lead to 'top down' structure formation, with large pancake like structures forming first, then fragmenting into smaller galactic scale structures at later times. This paradigm, known as 'Hot Dark Matter' is currently excluded, as its prediction of the timescale of formation of small scale structure is in conflict with observations of high redshift galaxies [32]. Thermal relics with eV scale masses are examples of hot candidates, implying that SM neutrinos are excluded as DM candidates.

The best agreement between simulation and observation of large scale structure is found if dark matter was non-relativistic at the time of structure formation, in a scenario broadly referred to as 'Cold Dark Matter' (CDM). In CDM models structure formed hierarchically, with galactic and sub-galactic scale structures forming first, later merging to form clusters and eventually super-clusters of galaxies. This, coupled with the standard cosmological paradigm of a dark energy dominated Universe, is collectively referred to as the ΛCDM model. A popular example of CDM is a thermal relic with a GeV scale mass.

1.1.3 Galactic Halo Profiles

The density profiles of galaxies can be inferred by the rotation curves of the stars bound within. N-body simulations in the ΛCDM model, like those discussed briefly in Section 1.1.2, make predictions of these profiles which are in good agreement with observation. Fits to these simulations can in general be parametrized by the

Profile	α	β	γ	r_s(kpc)
Isothermal	2	2	0	5
Kravtsov	2	3	0.4	10
NFW	1	3	1	20
Moore	1.5	3	1.5	28

Table 1.1: Density Profile Parameters for the Milky Way.

following relation

$$\rho(r) = \frac{\rho_0}{(r/r_s)^\gamma [1 + (r/r_s)^\alpha]^{(\beta-\gamma)/\alpha}}, \tag{1.3}$$

in which (α, β, γ) are dimensionless parameters, and r_s is the scale radius, or the radius at which the density transitions between two different power laws. The parameter ρ_0 is a normalizing energy density which, for the Milky Way, is fixed such that at the radius of the solar circle ($R_{sc} = 8.5$ kpc) the density is $\rho(R_{sc}) = 0.3$ GeV cm^{-3}. Various groups have performed simulations of galactic structure formation, the consequent fits being the Isothermal [25, 26], Kravtsov [27], Navarro Frenk and White (NFW) [28], and Moore [29] profiles, which are displayed in Table 1.1.

An alternative to the parametrization in Eq. 1.3 is the Einasto profile [30, 31], given by

$$\rho(r) = \rho_0 \exp\left[\frac{-2}{\alpha}\left(\left(\frac{r}{r_s}\right)^\alpha - 1\right)\right], \tag{1.4}$$

in which $\alpha = 0.17$ and $r_s \simeq 20$ kpc. The corresponding theoretical predictions of the Milky Way density profile can be seen in Fig. 1.3. Clearly all are in relatively good agreement for radii outside the scale radius, diverging from one another towards the Galactic center. The cuspy nature of some of these profiles at small radii is in conflict with the observation of near constant core density in low surface

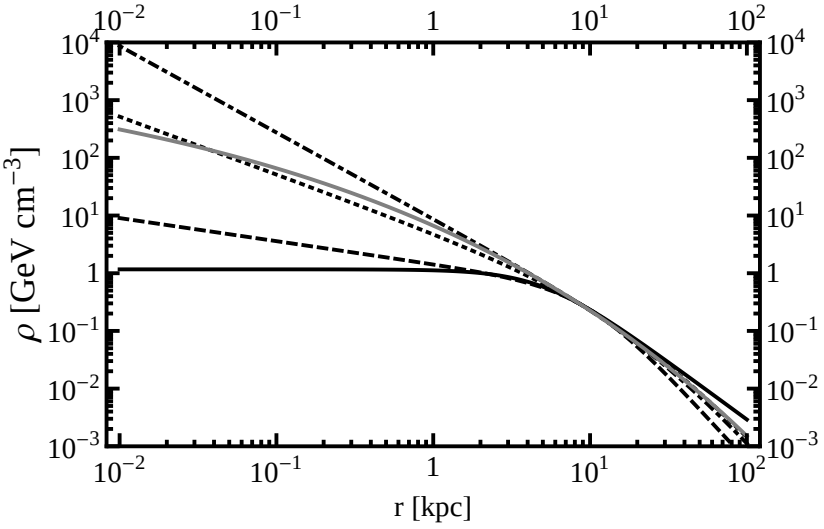

Figure 1.3: Density Profiles for Milky Way for Isothermal (solid-black), Kravitsov (dashed), NFW (dotted), Moore (dot-dashed) and Einasto (solid-gray) profiles.

brightness galaxies [33]. This suggests a potential issue with the standard ΛCDM scenario, and the doubtful reliability of its predictions of dark matter densities inside r_s of the Galactic center. This over-prediction of central density is relevant to our work on decaying dark matter, and will be discussed further in Section 2.1.1.

1.2 Interacting Dark Matter

Up to this point in the discussion, we have assumed dark matter only interacts gravitationally, as motivated by the observation that it is nearly collision-less. There may however be weak DM-DM or DM-visible interactions, which can take on a variety of forms, and whose presence are yet to be detected. DM-visible interactions are well motivated in that they provide a mechanism for producing the correct DM relic abundance. The observed density of $\Omega_{DM}h^2 \simeq 0.11$ is a natural consequence of models in which DM annihilates into Standard Model particles with a weak-scale

cross section, and has a mass in the GeV-TeV range. Dark matter particles exhibiting weak-scale interactions are known as Weakly Interacting Massive Particles (WIMPs) [34–39]. Importantly, WIMPS with GeV-TeV scale masses are consistent with ΛCDM

Though dark matter is required to be stable or meta stable on timescales less than the age of the Universe, there is the possibility it can decay at late times, either invisibly or via processes such as $\chi \to SM$ or $\chi \to \chi' + SM$. Decays into SM particles could result in detectable astrophysical fluxes, the non-observation of which allow us to constrain the DM lifetime. We discuss such constraints in Section 1.2.2.

There are three possible mechanisms aside from decay, through which a WIMP-like dark matter particle χ can interact with SM fields: annihilation ($\chi\chi \to SM$), scattering ($\chi + SM \to \chi + SM$), and production ($SM \to \chi\chi$). In many models these processes all result from the same fundamental couplings and are therefore related, with constraints on one being translatable to constraints on the others. All three of these processes potentially allow the the detection of DM in the laboratory, with their non-observation leading to constraint on dark matter models. Annihilation allows for an indirect observation of dark matter through its annihilation products, and is the focus of Section 1.2.1. Scattering processes allow for the direct detection of nuclear recoil events and are the focus of Section 1.2.3. Production provides the potential to create and observe dark matter in colliders and is the focus of Section 1.2.4.

1.2.1 Indirect Detection

Astrophysical observations are an important tool in the quest to understand dark matter. Not only are they important in uncovering the distribution of dark mat-

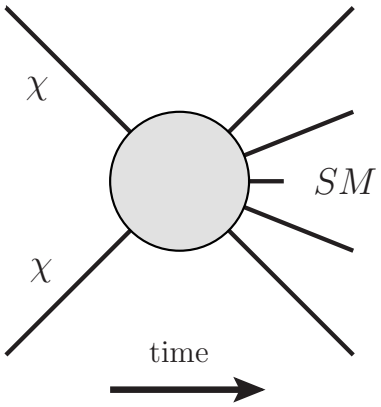

Figure 1.4: Generic dark matter annihilation.

ter on large scales, but can be used to probe potential interactions between dark matter and SM states. Specifically, looking for the products of dark matter annihilation in astrophysical fluxes allows one to place limits on the strength of DM-SM interactions.

Annihilation

Dark matter annihilations proceed via the diagram in Fig. 1.4, in which the composition of the final states and the nature of the annihilation vertex, depend specifically on the dark matter model under consideration.

The products of dark matter annihilation need to be distinguished from the myriad of astrophysical backgrounds, coming from either the Galactic center or the diffuse background away from the Galactic plane. This should appear as either a feature in observed particle spectra, or more modestly, an excess above expected background events. For example, should a particular model allow for the process $\chi\chi \rightarrow \gamma\gamma$, this should appear as a mono-energetic line in the photon spectrum. The observation of a line-like feature is often referred to as 'smoking gun' evidence for dark matter, as such a feature does not easily arise from purely astrophysical sources. The non-observation of such features in astrophysical backgrounds places

constraints on WIMP models.

In particular, the expected flux of visible particles from decays in the Milky Way can be calculated for a given model and compared with observation. The flux is calculated for the line of sight, and averaged over solid angle $\Delta\Omega = 2\pi(1-\cos\psi)$, where ψ is the angle from the galactic center. The differential flux of SM decay products averaged over solid angle $\Delta\Omega$, is given by the following relation

$$\frac{d\Phi_{\Delta\Omega}(\psi)}{dE_{SM}} = \frac{1}{4\pi}\mathcal{P}(E_{SM}, m_\chi)\mathcal{J}_{\Delta\Omega}(\psi), \tag{1.5}$$

in which all specific dependence on the particle physics model is contained in $\mathcal{P}(E_{SM}, m_\chi)$, while all dependence on choice of dark matter halo profile is contained in $\mathcal{J}_{\Delta\Omega}(\psi)$.

Assuming equal amounts of dark matter and dark antimatter, the first term in Eq. 1.5 is given by [25]

$$\mathcal{P}(E_{SM}, m_\chi) = \frac{\langle\sigma v\rangle}{m_\chi^2}\frac{dN_{SM}}{dE_{SM}}, \tag{1.6}$$

in which $\langle\sigma v\rangle$ is the velocity averaged cross section for the DM annihilation process, and dN_{SM}/dE_{SM} is energy spectrum per decay of the final state. If the dark matter is Majorana (self conjugate) in nature, an additional factor of $1/2$ is introduced into the right hand side of Eq. 1.6.

The second term in Eq. 1.5 is given by [25]

$$\mathcal{J}_{\Delta\Omega}(\psi) = \frac{2\pi}{\Delta\Omega}\int_{\cos\psi}^{1}\int_{0}^{l_{max}} \rho\left(\sqrt{R_{sc}^2 - 2lR_{sc}\cos\psi' + l^2}\right)^2 dl d(\cos\psi'), \tag{1.7}$$

in which l is the magnitude of the line of sight vector at angle ψ from the galactic center, with $l_{max} = \sqrt{R_{MW}^2 - \sin^2\psi' R_{sc}^2} + R_{sc}\cos\psi'$ (R_{MW} is the radius of the Milky Way, and R_{sc} is the solar radius). The DM density ρ is determined by the halo density profile, the choices for which were discussed in Section 1.1.3. Given the quadratic dependence on the density, the theoretical uncertainty on the halo profile has a significant effect on the expected flux for small ψ.

The flux in Eq. 1.5 can be compared with the observed flux, and in assuming that the entire observed signal comes from dark matter annihilation, a conservative upper-bound can be placed on $d\Phi_{\Delta\Omega}/dE_{SM}$, and therefore on $\langle\sigma v\rangle$. Less conservative work attempts to estimate the astrophysical backgrounds. This methodology has been used to constrain many models through a variety of annihilation channels, some examples of which can be found in Refs. [4, 40–56].

1.2.2 Decay

It is possible that dark matter χ is unstable or meta-stable. In some models the final state may contain only SM fields ($\chi \to SM$), while in others, it may contain one or several stable WIMPs χ' ($\chi \to \chi' + SM$), for which $m'_\chi < m_\chi$.

The expected flux from decays in the Galactic center are given by an analogue of Eq. 1.5, though the forms of the functions $\mathcal{P}$ and $\mathcal{J}_{\Delta\Omega}$ differ with respect to the annihilation case. The particle physics dependent piece is now given by [57]

$$\mathcal{P}(E_f, m_\chi) = \frac{1}{m_\chi \tau_\chi e^{\tau_0/\tau_\chi}} \frac{dN_{SM}}{dE_{SM}}, \tag{1.8}$$

in which τ_χ is the lifetime of χ, and τ_0 is the current age of the Universe. The factor e^{τ_0/τ_χ} appears in models for meta-stable dark matter, and accounts for the fact that the number of unstable DM particles χ' may have decreased significantly due to decays.

Given that the initial state only has a single dark matter particle, the flux depends on only a single power of the energy density, thus the halo dependent piece of Eq. 1.5 becomes [57]

$$\mathcal{J}_{\Delta\Omega}(\psi) = \frac{2\pi}{\Delta\Omega} \int_{\cos\psi}^{1} \int_{0}^{l_{max}} \rho\left(\sqrt{R_{sc}^2 - 2lR_{sc}\cos\psi' + l^2}\right) dl d(\cos\psi'). \tag{1.9}$$

A consequence of this is that while the theoretical uncertainty in the halo profile is still significant, it has less of an effect on the expected flux from decays than it has on annihilations.

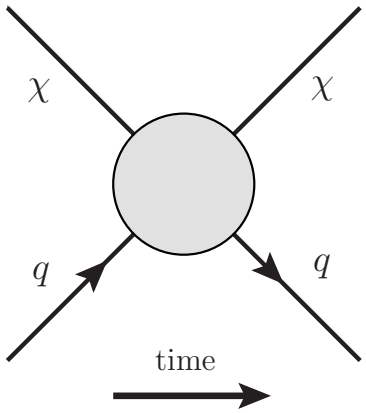

Figure 1.5: Generic dark matter-quark scattering.

As with annihilation, the observed flux of visible states can be used as an upper bound on the flux from dark matter decays, and used to put a lower bound on the dark matter lifetime. Examples of constraints on decays can be found in [4, 45, 48, 49, 57–59]. Investigating constraints on decays of meta-stable WIMPs is the topic of Section 2.2 of this thesis.

1.2.3 Direct Detection

The same coupling responsible for annihilation of dark matter into fermions can, in many models, cause scattering processes. Of particular interest are scattering processes like that pictured in Fig 1.5, in which a dark matter particle scatters off a quark. This allows for DM-nucleon (n) and, by extension, DM-nuclear (N) scattering. These processes can be probed by looking for recoil events in ultra-cold atomic systems. The non-observation of nuclear recoils allows constraints to be placed on the DM-nucleon cross section. The expected differential scattering rate between DM and nuclei (on earth) is given by the following relation [60]

$$\frac{dR}{dE_R} = N_T \frac{2\rho_0}{m_\chi} \int_{v_{min}}^{v_{max}} \frac{d\sigma}{d|\vec{q}|^2}(E_R + m_N) v f(\vec{v}) d\vec{v}, \tag{1.10}$$

in which N_T is the number of target nuclei, E_R is the nuclear recoil energy, and $|\vec{q}|$ is the momentum transfered to the nucleus. The quantities ρ_0 and $f(\vec{v})$ are the local dark matter density and velocity distribution function respectively, and are subject to theoretical uncertainties related to those outlined in Section 1.1.3.

The form of $d\sigma/d|\vec{q}|^2$ contains all particle physics information, and depends strongly on the type of scattering that takes place. There are two distinct ways in which χ can interact with the nucleus, spin-dependently (SD) or spin-independently (SI). The process in Fig. 1.5 can be expressed in terms of an effective 4-Fermi operator; the form of this operator determines the nature of the interaction.

For SD interactions, dark matter couples to the nucleon spin, thus only the unpaired or valence nucleons in the nucleus will contribute to DM-nuclear scattering. SD interactions arise from axial-vector ($\gamma_5\gamma_\mu$) operators, for example

$$\mathcal{L}_{\text{int}} = \frac{1}{\Lambda}\overline{\chi}\gamma_5\gamma_\mu\chi\overline{q}\gamma_5\gamma^\mu q, \tag{1.11}$$

where Λ is the energy scale at which the effective theory breaks down. This can be scaled to an effective DM-n operator using the following identity [34, 61–64]

$$\langle \mathsf{n}|\overline{q}\gamma_5\gamma_\mu q|\mathsf{n}\rangle \equiv 2s_\mu^{(\mathsf{n})}\Delta q^{(\mathsf{n})}, \tag{1.12}$$

in which $s_\mu^{(\mathsf{n})}$ is the nucleon spin 4-vecor, and $\Delta q^{(\mathsf{n})}$ is a constant to be determined experimentally. It can be shown that the differential DM-N cross section in the SD case is given by [61–63]

$$\frac{d\sigma}{d|\vec{q}|^2} = \frac{8G_F^2}{(2J+1)v^2}S(|\vec{q}|, \Delta q^{(p)}, \Delta q^{(n)}), \tag{1.13}$$

in which J is the nuclear spin, and v the dark matter velocity. The nuclear dependent form factor $S(|\vec{q}|, \Delta q^{(p)}, \Delta q^{(n)})$ contains all Λ dependence. Some examples of form factors are given in Refs. [34, 61–63]. The convention in the direct detection literature is to normalize the nuclear form factors appropriately so that the cross section contains explicit G_F dependence.

SI interactions arise from scalar, vector (γ^μ) and tensor ($T^{\mu\nu}$) operators. SI DM-quark operators can be scaled to DM-n operators in a similar fashion to SD operators. As an example consider the scalar interaction

$$\mathcal{L}_{\text{int}} = \frac{1}{\Lambda}\overline{\chi}\chi\overline{q}q. \tag{1.14}$$

This can be scaled similarly to Eq. 1.12 [34, 61, 64]

$$\langle \mathsf{n}|\overline{q}q|\mathsf{n}\rangle \equiv \frac{m_{\mathsf{n}}}{m_q} f_{Tq}^{(\mathsf{n})}, \tag{1.15}$$

in which $f_{Tq}^{(\mathsf{n})}$ is a constant determined by experiment. For the SI scalar case, the differential cross section is given by [34, 61, 62, 64]

$$\frac{d\sigma}{d|\vec{q}|^2} = \frac{G_F^2}{v^2} C_{scal} F(E_R)^2, \tag{1.16}$$

in which $F(E_r)$ is a nuclear form factor, some examples of which are given in Refs. [34, 61, 62]. The constant C_{scal} is defined to be [34, 64]

$$C_{scal} = \frac{1}{\pi G_F^2}[Z f_p + (A - Z) f_n]^2, \tag{1.17}$$

where Z is nuclear charge, and A atomic number. The parameters f_{n} are the effective couplings to the nucleons, which depend on $f_{Tq}^{(\mathsf{n})}$ and the cutoff scale Λ. Depending on the choice of model, the scalar coupling may contain contributions from various sources, including coupling to gluons, Higgs exchange, and one-loop processes [34, 61]. As is clear from Eq. 1.17, in contrast to SD scattering, there are coherent contributions from interactions with all nucleons in the nucleus. Thus, spin-independent interactions usually dominate over the spin-dependent scattering, particularly for the heavy elements used in direct detection experiments. Note that this description of the cross section, in particular coherent scattering, breaks down for momentum transfers lower than the energy scale defined by the nuclear diameter, implying a limit to the usefulness of increasing nuclear size.

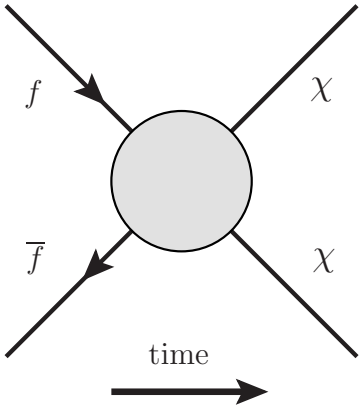

Figure 1.6: Generic dark matter production process.

There are various direct detection experiments in operation, using heavy elements such as Xenon [60, 65, 66], Silicon and Germanium [67–69] and various other materials [70, 71], and the DM-nucleon cross section is constrained considerably by observation.

1.2.4 Production

Last in our exploration of DM-SM interactions are processes like that pictured in Fig. 1.6, in which a pair of SM particles (in this case fermions) annihilate into a pair of DM particles. These processes are relevant for collider experiments, allowing for the possibility of direct dark matter production. Of particular interest are processes in which the initial state fermions are quarks, as this allows for production of dark matter at the LHC.

Given the WIMP-like nature of χ, we would expect the dark matter produced in Fig. 1.6 to escape the LHC's detectors completely undetected, making this process on its own unobservable. As with neutrinos, the presence of the invisible dark matter particles is only indicated by an apparent violation of conservation of energy-momentum in the detector system. Thus at least one visible particle is required

in the final state, against whose momentum some amount of missing momentum can be reconstructed. In the language of collider physics, the magnitude of this momentum is referred to as the missing energy.

The quarks responsible for the DM production in Fig. 1.6 carry some fraction x of the colliding proton's momentum. This fraction is probabilistic, being determined by Parton Distribution Functions (PDF), and is therefore not predictable on an event by event basis. This indeterminacy of the initial state momentum makes accurate reconstruction of missing energy in the longitudinal direction (i.e, beamline direction) impossible. Thus, the useful variable in dark matter searches is the missing energy in the transverse plane ($\not{E}_T$).

The possibilities for the visible final state from which the $\not{E}_T$ is reconstructed are highly model dependent, and indeed in any given model there may be several search channels for dark matter. The prime example of this is Supersymmetry (SUSY). There is significant model variation in SUSY, with different SUSY models providing different DM candidates [72]. The dominant search channel depends on the SUSY model and parameters chosen [73]. For example, for neutralino dark matter, in the region of parameter space in which the gluino is kinematically accessible, DM may be detectable through a number of final states, including multiple jets and/or multiple leptons [74–77]. Conservation of R-parity implies that any SUSY decay chain will end in the lightest stable supersymmetric particle for a given model, and will therefore have some missing energy signal.

Regardless of the choice of dark matter model, there will always be the possibility that a gauge boson will be radiated from one of the initial state quarks. For this reason, searches for a single gauge boson plus $\not{E}_T$ are the most general search strategies for DM at the LHC. A consequence of the largeness of α_s is that gluon radiation (resulting in a mono-jet plus $\not{E}_T$ signal) has the largest cross section at the LHC. This process has been considered by several authors [78–87], with

LHC data used to constrain the possible 4-Fermi effective operators responsible for the process pictured in Fig. 1.6. As in Ref. [88], mono-jets can also be used to probe non-standard neutrino interactions. Mono-photons have been considered in Refs. [83, 89, 90], and while not as constraining as mono-jet searches [79, 91], are nonetheless an important search channel for dark matter. Recently, electroweak bremsstrahlung has been considered, and the potential signatures of mono-W [92] and mono-Z [93] emission explored. The focus of Chapter 4 of this thesis is the expected signatures of WIMP dark matter in the mono-Z search channel.

1.3 Relic Abundance

Of fundamental importance in the quest to understand the nature of dark matter is the mechanism through which it was created in the early Universe. Though little is known for certain about the production mechanism for dark matter, the non-gravitational interactions discussed in Section 1.2 provide a useful avenue for exploration. Processes like those in Figs. 1.4-1.6 have potentially caused the visible and dark sectors to be in thermal equilibrium in the early Universe, allowing dark matter and the Standard Model to share a common production mechanism. The basic principals behind thermal production are highlighted in Section 1.3.1. In Section 1.3.2 we discuss the phenomenon known as coannihilation, in which there were contributions to the DM relic density from several states with near degenerate mass.

1.3.1 Thermal Relic Dark Matter

At times much less than a second when the number density was high, interactions acted to keep all SM fields in thermal equilibrium with each other. The system was well approximated by a Maxwell-Boltzmann fluid at temperature T, whose species

obeyed the distribution function $f(E) \sim \exp[-E/T]$ [32]. If interactions such as those pictured in Figs. 1.4-1.6 were present, a similar equilibrium would have existed between DM and the SM, ensuring that dark matter maintain a Maxwell-Boltzmann distribution, and a common temperature with the SM. The dark matter number density in this scenario was determined by the Boltzmann equation

$$\frac{dn_\chi}{dt} + 3Hn_\chi = -\langle\sigma v_{rel}\rangle \left(n_\chi^2 - (n_\chi^{eq})^2\right), \tag{1.18}$$

in which H is the Hubble expansion rate, and n_χ the DM number density. The equilibrium number density n_χ^{eq}, was given by

$$n_\chi^{eq} = g_\chi \int \frac{d^3\vec{p}}{(2\pi)^3} e^{-E/T} = \frac{2g_\chi}{(2\pi)^2} m_\chi^2 T K_2\left(\frac{m_\chi}{T}\right), \tag{1.19}$$

where g_χ is the number of degrees of freedom that the dark matter possessed. The velocity averaged annihilation cross section $\langle\sigma v_{rel}\rangle$, is given by [94]

$$\langle\sigma v_{rel}\rangle = \frac{T\, g_\chi^2}{32\pi^4 (n_\chi^{eq})^2} \int_{4m_\chi^2}^{\infty} \sigma(s)\, \left[s - 4m_\chi^2\right] \sqrt{s}\, K_1\left(\frac{\sqrt{s}}{T}\right) ds, \tag{1.20}$$

in which $K_1(x)$ and $K_2(x)$ are modified Bessel functions of the first and second kind respectively, and $\sigma(s)$ is the cross section for the process $\chi\chi \to SM$, which depends greatly on the choice of DM model.

The Hubble expansion rate was given by

$$H \equiv \frac{\dot{a}}{a} = \frac{1}{2t} = \frac{1.66\sqrt{g_*}T^2}{m_{Pl}}, \tag{1.21}$$

where

$$g_*(T) \equiv \sum_{i=\text{bos}} g_i \left(\frac{T_i}{T}\right)^4 + \frac{7}{8} \sum_{i=\text{ferm}} g_i \left(\frac{T_i}{T}\right)^4. \tag{1.22}$$

Thus, as the Universe expanded the temperature decreased. At some time the temperature T dropped below m_χ, and the number density in Eq. 1.19 became exponentially suppressed. This caused the annihilation rate, given by $\Gamma = n_\chi \langle\sigma v_{rel}\rangle$,

to die off exponentially with temperature. At some critical temperature $\Gamma \simeq H$, the annihilation rate dropped below the Universal expansion rate. At this point annihilation ceased, and the co-moving number density of the DM became fixed.

To express this more explicitly, we need to find solutions to the Boltzmann equation in Eq. 1.18. Specifically, we need to determine the temperature at which n_χ departed from n_χ^{eq}, which indicates Γ approaching H. It is convenient to express Eq. 1.18 in terms of the number density per unit entropy $Y = n_\chi/s$.

From Eq. 1.18 and the definition of entropy, it can be easily shown that

$$\frac{dY}{dt} = -s\langle\sigma v_{rel}\rangle(Y^2 - Y_{eq}^2), \tag{1.23}$$

and hence

$$\frac{dY}{dT} = \sqrt{\frac{\pi}{45}} g_*^{1/2} m_{Pl}\langle\sigma v_{rel}\rangle(Y^2 - Y_{eq}^2). \tag{1.24}$$

The variable $g_*^{1/2}$ is a measure of the total number of degrees of freedom in equilibrium given by

$$g_*^{1/2} \equiv \frac{g_{*s}}{\sqrt{g_*}}\left(1 + \frac{T}{3g_{*s}}\frac{dg_{*s}}{dT}\right), \tag{1.25}$$

in which

$$g_{*s}(T) \equiv \sum_{i=\text{bos}} g_i\left(\frac{T_i}{T}\right)^3 + \frac{7}{8}\sum_{i=\text{ferm}} g_i\left(\frac{T_i}{T}\right)^3, \tag{1.26}$$

as defined in Refs. [94, 95]. Following the methodology of Refs.[32, 94, 95], it is straight forward to solve Eq. 1.24 at the departure of Y from its equilibrium value. This leads to the following criteria for thermal production of DM

$$\Omega_\chi h^2 = 2.818 \times 10^8 \frac{m_\chi}{\text{GeV}}\left[\frac{1}{Y_f} + \sqrt{\frac{\pi}{45}} m_{Pl}\int_{T_0}^{T_f} g_*^{1/2}\langle\sigma v_{rel}\rangle dT\right]^{-1}, \tag{1.27}$$

where T_f is the temperature at the time of departure, $Y_f = Y_{eq}(T_f)$, and $\Omega_\chi h^2 \simeq 0.11$ as outlined in Section 1.1.1. The relic abundance, determined by Eq. 1.27,

turns out to be relatively insensitive to the DM mass, roughly leading to the constraint $\langle \sigma v_{rel} \rangle \sim 10^{-26}\text{cm}^3/\text{s}$. This, as it happens, is a natural cross section for annihilation of a WIMP in the GeV mass range. This coincidence is generally referred to as the 'WIMP miracle', and is one of the great motivations for interacting dark matter.

1.3.2 Coannihilation

Let us consider N species X_i which were near degenerate in mass. As each unstable species dropped out of equilibrium, it decayed, eventually reaching a stable state, that is, dark matter. Assuming the decay rate of the heavier species into dark matter occurred on much shorter timescales than Universal expansion, all species X_i contributed to the relic abundance, and the total number density $n = \sum_i^N n_i$ can be equated to the DM number density n_χ.

The Boltzmann equation describing the total abundance is given by [96]

$$\frac{dn}{dt} + 3Hn = -\sum_{i,j}^{N} \langle \sigma_{ij} v_{ij} \rangle \left(n_i n_j - n_i^{eq} n_j^{eq} \right). \tag{1.28}$$

Similarly to Eq. 1.20, the thermally averaged annihilation cross section $\langle \sigma_{ij} v_{ij} \rangle$ is given by [94]

$$\langle \sigma_{ij} v_{ij} \rangle = \frac{T\, g_i g_j}{32\pi^4 n_i^{eq} n_j^{eq}} \int_{(m_i+m_j)^2}^{\infty} \sigma(s)_{ij} \frac{\left[s-(m_i+m_j)^2\right]\left[s-(m_i-m_j)^2\right]}{\sqrt{s}} K_1\left(\frac{\sqrt{s}}{T}\right) ds, \tag{1.29}$$

in which $\sigma(s)_{ij}$ is the cross section for process $X_i X_j \to SM$.

The presence of the coannihilation processes, $X_i X_j \to SM$, imply the existence of the mixing processes $X_i + SM \to X_j + SM$. When the species X_i were non-relativistic, their equilibrium number densities dropped exponentially, becoming far lower in abundance than the still relativistic SM degrees of freedom. We therefore

expect the rates for the annihilation processes $X_i X_j \to SM$ to have been greatly suppressed relative to mixing processes $X_i + SM \to X_j + SM$. This ensured the relative number densities of species X_i maintained their equilibrium values, despite annihilations removing those species from the bath at different rates, i.e., [96]

$$\frac{n_i}{n} \simeq \frac{n_i^{eq}}{n^{eq}}. \tag{1.30}$$

The Boltzmann equation therefore becomes

$$\frac{dn}{dt} + 3Hn = -\langle \sigma v \rangle_{eff} \left(n^2 - (n^{eq})^2 \right), \tag{1.31}$$

where

$$\langle \sigma v \rangle_{eff} = \sum_{i,j}^{N} \langle \sigma_{ij} v_{ij} \rangle \frac{n_i^{eq} n_j^{eq}}{n^{eq} n^{eq}}. \tag{1.32}$$

Given the prompt decay of unstable contributions to n, the total number density is equal to the DM density n_χ, and Eq. 1.31 can be used to determine the relic abundance in a similar fashion to Eq. 1.18 in Section 1.3.1. The distinction from the standard case is that $\langle \sigma v \rangle_{eff}$, as opposed to $\langle \sigma v_{rel} \rangle$, contains contributions from annihilation processes involving all species X_i, not just the DM χ.

2

Models for Dark Matter Decay

Given its accurate replication of large scale structure, the ΛCDM model has become the most popular framework for dark matter. It does, however, suffer from inaccuracies in its prediction of small scale structure. In this chapter we discuss one possible solution to this problem. We consider models in which dark matter is only meta-stable. In this work we seek to explore constraints on this class of model, and present a specific particle physics model to realize this scenario.

In Section 2.1 we present the problems with ΛCDM in more detail, along with a possible solution. In Section 2.2 we explore the observational constraints on this class of model, deriving constraints on decays into neutrinos. The focus of Sections 2.3 and 2.4 will be the construction of an explicit particle physics model for decaying dark matter. We conclude in Section 2.5.

2.1 The Small Scale Structure Problem and Decaying Dark Matter

2.1.1 The Small Scale Structure Problem

Many body gravitational simulations of ΛCDM paradigm are, as discussed in Section 1.1.2, in very good agreement with observed large scale structure. This success stems from 'bottom up' structure formation, in which galactic scale structures form early. ΛCDM is not problem free however, as it tends to over-predict small scale power [29, 97–110].

The issue of small scale power was highlighted in Section 1.1.3, which contained a discussion of galactic halo profiles. As discussed in that section, there is a large amount of theoretical uncertainty as to the abundance of DM near the Galactic Center. Indeed, all predictions from numerical simulations involving CDM are in contrast with observation of near constant core density in low surface brightness galaxies [33]. Such simulations are also erroneous in their prediction of the number of satellite galaxies orbiting Milky Way sized objects, over predicting their multiplicity by a factor of around 10 [8, 29, 97, 106, 111, 112]. Although these simulations do not include visible matter, the gravitational potential wells they predict would promote a level of star formation not observed. Though these issues may be partially alleviated by tidal disruption and other effects, the small scale power problems of ΛCDM are still poorly understood (see e.g. [113, 114] for recent work).

These discrepancies have led many to consider a dark matter candidate somewhere between the 'Hot' and 'Cold' regimes. Models for 'Warm' dark matter, often involving keV mass particles, soften the small scale power problem, while maintain-

ing the 'bottom up' structure formation that made ΛCDM appealing. While warm dark matter is appealing from an astrophysical standpoint, obtaining the correct relic abundance in a natural way can be difficult in these models. In this work, as in [115–123], we will consider an alternative hypothesis in which DM does not consist of a single stable species.

2.1.2 A possible Solution: Decaying Dark Matter

We consider a scenario with two WIMP candidates, in which one species is unstable, decaying into the other. If the mass splitting between the two WIMPS is sufficiently small, the decay process will leave the overall halo mass unaffected, while giving the daughter DM particles a small velocity kick. Such velocity kicks heat the dark matter halos and cause them to expand, softening the central cusps and disrupting small halos [7, 8, 124–126]. Such models are appealing, as they can alleviate the small scale structure problems, while retaining the attractive features of cold dark matter.

We shall assume the DM decays predominantly via the channel

$$\chi^* \to \chi + l\,, \tag{2.1}$$

where χ^* and χ denote the heavier and lighter candidate, respectively, and l is some relativistic final state. The mass splitting between χ^* and χ is given by

$$\Delta m = m_{\chi^*}\epsilon\,, \tag{2.2}$$

where $\epsilon \ll 1$. Abdelqader and Melia [8] have shown the dwarf halo problem can be solved for $\epsilon \simeq (5-7)\times 10^{-5}$ and a decay lifetime of $(1-30)$ Gyr. The work of Peter, Moody, and Kamionkowski [7] has demonstrated that galaxy cusps can be alleviated for a wider range of ϵ and τ_{χ^*}, with the most favored lifetimes in the range $(0.1-100)$ Gyr. Subsequent work by Peter and Benson [127] has

used properties of galactic subhalos to further constrain the allowed values of ϵ, preferring lower values to those favored in [8]. Dark matter decays may be further constrained from analysis of their effect on weak lensing of distant galaxies as in [128]. However, at present, such analyses have only placed limits on models with much larger values of ϵ than those considered in this work.

An interesting possibility, from an observational standpoint, is a decay mode in which the relativistic final state, l, consists of SM particles. This allows the possibility of verifying the model, via the detection of particles produced by decay in our own Galaxy, or of a diffuse flux from decays in halos throughout the Universe. Current astrophysical observations place constraints on the allowed parameters, via comparison of the expected fluxes from decay with relevant astrophysical backgrounds. This will be discussed more detail in Section 2.2.

2.2 Constraints on Meta-stable Dark Matter

Let us consider the process $\chi^* \rightarrow \chi + l$ discussed in the previous section. If l is a visible state, its non-observation above backgrounds should yield a constraint on the lifetime of χ^*. For $\epsilon \sim 10^{-5}$ and $m_\chi \sim$ GeV-TeV, the Δm values of interest are of order 10 keV-10 MeV. Therefore, the possible SM final states are $l = \gamma, e^+e^-, \nu\overline{\nu}$. The least detectable SM particles are neutrinos. Consequently the constraints on DM decay into neutrinos are the weakest but most robust. In Section 2.2.1 we place constraints on the process $\chi^* \rightarrow \chi + \nu + \overline{\nu}$ based on atmospheric neutrino data. Due to the high detectability of γ ray photons, constraints on the lifetime of χ^* from the process $\chi^* \rightarrow \chi + \gamma$ are in general the most stringent. The branching ratio for direct photon production may, however, be tiny in many models, making it important to consider other possible decay products. Photon and positron producing processes are the focus of Section 2.2.2.

2.2.1 Neutrino Constraints

Given that neutrinos are the least detectable stable SM particles, constraints on DM decay (or annihilation) to neutrinos can be used to set conservative but robust lower limits on the DM lifetime (or upper limit on the annihilation cross section) to any SM final state [50]. Palomares-Ruiz [45, 58] obtained limits on the decay channel $\chi \rightarrow \nu + \overline{\nu}$. Here we will adapt the analysis of Refs. [45, 46, 58], to constrain the decay channel $\chi^* \rightarrow \chi + \nu + \overline{\nu}$. This will set the most conservative limit on DM decay modes of the form $\chi^* \rightarrow \chi + l$, where l is any SM final state.

The neutrino flux on Earth from DM decay in the galactic halo is

$$\frac{d\Phi_\nu}{dE_\nu} = \frac{1}{4\pi}\frac{1}{m_\chi \tau e^{\tau_0/\tau}}\mathcal{J}_{\Delta\Omega}\frac{2}{3}\frac{dN}{dE_\nu}. \tag{2.3}$$

The multiplicity of 2 accounts for the sum of ν and $\overline{\nu}$ produced in the decays. As in Refs. [45, 58], we assume equal decay width to all three neutrino flavors, which accounts for the factor of $1/3$ in Eq. 2.3. This is a reasonable approximation, since neutrino flavor oscillations between the production and detection points will considerably weaken any preference toward a particular flavor. For simplicity, and in order to minimize the uncertainty arising from a particular choice of halo profile, we average the expected neutrino signal over the whole sky, $\psi = 180°$. Directional information, whenever available, is in general expected to lead to more stringent limits [45, 51, 58]. There is an inherent model dependence in the energy distribution, dN/dE_ν, for a process with a three body final state. To accommodate this without specializing to a given model, we use the limiting cases, that is, mono-energetic

$$dN/dE = \delta(E - \Delta m/2), \tag{2.4}$$

and flat

$$dN/dE = 1/(\Delta m - 2m_\nu) \simeq 1/\Delta m, \tag{2.5}$$

energy distributions.

For energies $E_\nu \gtrsim 50$ MeV, the neutrino flux on Earth is dominated by atmospheric neutrinos. The atmospheric neutrino flux has been well measured by a number of experiments [129–134], and is in good agreement with theoretical predictions. We utilize the results of the FLUKA [135, 136] calculation of the atmospheric $\nu_\mu + \overline{\nu}_\mu$ background, over the energy range 50 MeV to 10 TeV. We determine a DM decay limit by requiring the expected neutrino signal from DM decay not exceed the atmospheric neutrino flux, integrated over energy bins of width $\Delta \log_{10} E_\nu \sim 0.3$. This choice of bin size is in accordance with that adopted in Refs. [45, 58], and encompasses the experimental resolution of the neutrino detectors. Fig. 2.1 shows limits for both mono-energetic (dashed) and flat (solid) neutrino energy distributions.

At low energies $E_\nu \lesssim 100$ MeV, the relevant data comes from the diffuse supernova neutrino background (DSNB) search performed by the SK experiment [137]. SK searched for positrons produced by incident $\overline{\nu}_e$ on free protons inside the detector, via the inverse β-decay reaction $\overline{\nu}_e + p \to e^+ + n$. Incoming ν_e and $\overline{\nu}_e$ interact also with bound nucleons, producing electrons and positrons. The main sources of background for these observations are atmospheric ν_e and $\overline{\nu}_\epsilon$, and the Michel electrons and positrons from decays of sub-threshold muons. A DSNB signal was not detected. In Refs. [45, 46, 58] a χ^2 analysis of this data was performed, and used to place 90% CL limits on the contribution to the signal from DM annihilation, $\chi\chi \to \nu\overline{\nu}$, or decay, $\chi \to \nu\overline{\nu}$.

We shall employ the DM decay limits of Refs. [45, 58], in order to constrain the lifetime for small Δm, $\Delta m \leq$100 MeV. A simple rescaling suffices to convert these limits into constraints on the decay mode of interest here, $\chi^* \to \chi\nu\overline{\nu}$, under the assumption that $\nu\overline{\nu}$ are emitted mono-energetically. The resulting constraints are shown in Fig. 2.1.

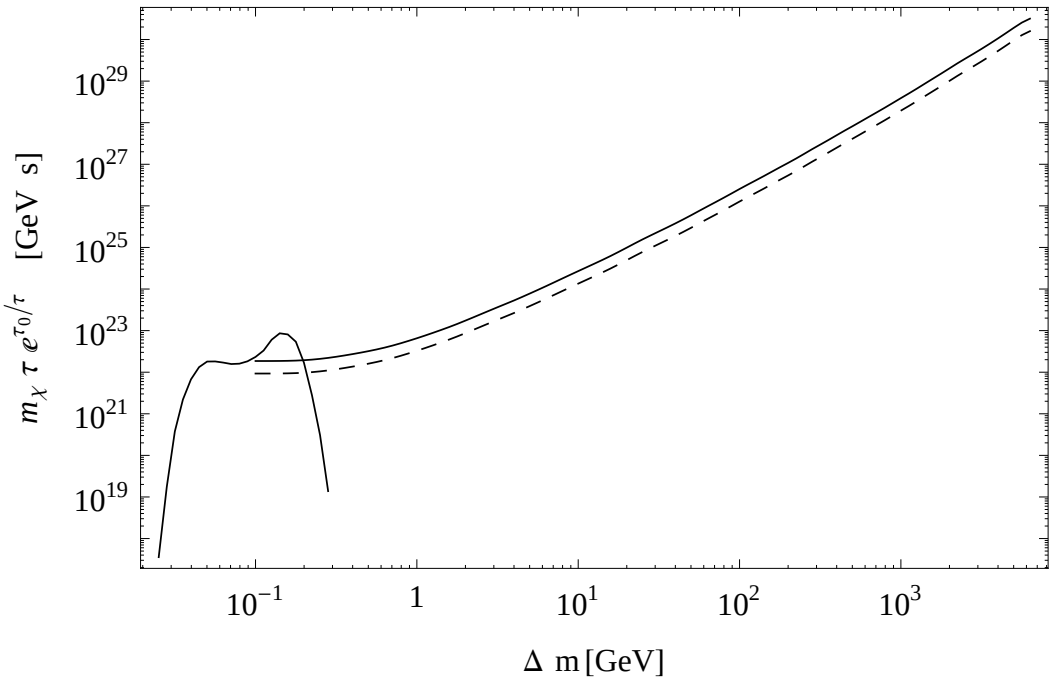

Figure 2.1: Limits on dark-matter decay $\chi^* \to \chi + \nu + \overline{\nu}$. The solid (dashed) lines correspond to mono-energetic (flat) injection distribution of ν, $\overline{\nu}$. The regions below the lines are excluded.

2.2.2 γ-ray and Positron Constraints

The tightest constraints on the DM lifetime come from photon producing processes. In Ref. [4], authors Yüksel and Kistler placed constraints on the lifetime of the decay channel, $\chi^* \to \chi + \gamma$, based on γ-rays from the Galactic Center region, and the isotropic diffuse photon background.

Weaker, but still significant, constraints can be placed on decays into e^+e^- pairs via the process $\chi^* \to \chi + e^+ + e^-$ [5]. These are visible by directly measuring the resulting positrons, or via the subsequent or associated production of photons. The combined limit on e^+e^- decays are displayed in Fig. 2.2 (dashed). Plotted alongside this are the γ constraints from [4] (solid), and the neutrino constraints derived in the previous section (dotted). Results are displayed for a mono-energetic e^+e^- and $\nu\overline{\nu}$ distributions, which turn out to yield the most conservative constraints.

Figs. 2.3-2.5 show the constraints in Fig. 2.2, translated into constraints on τ for varying values of $\epsilon = \Delta m/m_\chi$. For $\tau \ll \tau_0$, all the decays occur very early in the evolution of the Universe, depleting the abundance of χ' and causing the expected flux to die off. For $\tau \gg \tau_0$, decays happen late, implying that though a larger fraction of the dark matter is χ', the decay rate of χ' is lower causing the expected flux to decrease. Between these two extreme limits is a band of excluded lifetimes. Clearly the available parameters have been restricted substantially. Of particular interest is Fig. 2.5, which shows the parameters preferred by Ref. [8] to solve the dwarf halo deficit problem (namely $\epsilon = 5 \times 10^{-5}$ and $1\text{Gyr} < \tau < 30\text{Gyr}$), to be close to ruled out for decays into $e^\pm$ pairs.

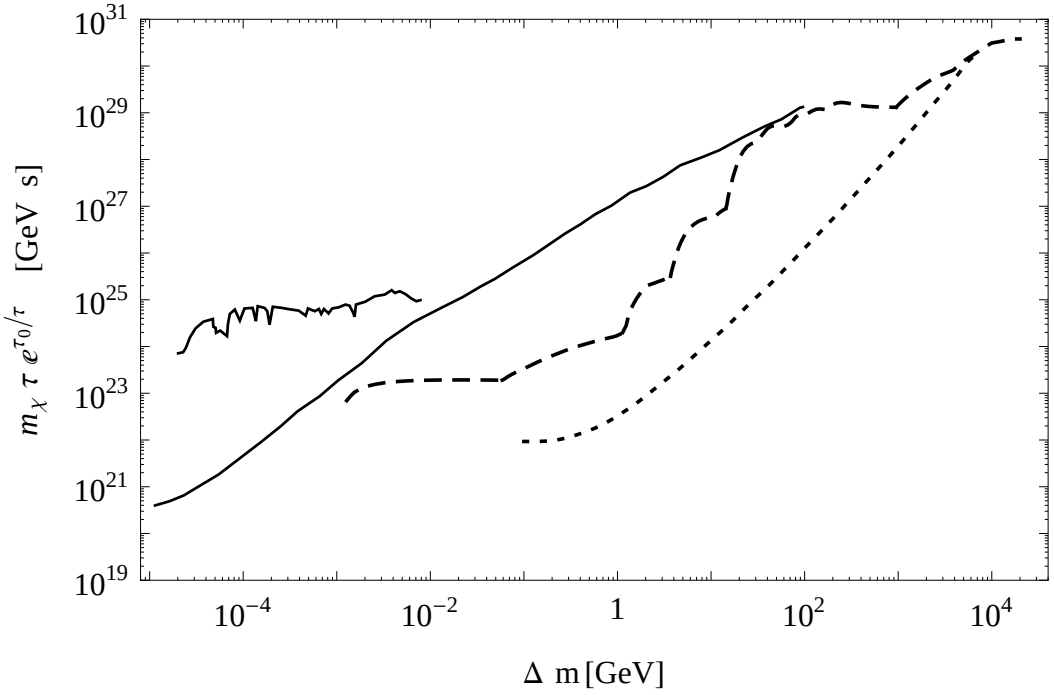

Figure 2.2: Constraints on dark-matter decay channels $\chi \to \chi' + \gamma$ [4] (solid), $\chi \to \chi' + e^- + e^+$ (dashed) and $\chi \to \chi' + \nu + \bar{\nu}$ (dotted). The regions below the lines are excluded.

2.3 A Dark Matter Decay Model

In Section 2.2 we demonstrated the viability (though constricted) of the decaying dark matter scenario from an observational standpoint. The aim of this section is to construct a specific particle physics model which can realize decaying dark matter. We shall use the criterion specified by Abdelqader and Melia [8] [namely, $\epsilon \simeq (5-7) \times 10^{-5}$ and $\tau \sim (1-30)$ Gyr] as a reference point for these models, but given the constraints of Ref. [127], we will choose the more restrictive values of $\epsilon \sim 10^{-5}$ and $\tau \simeq$ (1-10) Gyr.

In order to construct a model which can achieve the goals of decaying dark matter there are certain criteria that need to be satisfied. The first and most

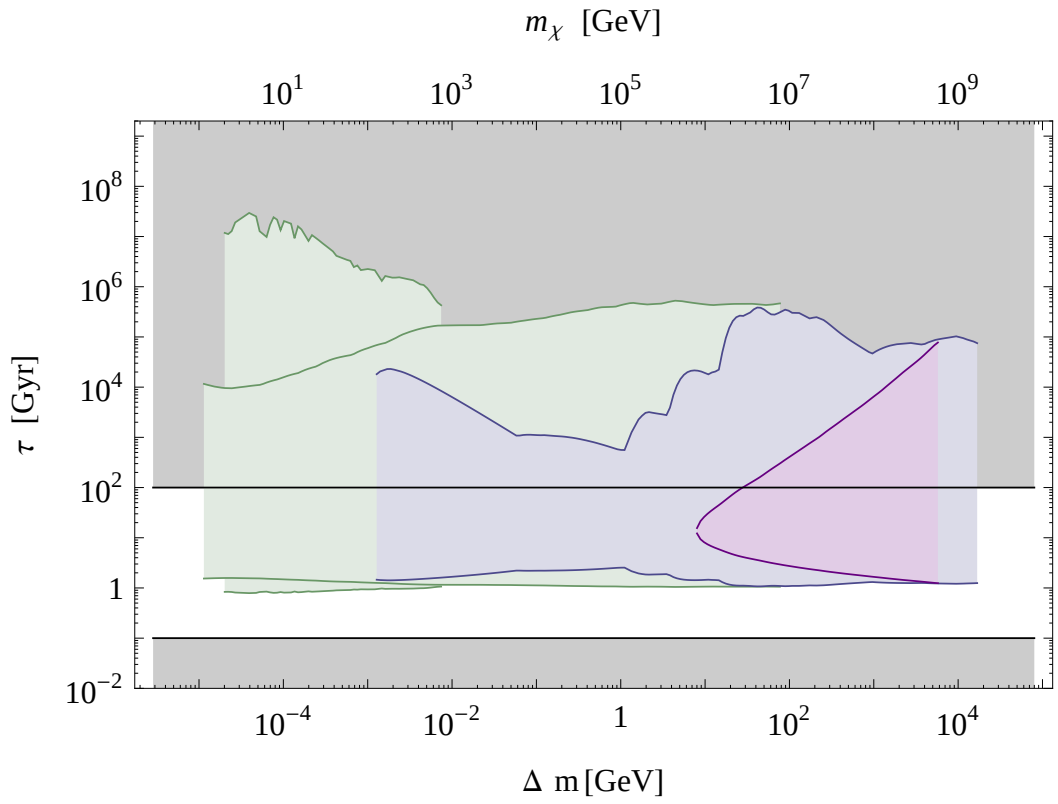

Figure 2.3: Constraints on DM lifetime τ as a function of mass splitting Δm and mass m_χ, for $\varepsilon = 10^{-5}$, for the decay channels $\chi^* \to \chi + \gamma$ (green) [4], $\chi^* \to \chi + e^- + e^+$ (blue) [5] and $\chi^* \to \chi + \nu + \bar{\nu}$ (purple) (this work). Color-shaded regions are excluded observation. The decays may have an observable effect on galactic halo structure if they occur at times 0.1Gyr $< \tau <$ 100Gyr$r$ [6, 7] (non-shaded region).

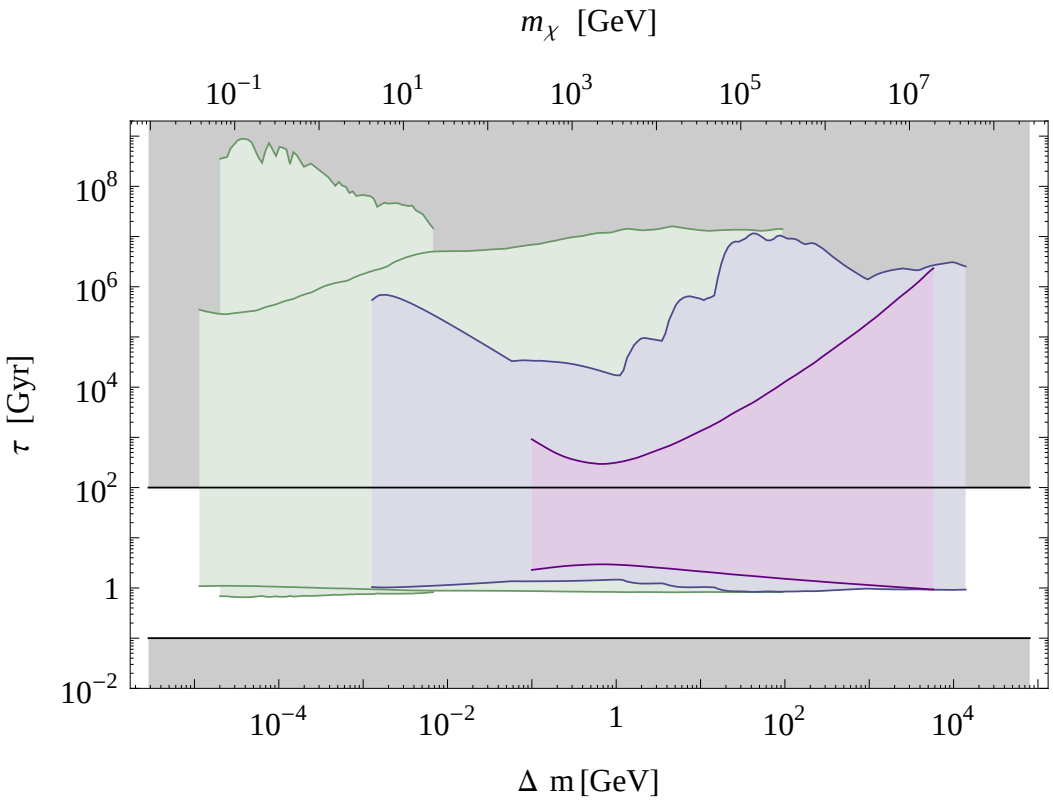

Figure 2.4: Same as in 2.3, but for $\varepsilon = 3 \times 10^{-4}$.

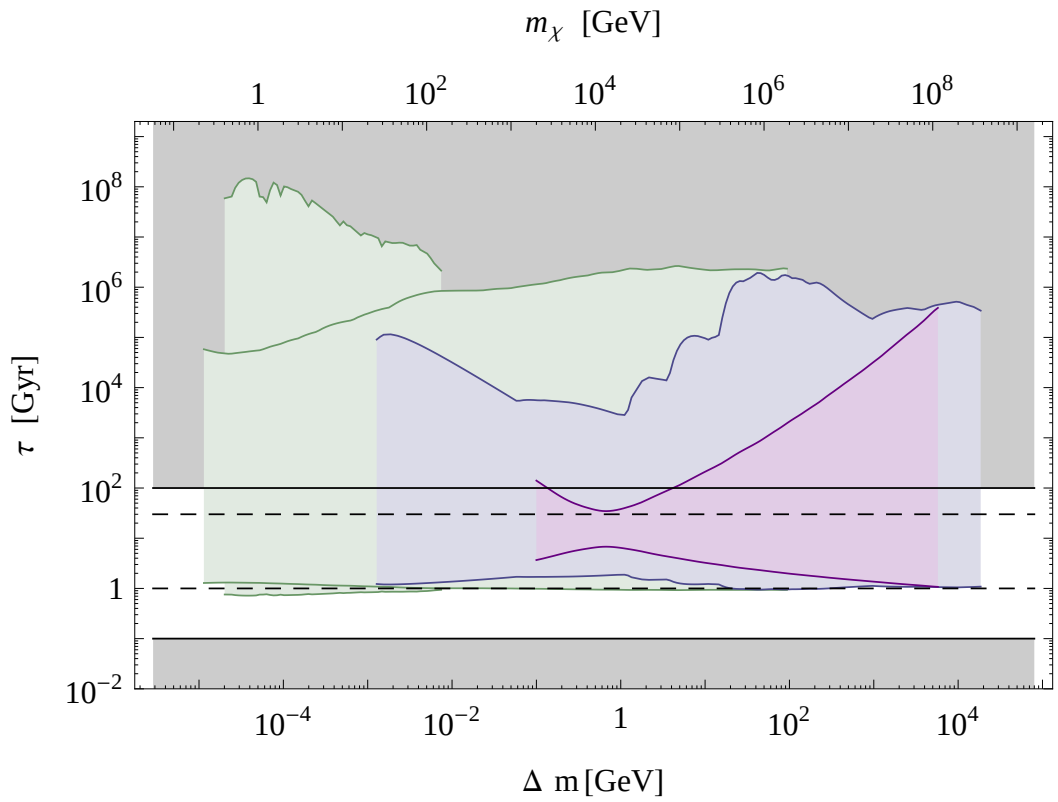

Figure 2.5: Same as in 2.3, but for $\varepsilon = 5 \times 10^{-5}$, suggested in [8] as suitable for resolving the missing-satellite problem. This would require a dark-matter lifetime within the narrower interval 1Gyr $< \tau <$ 30Gyr shown (dashed lines).

important of these is the need for two candidates with nearly degenerate masses. Second, we need decay of the parent DM particle to either light SM final states, or some new light degree of freedom. Third, the process needs to occur on time scales relevant for the disruption of structure formation, and lastly, we need some viable DM production mechanism. WIMP-like scenarios are particularly interesting on this front, as WIMPs are populated as thermal relics and naturally freeze out in the early Universe with the correct relic density.

Two scenarios will be considered. In the first we implement a variation of the "exciting dark matter" model conceived by Finkbeiner and Weiner [115], which involves the addition of a dark sector containing a Dirac fermion and a real scalar field to the standard model. The introduced fields obey a discrete $\mathbb{Z}_4$ symmetry, the breaking of which leads to a non-degeneracy of the masses of the fermion's two Weyl components, and an instability of the heavier to decay into the lighter. The scenario considered in this work differs from [115] in the values of the model parameters chosen; in short, we consider longer decay lifetimes.

As a second example, we consider a generalization of the scenario in [115], in which we replace the $\mathbb{Z}_4$ symmetry with a global $U(1)$ symmetry, requiring the introduced scalar field to be complex. The breaking of this $U(1)$ will produce a pseudo-Nambu-Goldstone boson, which will serve as our light final state for the dominant decay channel. We show that DM production through interaction with the SM is impossible in the $U(1)$ model. The second scenario is one example among any number of generalizations and extensions to the simple $\mathbb{Z}_4$ model; it is simply an illustration that decaying DM can be realized in a particle model irrespective of the strength of coupling to the SM.

In Section 2.3.1 we shall explore a model in which SM final states are produced in the dominant decay channel. In Section 2.3.2 we consider the possibility of completely non-SM final states. In Section 2.3.3 we discuss production, and in

Section 2.3.4 consider the possibility of χ^* depopulation. Section 2.4 focuses on constraints on the models and the available regions of parameter space.

2.3.1 SM Final States $(\mathbb{Z}_4)$

When searching for a light final state for the process in Eq. 2.1, the obvious place to look is the SM, as the existence of particles with masses substantially below the CDM mass scale (GeV) is assured. To couple the DM to the SM we adopt the model put forward in [115]. Although this was originally intended as a mechanism for explaining the observed INTEGRAL/SPI positron excess [138], with a different choice of parameters the model can serve our astrophysical aims quite well. We begin with the introduction of a Dirac fermion comprised of the two Weyl spinors $\chi_{1\mathrm{L}}$ and $\chi_{2\mathrm{R}}$, which couple to a real singlet scalar ϕ. The mass eigenstates for the χ_1 and χ_2 fields (which we will call χ and χ^*, respectively) are the DM in this model.

We impose a discrete $\mathbb{Z}_4$ symmetry under which the fields transform as

$$\begin{aligned} \chi_{1,2} &\rightarrow i\chi_{1,2}\,, \\ \phi &\rightarrow -\phi\,, \end{aligned} \tag{2.6}$$

but remain singlets under the symmetries of the SM. This allows for the following Lagrangian:

$$\begin{aligned} \mathcal{L} &= \frac{1}{2}\partial_\mu\phi\partial^\mu\phi + \sum_i^2 \chi_i^\dagger\sigma_\mu\partial^\mu\chi_i - m_D\overline{\chi_{1\mathrm{L}}}\chi_{2\mathrm{R}} \\ &- \lambda_1\phi\overline{\chi_{1\mathrm{L}}}(\chi_1)^c_{\mathrm{R}} - \lambda_2\phi\overline{\chi_{2\mathrm{R}}}(\chi_2)^c_{\mathrm{L}} - V(\phi, H, H^\dagger) + h.c.\,. \end{aligned} \tag{2.7}$$

At this stage the two mass eigenstates both have mass m_D. To lift this degeneracy we need to break the $\mathbb{Z}_4$ symmetry. We break the symmetry spontaneously down to $\mathbb{Z}_2$ by allowing ϕ to obtain a vacuum expectation value. The Higgs potential is

given by

$$\begin{aligned} V(\phi, H, H^\dagger) &= \frac{\lambda_\phi}{4}\phi^4 - \frac{\mu_\phi^2}{2}\phi^2 + \frac{\lambda_h}{4}\left(H^\dagger H\right)^2 \\ &- \frac{\mu_h^2}{2}H^\dagger H + \frac{\alpha}{2}\phi^2\left(H^\dagger H\right), \end{aligned} \tag{2.8}$$

where H is the SM Higgs doublet. The last term in Eq.2.8 is included as it is allowed by all the symmetries of the theory. Minimizing the above potential with respect to both ϕ and H we obtain the conditions

$$\begin{aligned} 2\lambda_\phi\langle\phi\rangle^2 - 2\mu_\phi^2 + \alpha\langle h\rangle^2 &= 0\,, \\ \lambda_h\langle h\rangle^2 - 2\mu_h^2 + 2\alpha\langle\phi\rangle^2 &= 0\,. \end{aligned} \tag{2.9}$$

It can now be clearly seen that $\langle\phi\rangle \neq 0$. As in [115], the spontaneous breaking of the discrete $\mathbb{Z}_4$ symmetry will lead to the formation of domain walls, which may be disfavored by observation. We can remove this potentially troubling phenomenon by introducing the explicit breaking term $\mu\phi^3$ to our Higgs potential, where μ is small for reasons of technical naturalness.

Perturbing Eq. 2.7 about the vacuum there arise Majorana masses $\lambda_1\langle\phi\rangle$ and $\lambda_2\langle\phi\rangle$ for χ_1 and χ_2, respectively. The Lagrangian therefore contains the mass matrix

$$\mathcal{L} \supset -\begin{pmatrix} \overline{\chi_{1_{\rm L}}} & (\overline{\chi_{2_{\rm R}}})^c \end{pmatrix} \begin{pmatrix} \lambda_1\langle\phi\rangle & \frac{m_{\rm D}}{2} \\ \frac{m_{\rm D}}{2} & \lambda_2^*\langle\phi\rangle \end{pmatrix} \begin{pmatrix} (\chi_{1_{\rm L}})^c \\ \chi_{2_{\rm R}} \end{pmatrix}, \tag{2.10}$$

which we then diagonalize to obtain the Majorana mass eigenstates χ and χ^*:

$$\begin{aligned} \chi &\simeq \frac{1}{\sqrt{2}}\left[(\chi_1+\chi_2)^c - (\chi_1+\chi_2)\right], \\ \chi^* &\simeq \frac{1}{\sqrt{2}}\left[(\chi_1+\chi_2)^c + (\chi_1+\chi_2)\right], \end{aligned} \tag{2.11}$$

whose masses we find to be

$$m_{\chi^*,\chi} = \frac{1}{2}\sqrt{m_D^2 + 4\lambda_-^2\langle\phi\rangle^2} \pm \lambda_+\langle\phi\rangle\,, \tag{2.12}$$

where $\lambda_\pm \equiv \frac{1}{2}(\lambda_1 \pm \lambda_2^*)$. We want the mass splittings to be small, so we choose $m_D \gg \lambda_\pm \langle\phi\rangle$, making $m_{\chi^*,\chi} \simeq \frac{m_D}{2} \pm \lambda_+\langle\phi\rangle$, and thus $m_{\chi^*}\epsilon = 2\lambda_+\langle\phi\rangle$. Typically in this model we shall consider masses in the range $m_{\chi,\chi^*} \sim (50\text{-}800)$ GeV, a breaking scale of $\langle\phi\rangle \sim (3\text{-}20)$ MeV, and coupling strength of $\lambda_\pm \sim 10^{-1}$ [implying $\Delta m \sim (0.4\text{-}8)$ MeV for $\epsilon \simeq (0.7\text{-}1) \times 10^{-5}$]. For a detailed discussion of the parameter space, see Section 2.4.

In the basis of the mass eigenstates, the Lagrangian contains the following interaction terms, which mediate decay, scattering, and annihilation processes:

$$\begin{aligned} \mathcal{L} \;\supset\; & \lambda_+\phi\overline{\chi}\chi \,-\, \lambda_+\phi\overline{\chi^*}\chi^* \,-\, \lambda_-\phi\overline{\chi}\gamma_5\chi^* \\ & - m_\chi\overline{\chi}\chi \,- m_{\chi^*}\overline{\chi^*}\chi^* \,+\, h.c.\,. \end{aligned} \tag{2.13}$$

It should be noted that interaction terms coupling like mass eigenstates are scalar, while off-diagonal coupling is pseudo-scalar. As will be seen this has a substantial effect on the DM decay rate.

Mixing of the SM sector with the dark sector (χ, χ^*, ϕ) occurs through the last term in Eq. 2.8. Expanding the Higgs potential about the vacua's of both ϕ and H produces off-diagonal mass terms for both fields. Expressing the potential in terms of the mass eigenstates ϕ' and h', we find the following mixing of states:

$$\begin{aligned} \phi \;&\simeq\; \cos\theta\,\phi' - \sin\theta\,h' \simeq \phi' - \theta\,h'\,, \\ h \;&\simeq\; \cos\theta\,h' + \sin\theta\,\phi' \simeq h' + \theta\,\phi'\,, \end{aligned} \tag{2.14}$$

where h is the SM Higgs boson, and λ_h is its self-coupling. To first order in α

$$\theta \simeq \frac{\alpha\langle\phi\rangle}{\lambda_h\langle h\rangle}\,, \tag{2.15}$$

and we find masses of ϕ' and h' to be

$$\begin{aligned} m_\phi^2 \;&\simeq\; 2\lambda_\phi\langle\phi\rangle^2\,, \\ m_h^2 \;&\simeq\; \frac{1}{2}\lambda_h\langle h\rangle^2\,, \end{aligned} \tag{2.16}$$

(in the limit $m_\phi \ll m_h$) with that of ϕ' being $\sim (2-20)$ MeV. At the time of this work the SM Higgs mass was not a known quantity, so we adopted the plausible value of $m_h \sim 130$ GeV. Replacing this with the value of $m_h = 125$ GeV recently measured by ATLAS and CMS at the LHC [139, 140], would not modify our conclusions substantially. Through ϕ-Higgs mixing, χ and χ^* can couple to h' and by extension the SM. In particular, it allows the possibility of decay into SM final states via processes such as that shown in Fig. 2.6.

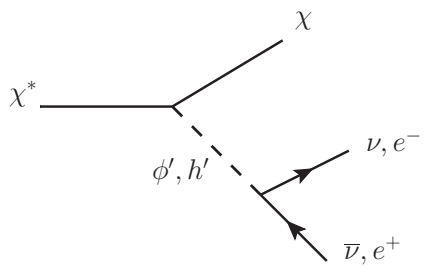

Figure 2.6: Primary DM decay channel for the $\mathbb{Z}_4$ model

This process has a decay rate given by

$$\Gamma \simeq \frac{\lambda_-^2\, y_l^2\, \theta^2}{2800\, \pi^3\, m_\phi^4}\, m_{\chi^*}^5 \epsilon^7\,, \tag{2.17}$$

where y_l is the Yukawa coupling for the dominant SM final state, and we assume $\Delta m \gg m_l$, $\lambda_+ \simeq \lambda_-$, and that the light final states are Dirac. Just as we choose our splitting to be small, we can choose the region of parameter space in which the lifetime is sufficiently large to disturb structure formation.

The above decay rate contains several elements which naturally lead to suppression and thus a long lifetime. First, the decay rate is subject to phase-space suppression, as there are 3 bodies in the final state. Second, it depends on the Yukawa coupling y_l, which, given we are only interested in decay into light leptons (e^+e^-, $\overline{\nu}\nu$), will be a small number. It is also dependent on the Higgs mixing angle

θ, which in turn varies depending on the strength of the coupling α. Although there is some freedom of choice with respect to the value of α, we typically take $\alpha \sim 10^{-5}$, which results in a mixing of $\theta \sim 10^{-9}$ (see Section 2.3.3 for details). Lastly, pseudo-scalar coupling between χ and χ^* means the decay rate contains a factor ϵ^7 (as opposed to ϵ^5 for scalar coupling). The conjunction of these factors means that the DM lifetime can be long without $\lambda_\pm$ being too small, typically $\lambda_\pm \sim 10^{-1}$.

2.3.2 Dark Decays $[U(1)]$

An advantage of SM final states is their detectability. While directly observable consequences are a desirable model building goal, the non-observation of the signatures of a model can lead to constraints, as will be seen in the next section. Were observational constraints to strengthen, there is the possibility that a non-observation of the final states in the above model may rule it out. Should this occur, the viability of decaying DM in general would rely on a primary decay channel to non-SM final states. In this section we will present a model which can realize this.

One way to naturally produce a decay channel with a light final state is to upgrade the discrete $\mathbb{Z}_4$ symmetry to a global $U(1)$ symmetry. Spontaneously breaking this will produce a Nambu-Goldstone boson (NGB) in the theory, which will couple to the DM. The Lagrangian in this scenario is similar to Eq.2.7 except that now $\phi = (1/\sqrt{2})(\phi_1 + i\phi_2)$, and $\chi_{1,2}$ and ϕ now transform under the $U(1)$ symmetry as

$$\begin{aligned} \chi_{1,2} &\rightarrow \chi_{1,2}\, e^{i\theta_\chi}\,, \\ \phi &\rightarrow \phi\, e^{-2i\theta_\chi}\,, \end{aligned} \tag{2.18}$$

where θ_χ is an arbitrary phase. The Higgs potential will have a similar form to

Eq. 2.8 but with $\phi \neq \phi^\dagger$, thus ϕ^2 terms become $\phi^\dagger\phi$. As with the discrete case, we end up with the mass matrix in Eq. 2.10 and subsequent mass eigenstates χ and χ^*; only now they couple to the mass eigenstates ϕ_1' and h', defined by

$$\begin{aligned} \phi_1 &\simeq \cos\theta_1\,\phi_1' - \sin\theta_1\,h' \simeq \phi_1' - \frac{\alpha\langle h\rangle}{\lambda_\phi\langle\phi\rangle}\,h'\,, \\ h &\simeq \cos\theta_1\,h' + \sin\theta_1\,\phi_1' \simeq h' + \frac{\alpha\langle h\rangle}{\lambda_\phi\langle\phi\rangle}\,\phi_1'\,, \end{aligned} \tag{2.19}$$

($m_\phi \gg m_h$ as will be seen) and the NGB ϕ_2, i.e.

$$\mathcal{L} \supset -\frac{\lambda_-}{\sqrt{2}}\phi_1'\overline{\chi}\gamma_5\chi^* - \frac{i\lambda_+}{\sqrt{2}}\phi_2\overline{\chi}\chi^* + h.c.\,. \tag{2.20}$$

It should be noted that the above coupling to the NGB is scalar, which results from the fact that ϕ_2 is the imaginary component of ϕ. This means that decays into the NGB contain less ϵ suppression (one power of ϵ) than they would were the coupling pseudoscalar (ϵ^3).

Coupling to the NGB implies the existence of long range DM-DM interactions, which can potentially affect structure formation. To avoid the issues involved with this, we will introduce a small soft breaking term, $\frac{\mu^2}{2}(\phi^2 + \phi^{\dagger 2})$ to the Higgs potential to explicitly break the continuous $U(1)$ symmetry down to the discrete $\mathbb{Z}_4$. This gives the NGB an $\mathcal{O}(\mu)$ mass, which is naturally small.

The off-diagonal interaction term in Eq. 2.20 leads to the decay channel $\chi^* \to \chi + \phi_2$, which has the decay rate

$$\Gamma \simeq \frac{\lambda_+^2}{4\pi} m_{\chi^*}\epsilon\,. \tag{2.21}$$

For the case where the primary decay of the DM was into SM final states, the reason for a long lifetime was the weak mixing with the SM and the suppression from the high power of ϵ. Should, however, the decay referred to in Eq. 2.21 be the primary channel, there is no such suppression, and we are forced to impose the additional approximate symmetry $\lambda_1 \simeq -\lambda_2^*$ to make $\lambda_+ \sim \mathcal{O}(10^{-18})$, hence

achieving $\tau \sim \mathcal{O}(\text{Gyr})$. As $\Delta m = 2\lambda_+\langle\phi\rangle$, small λ_+ implies a high breaking scale for reasonable values of the DM mass, roughly $\langle\phi\rangle \sim 10^{14}$ GeV. As will be discussed in Section 2.3.3, $\lambda_\phi \sim 1$ making $m_\phi \sim \langle\phi\rangle$ in this model.

This high scale has the potential to cause problems. Recall the minimization conditions in Eq. 2.9. In order to reproduce the correct breaking scale for the SM Higgs, either α needs to be small enough such that $\alpha\langle\phi\rangle^2$ is negligible with respect to μ_h^2, or we have a finely tuned scenario resembling the hierarchy problem of the SM, in which $\alpha\langle\phi\rangle^2$ and μ_h^2 are of similar order. The former, though the more natural of the two cases, precludes production via mixing with the SM, so we will entertain the latter for the time being.

2.3.3 Production

Both scenarios presented have all the required elements to disrupt structure formation in the desired fashion. All that is needed now is a production mechanism for the dark matter candidate in each scenario. As mentioned previously, one of the appealing properties of a WIMP is attainment of the correct relic abundance through thermal freeze-out from the bath in the early Universe.

$\mathbb{Z}_4$ Case

In the model presented in Section 2.3.1, χ couples to the SM through the Yukawa sector. It therefore follows that it is through these channels that it will maintain equilibrium with the SM prior to freeze-out. Production differs from the standard WIMP scenario in that it is a two-phase process. The ϕ is populated via interactions with the SM in the Higgs sector, while χ and χ^* are produced through their coupling to ϕ. At some temperature below the DM mass the ϕ-χ annihilation rate will drop below the expansion rate, and χ and χ^* will freeze out with respect to ϕ, fixing

the co-moving DM abundance to the standard value. We will now chronologically step through the processes leading to DM freeze-out.

The requirement that ϕ be in chemical equilibrium with the SM well before χ-ϕ freeze-out places a constraint on the allowed values of the coupling α. Well above the electroweak scale, the dominant process keeping ϕ in chemical equilibrium with the SM will be $hh \to \phi\phi$ (Fig. 2.7), which at temperatures well above the Higgs mass has the annihilation rate

$$\Gamma(hh \to \phi\phi) \simeq \frac{\alpha^2 T}{256\pi^3}\,. \tag{2.22}$$

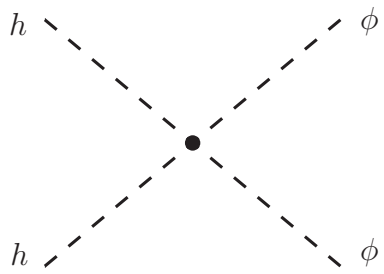

Figure 2.7: Dominant ϕ production mechanism for $T > m_h$.

This process will remain in equilibrium until $T < m_h$, and h production becomes Boltzmann suppressed, causing this ϕ production channel to become unavailable. For the DM masses of interest in this model (of order or below m_h), we require $\alpha > 10^{-6}$ to ensure that ϕ is in equilibrium at some point prior to ϕ-χ freeze-out.

Also contributing to ϕ production is the h-mediated processes $\overline{f}f \to \phi\phi$, which have the annihilation rate of

$$\Gamma(f\overline{f} \to \phi\phi) \simeq \frac{\alpha^2\, y_f^2\, \langle h\rangle^2\, T^3}{16\pi^3\, m_h^4}\,, \tag{2.23}$$

up to a color factor for processes involving quarks. The temperatures at which these processes freeze out depend on both the Higgs mixing α and SM fermion Yukawa

y_f. For the values of α considered in this paper ($\alpha \sim 10^{-5}$) the process which remains in equilibrium longest is that involving b quarks. This freezes out around the time at which the annihilation in Fig. 2.7 turns off. Thus the temperature at which ϕ freezes out with respect to the SM can be calculated to be $T_f^{\phi\text{-}SM} \sim 20$ GeV. This occurs when ϕ is still relativistic.

After ϕ-SM freeze out, the temperature of the ϕ-χ system will continue to track that of the background.[1] The DM will be kept in chemical equilibrium with ϕ through the scattering in Fig. 2.8, which in the non-relativistic limit has a cross section of

$$\sigma\, v_{rel} \simeq \frac{|\lambda_+|^4}{\pi\, m_\chi^2}\,. \tag{2.24}$$

This process will freeze out once the temperature of the ϕ-χ system falls below m_χ and the number density of χ becomes Boltzmann suppressed.

To determine the DM relic abundance we use the well established simplification of Eq. 1.27 adopted in [32], in which it is assumed g_{*s} is approximately constant, and $Y_{eq}(T_f) \gg 1$, that is

$$\Omega_\chi h^2 \;=\; 1.07 \times 10^9 \frac{x_{DM\text{-}f}\sqrt{g_*} GeV^{-1}}{g_{*s} m_{Pl} \langle\sigma\, v\rangle}\,, \tag{2.25}$$

where

$$\begin{aligned} x_{DM\text{-}f} \;&=\; m_\chi / T_f^{\phi\text{-}\chi} \;=\; \ln[0.038(g/\sqrt{g_*}) m_{Pl} m_\chi \langle\sigma\, v\rangle] \\ &\quad -\frac{1}{2}\ln\left[\ln[0.038(g/\sqrt{g_*}) m_{Pl} m_\chi \langle\sigma\, v\rangle]\right]\,, \end{aligned} \tag{2.26}$$

[1] Up to a factor $(g'_*/g_*)^{1/3}$, where g_* and g'_* are measures of the number of freedom in the bath at $T_f^{\phi\text{-}SM}$ and $T_f^{\phi\text{-}\chi}$ respectively. We will assume this ratio to be ~ 1, and $\sqrt{g_*} \simeq 10.8$, i.e. that all degrees of freedom are in equilibrium. While depending on the time of DM freeze out this might not be strictly true, the effect on the results will be negligible. It is therefore irrelevant exactly when ϕ freezes out with respect to the SM, as long as it has been in equilibrium at some point prior to ϕ-χ freeze out.

and $T_f^{\phi\text{-}\chi}$ is the temperature at which ϕ and χ drop out of chemical equilibrium. We find that typically $x_{DM\text{-}f} \sim 20$. The requirement that we produce the observed relic density of $\Omega_\chi h^2 \simeq 0.11$, places constraint on the free parameters λ_+ and m_χ should the DM be a thermal relic. See Section 2.4 for a full treatment of the parameter space. Given that $m_\chi \simeq m_{\chi^*}$ (and $\Delta m \ll T_f^{\phi\text{-}\chi}$) χ and χ^* will be produced in equal abundance.

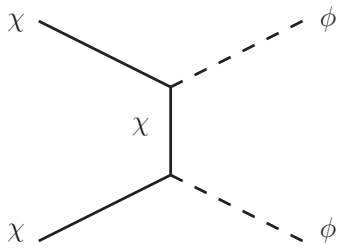

Figure 2.8: DM produced through ϕ annihilation.

After ϕ-χ freeze-out, the relativistic ϕ will remain with fixed abundance until the spontaneous breaking of the $\mathbb{Z}_4$ symmetry (at MeV scale). After symmetry breaking they become unstable to decay into photons via the loop order process depicted in Fig. 2.9 [141, 142]. This process has a rate of

$$\begin{aligned} \Gamma(\phi \to \gamma\gamma) &\simeq \frac{G_F\, \alpha_{EM}^2\, \theta^2\, M_W^4}{2\sqrt{2}\pi^3\, m_\phi} \\ &\simeq 4.5 \times 10^4 s^{-1} \left(\frac{\theta}{10^{-9}}\right)^2 \left(\frac{10MeV}{m_\phi}\right), \end{aligned} \tag{2.27}$$

which is large compared to the expansion rate, and ϕ rapidly depopulates.

In our calculation of the process depicted at tree level in Fig. 2.8, we have omitted the contribution from ladder diagrams involving ϕ exchange in the initial state. This approximation is valid at high energies, but begins to break down near freeze out, when the DM is in the moderate-nonrelativistic regime.

At low velocity the Yukawa potential (resulting from ϕ exchange) from one

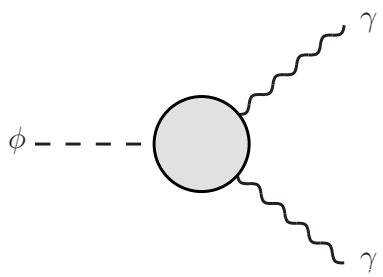

Figure 2.9: 1-loop order decay $\phi \to \gamma\gamma$, through h-ϕ mixing. Includes contribution from loops involving $W^{\pm}$, unphysical charged Higgs components $h^{\pm}$, and Fadeev-Popov ghosts.

initial state χ can significantly distort the wave-function of the other from that of a free particle. This leads to an enhancement of the velocity averaged cross section in an effect known as Sommerfeld enhancement [116, 143–145]. This effect can be taken into account by multiplying the relevant cross section by a velocity dependent Sommerfeld factor S. To calculate the enhancement to the process in Fig. 2.8 we follow the method of [143, 144], but find that in the relevant region of parameter space, S is close to 1 and the enhancement negligible. The enhancement generally becomes more important for larger values of Δm.

$U(1)$ Case

Production in the second model presented is slightly more difficult. An unfortunate consequence of a small Yukawa coupling is a weakening of the annihilation cross section (Fig. 2.8). This suppression ensures that the process in Fig. 2.8 is never in equilibrium, making thermal production of the DM impossible. This leads us to consider a nonthermal production mechanism, in which χ and χ^* are produced out of equilibrium through their weak mixing with the bath. Another possibility is production through direct coupling of the DM to the inflaton. While this is clean in

that it is independent of SM processes, it requires fine tuning to attain the correct relic abundance. For the time being we will entertain the former possibility.

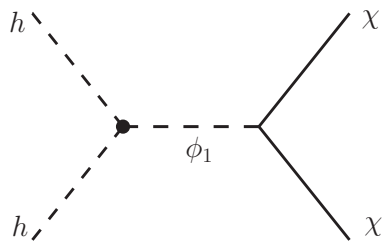

Figure 2.10: Dominant DM production mechanism in the $U(1)$ model.

The dominant channel through which production can occur is through the SM Higgs annihilation pictured in Fig. 2.10. As $\langle\phi\rangle$ is large in this model, we expect this process to be strongest above the electroweak breaking scale. At these high temperatures finite temperature effects come into the Higgs potential at loop order [146–148]. This has the effect of giving the scalar components of the SM Higgs doublet, temperature-dependent masses of the form

$$m_h^2 \simeq \frac{\lambda_h T^2}{24}\,. \tag{2.28}$$

The process in Fig. 2.10 goes to a maximum near the ϕ_1' resonance, which also coincides with $m_{\phi_1}^2 \simeq 4m_h^2$. Granted $\alpha^2 \ll \lambda_\phi$, and following the analysis of [94], the velocity averaged cross section can, in this region, be well approximated by

$$\langle\sigma v\rangle \simeq \frac{\lambda_+^2 T m_\phi^3}{\pi^3 (n_h^0)^2} K_1\left(\frac{m_\phi}{T}\right) \times \frac{\frac{\alpha^2}{\lambda_\phi}\sqrt{m_\phi^2 - 4m_h^2}}{\left[\left(\frac{\alpha^2}{\lambda_\phi}\sqrt{m_\phi^2 - 4m_h^2} + \lambda_\phi m_\phi\right)\coth\left(\frac{m_\phi}{4T}\right) + 128\lambda_+^2 m_\phi\right]}\,. \tag{2.29}$$

To avoid Boltzmann suppression in Eq. 2.29 we will take λ_ϕ to be small for now ($\lambda_\phi \sim 10^{-17}$), which implies that m_{ϕ_1} is far below the $U(1)$ breaking scale

($m_{\phi_1} \sim 100$ TeV). In order to calculate the abundance at a particular temperature, we must solve the Boltzmann equation, which can be expressed in the form

$$\frac{dn_\chi(T)}{dT} - \frac{3}{T} n_\chi(T) = -\frac{(n_h^0)^2}{HT} \langle \sigma v \rangle \,, \tag{2.30}$$

and has the solution

$$n_\chi(T) \;=\; T^3 \int_T^{T_{n_\chi=0}} \frac{(n_h^0)^2 \langle \sigma v \rangle}{HT'} dT' \,, \tag{2.31}$$

where $T_{n_\chi=0} \simeq \sqrt{6/\lambda_h}$ is defined by the temperature at which $m_{\phi_1}^2 \simeq 4m_h^2$, and will be taken to be the temperature at which significant production starts.

For the representative region of parameter space $\lambda_\phi \sim 10^{-17}$, $\alpha \sim 10^{-15}$, $\lambda_+ \sim 10^{-18}$, and $\tau_{\chi^*} \sim 1$ Gyr, the co-moving number density can be calculated to be $\mathcal{O}(10^{-27})$, roughly 17 orders of magnitude below the required value at that temperature. These values for the parameters in the model were chosen as they were shown to maximize production. As this channel is expected to be the strongest available it is therefore clear that production of the DM via mixing with the SM in such a model is impossible. The implication of neither a SM final state nor SM related production is the decoupling of the dark sector from the visible. This gives us complete freedom in the choice of dimensionless parameters α and λ_ϕ but precludes entirely the possibility of direct verification of the model. We can now choose $\lambda_\phi \sim 1$ and α to be very small to avoid issues of fine-tuning.

Decoupling of the dark sector from the SM implies the necessity for some novel DM production mechanism. As mentioned earlier this can be realized through a direct coupling of the DM to the inflaton, but as stated, such a mechanism is problematic as it is difficult to obtain a relic density of a similar order to that of the SM without fine-tuning of the DM-inflaton coupling.

2.3.4 Depopulation of the Excited State

In the $\mathbb{Z}_4$ model, as the temperature of the ϕ-χ system drops well below the DM mass, χ and χ^* will have chemically frozen out, fixing the relic abundance. The s-channel equivalent to Fig. 2.8 will, however, maintain kinetic equilibrium in the ϕ-χ system to temperatures down as low as m_ϕ [143, 149]. Both χ and χ^* will be kept in equilibrium with each other by way of a process like that in Fig. 2.11, causing both to track closely the temperature of the background. However, as the average kinetic energy drops below Δm, the process $\chi\chi \to \chi^*\chi$ is no longer kinematically viable, and the up-scattering rate becomes Boltzmann suppressed [149]. The result is a rapid depopulation of χ^*, and an absence of the heavy state so important for disturbance of structure formation. This issue can be averted should the scattering rate for Fig. 2.11 be small enough such that the process freezes out sufficiently early, i.e for $T \gg \Delta m$. Should this be the case, both the forward and back scattering processes will cease well before depopulation becomes an issue.

The cross section for this process (at tree level) can be calculated to be

$$\sigma v_{rel} \;\simeq\; \frac{3|\lambda_-\lambda_+|^2}{\pi m_{\chi^*}^2}\frac{1}{v_{rel}}\log\left[\frac{32}{v_{rel}^2}\right], \tag{2.32}$$

in the limit $m_\phi^2 \ll m_{\chi^*}\Delta m$, which is justified in the region of parameter space considered (see Section 2.4). In the moderate to nonrelativistic regime, the scattering rate for process $\chi^*\chi \to \chi\chi$ is given by

$$\Gamma \;\simeq\; (n_\chi)\,\frac{x_{sc\text{-}f}^{3/2}}{2\sqrt{\pi}}\int_0^1 (\sigma v_{rel})\,S\,v_{rel}^2\,e^{-x_{sc\text{-}f}v_{rel}^2/4}\,dv_{rel}, \tag{2.33}$$

where $x_{sc\text{-}f} = m_\chi/T_f^{\chi\text{-}\chi^*}$, and $T_f^{\chi\text{-}\chi^*}$ is defined as the temperature at which the process in Fig. 2.11 freezes out.

After the process in Fig. 2.8 freezes out, the comoving DM number density

n_χ/T^3 is fixed, and is given by

$$n_\chi/T^3 \simeq \frac{g_{*s}}{m_\chi} 3.76 \times 10^{-11}\,\text{GeV}\,, \tag{2.34}$$

where T is the temperature of the bath. We can now choose parameters such that the process in Fig. 2.11 freezes out around the same time as that of Fig. 2.8, in which case Eq. 2.24 and Eq. 2.32 are of a similar order. In the relevant region of parameter space, this is generally the case, with $x_{sc\text{-}f} \sim 1$. Interestingly, this is before ϕ-χ freeze-out, meaning χ and χ^* are both in equilibrium with ϕ but not with each other.

In the above, we have considered only the depopulation of χ^* in the early Universe. It is also important that χ^* not be depopulated via scattering in the late Universe, when Sommerfeld effects are significant. In fact, additional constraints on $\chi\chi$ and $\chi\chi^*$ scattering arise from the requirement that self-scattering of DM does not significantly perturb galactic halo shapes [9]. These requirements will be taken into account in Section 2.4.

In the $U(1)$ model there are no such depopulation issues, as λ_+ is very small and the DM is never in equilibrium in the first place.

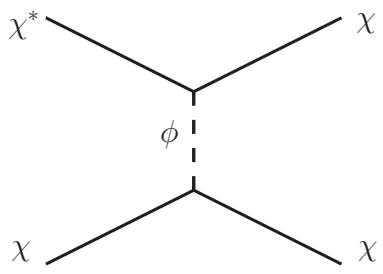

Figure 2.11: Process by which χ and χ^* maintain chemical equilibrium.

2.4 Constraints on $\mathbb{Z}_4$ model

Up to this point there has been minimal discussion of the choice of values for the many free parameters in our model. We begin by highlighting the constraints on those parameters. There are initially 7 independent free parameters, those related to the fermions χ and χ^*, namely, m_{χ^*} and $\lambda_\pm$, and those belonging to the Higgs sector: λ_ϕ, α, μ_ϕ, and μ. Recall also that we can express the mass splitting in terms of these parameters, that is, $\Delta m = 2\lambda_+\langle\phi\rangle$ [$\langle\phi\rangle$ depends on Higgs potential parameters from Eq. 2.9]. Thus when we parametrize Δm in terms of ϵ ($\Delta m = m_{\chi^*}\epsilon$) and fix its value to $\epsilon = 10^{-5}$, we place a constraining relationship between λ_+, m_{χ^*}, and $\langle\phi\rangle$. As a second constraint we will impose $\lambda_+ \sim \lambda_-$, as they will only differ greatly in the finely tuned scenario where $\lambda_1 \simeq \pm\lambda_2$ to high precision. Finally, we must satisfy the condition in Eq. 2.25, to ensure correct relic abundance. These three constraints reduce the number of free independent parameters to 4, which can be taken to be $\langle\phi\rangle$, λ_ϕ, α, and μ. We can now express allowed values of Δm as a function of breaking scale $\langle\phi\rangle$ for chosen vales of α and λ_ϕ. We must choose α appropriately such that ϕ goes into equilibrium with the bath before the temperature of DM freeze-out. The allowed values of Δm for the appropriate DM lifetimes are plotted on the left hand side of Figs. 2.12-2.13, while the corresponding values of m_{χ^*} (for $\epsilon = 10^{-5}$ and $\epsilon = 0.7 \times 10^{-5}$ for Figs. 2.12 and 2.13, respectively) are plotted on the right.

The presence of readily detectable charged particles in the final state increases the possibility of indirect detection. Indeed, heavy constraints can be placed on the parameter space based on non-observation of the consequences of such a final state. As outlined in Section 2.2, astrophysical fluxes can be used to place limits on the relevant parameters τ_{DM} and Δm, as seen in Figs. 2.3-2.5. We have translated the constraints on decay to e^+e^- from Fig. 2.5, to the parameter space relevant

to this model, resulting in the exclusion region in Fig. 2.12.

Which leptons will be predominantly produced will depend not only on the choice of parameters (i.e. for which lepton does $\Delta m \geq 2m_l$ hold) but also the choice of neutrino model. We will consider three distinct possible final states: (i) e^+e^-, i.e. $\Delta m \geq 2m_e$ for Dirac neutrinos, (ii) $\nu\overline{\nu}$, i.e. $\Delta m < 2m_e$ for Dirac neutrinos, and (iii) $\nu\overline{\nu}$ for Majorana neutrinos.

(i) If we consider the SM neutrino to be a Dirac particle, then the upper bound on light neutrino masses implies a Yukawa coupling of $y_\nu \lesssim 10^{-11}$ [150]. Thus when decays into charged leptons are kinematically allowed ($\Delta m \geq 2m_e$), their relatively large coupling in the Yukawa sector will render decays into neutrinos subdominant. There is the important constraint that $\Delta m < 2m_\mu$, as should $\mu^+\mu^-$ pairs be produced, their Yukawa is large enough that for no allowed values of Δm and $\langle\phi\rangle$ would $\tau_{\chi^*} >$ 0.1 Gyr. Thus for $\Delta m \geq 2m_e$, decays to e^+e^- will dominate. A representative region of parameter space can be seen in Fig. 2.12. To obtain the correct relic abundance, parameters must lie on the dashed line. We find that for $m_\chi \sim$ 600 GeV, the breaking scale $\langle\phi\rangle$ is required to be in the $\sim$ 10 MeV range, while (for $\epsilon = 10^{-5}$) Δm is in the MeV. It should be noted that these parameters coincide with an $x_{sc\text{-}f} \sim 1$, which is well above $T_f^{\chi\text{-}\chi^*} \sim \Delta m$, removing the possibility of depopulation of the heavier DM state.

Interestingly, the (1-30) Gyr lifetime range preferred by Abdelqader and Melia [8] has been nearly completely excluded for decays into charged particles, leaving only the restrictive region of (0.1-1) Gyr available. However, should decays to neutrinos dominate, we can avoid this exclusion region entirely.

(ii) Should $\Delta m < 2m_e$ only neutrinos are kinematically available. As Dirac neutrinos couple only very weakly with the SM Higgs, the lifetime of the DM will be too long to affect structure formation. There are two ways in which we could reduce τ_{χ^*}, by either increasing α or decreasing m_ϕ. We find, however, that for

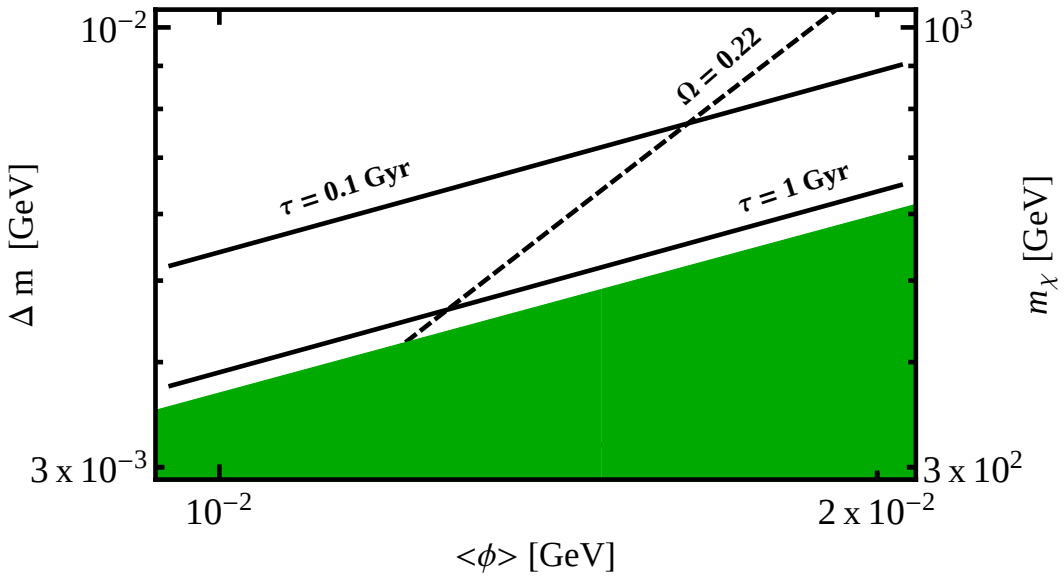

Figure 2.12: Available parameter space for decays into e^+e^- ($y_l = y_e$) for $\lambda_\phi = 1$ and $\alpha = 10^{-5}$ for lifetimes $\tau_{\chi^*} = 0.1$ Gyr (solid black upper line), and $\tau_{\chi^*} = 1$ Gyr (solid black lower line). Parameters yielding correct freeze-out abundance lie on the dashed black line. Shaded is the exclusion region from [5]. We have chosen $\epsilon = 10^{-5}$.

$m_\phi > \Delta m$, there are no values of α and m_ϕ that can yield a lifetime short enough. If, however, $m_\phi \lesssim \Delta m$, the process $\chi^* \to \chi + \phi'$ becomes kinematically allowed. The rate for this process does not contain the high level of suppression that decays into SM final states suffer, and we find its lifetime to be $\ll 0.1$ Gyr, dominating over decays into $\nu\overline{\nu}$. Thus for the parameter choice $m_\phi > \Delta m$, the DM lifetime is too long, while for $m_\phi \lesssim \Delta m$, $\nu\overline{\nu}$ final states are unimportant, and τ_{χ^*} is far too short. It therefore seems that in no region of parameter space can decays into Dirac neutrinos affect structure formation.

(iii) Should we introduce Majorana masses for the ν_{R} and employ the type I see-saw mechanism, we have the freedom to make y_ν large enough (while still keeping

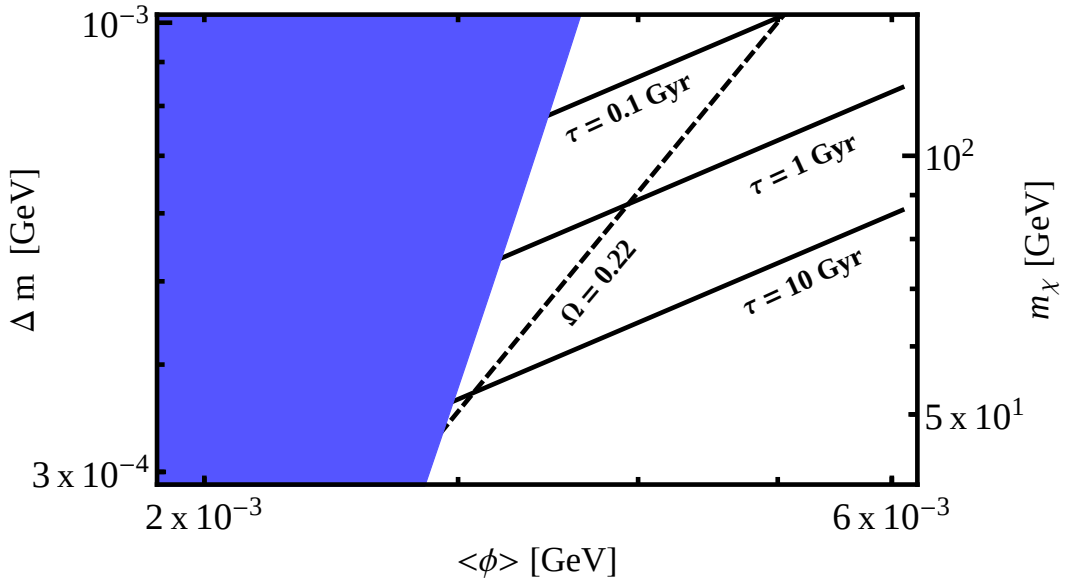

Figure 2.13: Available parameter space for decays into $\overline{\nu}\nu$ with a larger Yukawa of $y_\nu \simeq 10^{-4}$ (ν are Majorana) for $\lambda_\phi = 0.8$ and $\alpha = 10^{-5}$ for lifetimes $\tau_{\chi^*} = 0.1$ Gyr (solid black upper line), $\tau_{\chi^*} = 1$ Gyr (solid black center line) and $\tau_{\chi^*} = 10$ Gyr (solid black lower line). Parameters yielding correct freeze-out abundance lie on the dashed black line. Shaded is the exclusion region based on ellipticity constraints [9]. We have chosen $\epsilon = 0.7 \times 10^{-5}$.

the neutrino mass small) to cause decays with neutrino final states to dominate without the need for fine-tuning m_ϕ. We can consider three options: $y_\nu^2 \ll y_e^2$, $y_\nu^2 \simeq y_e^2$, and $y_\nu^2 \gg y_e^2$. Should $y_\nu^2 \simeq y_e^2$ or $y_\nu^2 \ll y_e^2$, decays into electrons are either important or dominate, causing the allowed parameters to be the same as for the Dirac case. However, for $y_\nu^2 \gg y_e^2$, neutrino final states are dominant for all values of Δm, and while we still need to respect the observational constraints in Fig. 2.12, we have a wider parameter space available, an example of which can be seen in Fig. 2.13.

Conversely to the Dirac case, having $\Delta m \geq 2m_e$ makes $\tau_{\chi^*} > 0.1$ Gyr impos-

sible, as the Yukawa controlling the decay is much larger than that of the electron. This constraint requires us to choose much smaller values of m_ϕ than for e^+e^- final states, if we wish to maintain thermal production. The smaller the value of m_ϕ, the larger the χ-χ cross section in present-day halos. In [9] authors argued that to maintain the observed ellipticity in galactic halos, the timescale for DM self-interactions must be longer than the halo age ($\Gamma^{-1}_{DM-DM} > 10^{10}$ yr). Following the approach in [9] constraints were placed on our parameter space, resulting in the shaded exclusion region in Fig. 2.13.

2.5 Conclusions

Models for decaying dark matter are interesting in that they maintain the attractive features of the ΛCDM model, while alleviating the issues pertaining to the over prediction of small scale power. In this work we investigated the class of DM models in which decay occurs via the process $\chi^* \to \chi + l$ where χ^* and χ are nearly degenerate in mass (in this work we chose $\Delta m/m_{\chi^*} \equiv \epsilon = 10^{-5}$) and l is relativistic. We reviewed constraints on the class of model in which l is either a γ ray photon or an $e^\pm$ pair, and derived constraints on the scenario in which l is a pair or neutrinos. We then went on to investigate two examples of specific particle physics models to test the theoretical viability of the decaying dark matter scenario.

In the first scenario, we considered the possibility of decays into SM final states. We demonstrated that through the breaking of a discrete $\mathbb{Z}_4$ symmetry with the real scalar field ϕ, we could produce two Majorana DM candidates χ^* and χ with non-degenerate mass, and allow for the decay channel $\chi^* \to \chi + \mathrm{SM}$. The required long lifetime ((0.1-100) Gyr) was naturally achieved, as the the decay rate was suppressed by ϵ, by small Yukawa couplings, and by the small mixing between

SM-sector and dark-sector particles.

The only two viable decay modes involving SM final states were $\chi^* \to \chi + e^+e^-$ and $\chi^* \to \chi + \overline{\nu}\nu$, where the later is possible only in the case of Majorana neutrinos. We found that for DM masses in the range (50-800) GeV ($\Delta m \simeq (0.4 - 8)$ MeV) and for a ϕ-Higgs mixing of $\alpha \simeq 10^{-5}$, all required criteria, including thermal production, could be met if the $\mathbb{Z}_4$ symmetry was broken at the MeV scale, with $\langle\phi\rangle \simeq (3-20)$ MeV ($m_\phi \simeq (2-20)$ MeV). Interestingly, in applying the constraints on decays to e^+e^- derived in [5], we showed that this final state is almost excluded for DM lifetimes in the (1-30) Gyr range preferred in [8]. Dirac neutrinos were unable to fulfill the requirements for decaying DM, as their Yukawa coupling is too small. Thus decays to Majorana neutrinos are preferred by such DM decay models, as they are not constrained to either the short lifetimes applicable for e^+e^- decays, or the small Yukawa couplings of Dirac neutrinos.

In the second scenario, we considered the possibility of non-SM final states. This was achieved by replacing the discrete $\mathbb{Z}_4$ symmetry with a continuous $U(1)$ symmetry. Breaking of the $U(1)$ symmetry led to a pseudo-Nambu-Goldstone boson, which became the light final state produced in decays. As the DM decay process was no longer strongly suppressed, we were forced to finely tune model parameters to obtain a DM lifetime in the correct range. A consequence of this fine tuning was that DM production via mixing with the SM was no longer possible. In this scenario, the dark and visible sectors are almost decoupled from each other. Though aesthetically less appealing, this model demonstrates the feasibility of decaying dark matter, independent of the strength of coupling to the SM.

3

Electroweak Bremsstrahlung and the Lifting of Helicity Suppression

A certain class of models for Majorana dark matter contains helicity suppression of the s-wave annihilation cross section. In these models, the leading order contribution to the annihilation cross section is from the velocity suppressed p-wave component, leading to suppressed annihilation today.

As has long been known, the bremsstrahlung of a photon during annihilation can lift the helicity suppression [151–156], causing the $2 \to 3$ bremsstrahlung process to dominate over the leading order $2 \to 2$ process. In this work we demonstrate that a similar effect can be achieved by the bremsstrahlung of electroweak gauge bosons.

We begin by briefly describing the origin of helicity suppression in Section 3.1, and present an example of a model which contains this issue. In Section 3.2 we outline the lifting of suppression via bremsstrahlung processes, and perform an explicit calculation of the W-strahlung cross section to demonstrate this fact.

3.1 Helicity Suppression in Dark Matter Annihilation

In certain models for Majorana dark matter, there is a mismatch between the allowed helicities of the initial and final states for dark matter annihilation via an s-wave into light fermions. This leads to a suppression of the s-wave annihilation cross section, causing p-wave processes to dominate. Helicity suppression will be discussed in more detail in Section 3.1.1, with an example of a model containing suppressed annihilations presented in Section 3.1.2.

3.1.1 Origin of Suppression

The cross section for an annihilation process can be expanded in powers of v^2

$$\sigma v = \sum_L a_L v^{2L}, \tag{3.1}$$

in which v is the velocity of the annihilating particles in the Center of Momentum (CoM) frame. Dark matter in the galactic halo is non-relativistic, having a virial velocity of $v \sim 10^{-3}$ (in units of c). This implies that the cross section can be well approximated by the lowest order terms in Eq. 3.1,

$$\sigma v \simeq a_0 + a_1 v^2. \tag{3.2}$$

Given the high level of velocity suppression in $a_1 v^2$ relative to a_0 ($\sim 10^{-6}$), one would expect the cross section to be dominated by a_0, which is purely s-wave ($L = 0$). This is generally the case, but for a subset of models in which the s-wave contribution is suppressed.

If the dark matter is a Majorana fermion, the initial state in the annihilation $\chi\chi \to SM$ must be odd under particle-antiparticle exchange. Therefore, an even

L state implies an antisymmetric spin state. Thus for a purely s-wave annihilation $L = 0$ and $S = 0$, so $J = S + L = 0$, and the DM necessarily has to annihilate into a $J = 0$ final state[1]. This turns out to be problematic for annihilations of the type $\chi\chi \to f_{\rm L} + \overline{f}_{\rm R}$, where f is a Dirac fermion for which $m_f \ll m_\chi$ (subscripts refer to their chiral states). Given f is much lighter than χ, the annihilation products in this interaction will be highly relativistic. In the relativistic limit the chiral and helicity eigenstates correspond, implying that $f_{\rm L}$ is required to be in a left handed helicity eigenstate. Being an antiparticle, $\overline{f}_{\rm R}$ is necessarily in a right handed helicity eigenstate. Thus in the CoM frame, in which f and $\overline{f}$ are produced back to back, the final state for the interaction $\chi\chi \to f_{\rm L} + \overline{f}_{\rm R}$ necessarily has $S = 1$ in the relativistic limit. The s-wave process therefore has $J = 1$ in the final state, which is at odds with the requirement that the initial state has $J = 0$. The helicity and chirality eigenstates are only approximately equal, with the R-chiral component of the L-helicity state suppressed by a factor of $(m_f/m_\chi)^2$, leading to a $(m_f/m_\chi)^2$ suppression of the s-wave annihilation rate. Thus in the relativistic limit, a_0, the purely s-wave piece of Eq. 3.2, vanishes. The leading order piece in the limit $m_f/m_\chi \ll v$ is therefore the p-wave contribution to Eq. 3.2, which has a large degree of velocity suppression.

3.1.2 An Example Of Suppressed Annihilation

To illustrate our arguments, we choose a simple example out of the class of models under discussion. This is provided by the leptophilic model proposed in Ref. [157, 158]. Here the DM consists of a gauge-singlet Majorana fermion χ,

[1]Similar arguments apply to the case in which χ is a scalar field, as the state $\chi\chi$ trivially has $S = 0$.

which annihilates to leptons via the $SU(2)$-invariant interaction term

$$f\left(\nu\,\ell^{-}\right)_{L}\,\varepsilon\begin{pmatrix}\eta^{+}\\ \eta^{0}\end{pmatrix}\chi+h.c.=f(\nu_{L}\eta^{0}-\ell_{L}^{-}\eta^{+})\chi+h.c., \tag{3.3}$$

where f is a coupling constant, ε is the 2×2 antisymmetric matrix, and $(\eta^{+}$, $\eta^{0})$ is a new $SU(2)$ doublet scalar. In this model, DM annihilation to fermions is mediated by t and u channel exchange of the η fields.

A similar coupling occurs in supersymmetry if we identify χ with a neutralino and η with a sfermion doublet. In fact, the implementation of supersymmetric photinos as dark matter by H. Goldberg provided the first explicit calculation of s-wave suppressed Majorana dark matter annihilation to a fermion pair [159]. Therefore, much of what we discuss below is also relevant for neutralino annihilation to fermions via the exchange of sfermions. However, the class of models for which the $2\to 2$ annihilation is helicity suppressed is more general than the class of supersymmetric models.

The cross section for the $2\to 2$ process $\chi\chi\to e^{+}e^{-}$ or $\nu\overline{\nu}$ is given by

$$v\,\sigma=\frac{f^{4}v^{2}}{24\pi\,m_{\chi}^{2}}\,\frac{1+\mu^{2}}{(1+\mu)^{4}}\,, \tag{3.4}$$

where $m_{l}\simeq 0$ and $m_{\eta^{\pm}}=m_{\eta^{0}}$ have been assumed, and $\mu=m_{\eta}^{2}/m_{\chi}^{2}$. The suppressions discussed above are apparent in Eq. 3.4. The helicity suppressed s-wave term is absent in the $m_{l}=0$ limit, and thus only the v^{2}-suppressed term remains.

3.2 Lifting Suppression with Electroweak Bremsstrahlung

As discussed in the previous section, the inconsistency between the chirality of the final state fermions and their allowed spin state, leads to the suppression of purely s-wave contributions to $\chi\chi\to f_{\rm L}+\overline{f}_{\rm R}$. This mismatch can be alleviated by

the presence of an $S = 1$ particle in the final state. If, for example, we consider the bremsstrahlung of a gauge boson during the process $\chi\chi \to f_{\rm L} + \overline{f}_{\rm R}$, that is, $\chi\chi \to f_{\rm L} + \overline{f}_{\rm R}$ + gauge boson, the gauge boson can carry away a unit of angular momentum, allowing the final state to have $J = 0$ without requiring a spin/helicity mismatch for $f_{\rm L} f_{\rm R}$. In this way the helicity suppression of the purely s-wave contribution to the $\chi\chi \to f_{\rm L} + \overline{f}_{\rm R}$ annihilation process is lifted, and cross section no longer suffers from velocity suppression at leading order in v. This has been long understood in the context of photon bremsstrahlung [151–156].

For heavy χ, the bremsstrahlung of electroweak gauge bosons becomes kinematically allowed. The contribution from such processes should be significant, as has been recognized in Refs. [160–168]. The purpose of this work is to carry out an explicit calculation of the cross section for the process $\chi\chi \to \nu_{\rm L} + e^+_{\rm R} + W^-$ to leading order in v, and verify that it does not contain helicity or velocity suppression, that is, the cross section does not vanish in the limit $v/m_l \to 0$. This is a re-visitation of the calculation performed in Ref. [160], which was found to be in error. In order to perform this calculation, we implement the toy model outlined in Section 3.1.2, which allows for the annihilation processes pictured in Fig. 3.1. Sections. 3.2.1-3.2.2 will focus on the details of the calculation, with the results outlined in Sections. 3.2.4 and 3.2.5. In Section 3.2.6 we consider the generalization of this process to Z boson bremsstrahlung, and hence calculate the total cross section in Section 3.2.7, taking into account contributions from all colourless gauge bosons.

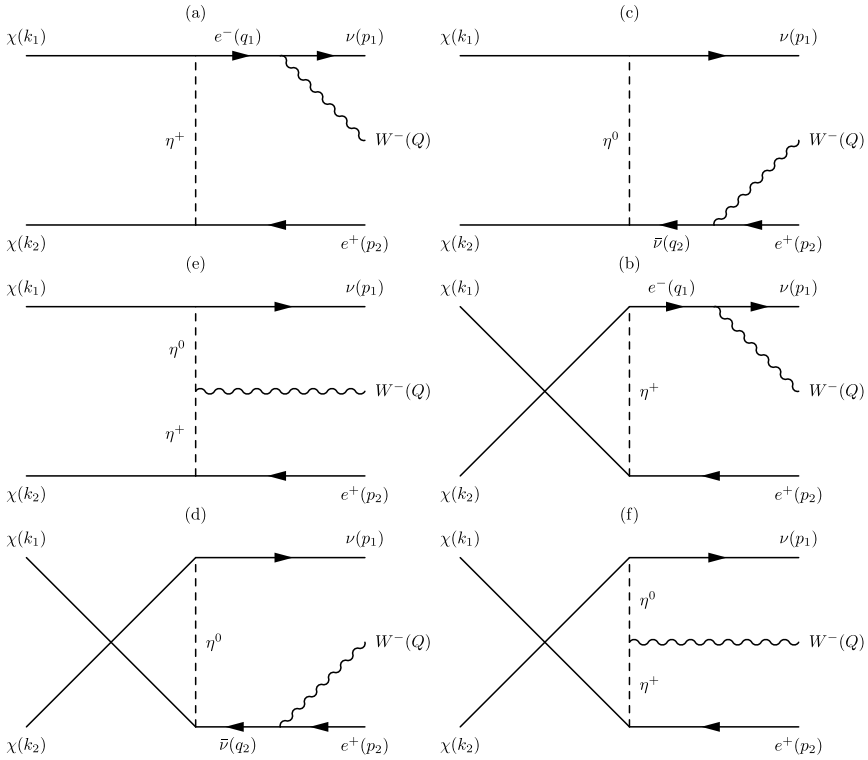

Figure 3.1: The t-channel ((a),(c), and (e)) and u-channel ((b), (d) and (f)) Feynman diagrams for $\chi\chi \to e^+\nu W^-$. Note that t- and u-channel amplitudes are simply related by the $k_1 \leftrightarrow k_2$ interchange symmetry. All fermion momenta in the diagrams flow with the arrow except p_2 and q_2, with $q_1 = p_1 + Q$, $q_2 = p_2 + Q$.

3.2.1 W-strahlung Matrix Elements

We begin the calculation by writing down the matrix elements for the 6 diagrams in Fig. 3.1. In the limit $m_l \simeq 0$, and assuming that $m_{\eta^\pm} = m_{\eta^0}$, they are given by

$$\begin{aligned}
\mathcal{M}_a &= i\frac{f^2 g}{\sqrt{2}}\frac{1}{q_1^2}\frac{1}{t_1 - m_\eta^2} \\
&\quad \times (\bar{v}(k_2)P_L v(p_2))(\bar{u}(p_1)\gamma^\mu P_L \not{q}_1 u(k_1))\epsilon_\mu^Q, \qquad (3.5)\\
\mathcal{M}_b &= i\frac{f^2 g}{\sqrt{2}}\frac{1}{q_1^2}\frac{1}{u_1 - m_\eta^2} \\
&\quad \times (\bar{v}(k_1)P_L v(p_2))(\bar{u}(p_1)\gamma^\mu P_L \not{q}_1 u(k_2))\epsilon_\mu^Q, \qquad (3.6)\\
\mathcal{M}_c &= -i\frac{f^2 g}{\sqrt{2}}\frac{1}{q_2^2}\frac{1}{t_2 - m_\eta^2} \\
&\quad \times (\bar{v}(k_2)P_L \not{q}_2 \gamma^\mu v(p_2))(\bar{u}(p_1)P_R u(k_1))\epsilon_\mu^Q, \qquad (3.7)\\
\mathcal{M}_d &= -i\frac{f^2 g}{\sqrt{2}}\frac{1}{q_2^2}\frac{1}{u_2 - m_\eta^2} \\
&\quad \times ((\bar{v}(k_1)P_L \not{q}_2 \gamma^\mu v(p_2))(\bar{u}(p_1)P_R u(k_2))\epsilon_\mu^Q, \qquad (3.8)\\
\mathcal{M}_e &= -i\frac{f^2 g}{\sqrt{2}}\frac{1}{t_3 - m_\eta^2}\frac{1}{t_3' - m_\eta^2} \\
&\quad \times ((\bar{v}(k_2)P_L v(p_2))(\bar{u}(p_1)P_R u(k_1)) \\
&\quad \times ((k_1 - p_1) + (k_1 - p_1 - Q))^\mu \epsilon_\mu^Q, \qquad (3.9)\\
\mathcal{M}_f &= -i\frac{f^2 g}{\sqrt{2}}\frac{1}{u_3 - m_\eta^2}\frac{1}{u_3' - m_\eta^2} \\
&\quad \times ((\bar{v}(k_1)P_L v(p_2))(\bar{u}(p_1)P_R u(k_2)) \\
&\quad \times ((k_2 - p_1) + (k_2 - p_1 - Q))^\mu \epsilon_\mu^Q, \qquad (3.10)
\end{aligned}$$

where we define the usual helicity projectors $P_{R/L} \equiv \frac{1}{2}(1 \pm \gamma_5)$, and the Mandelstam variables

$$\begin{aligned} t_1 &= (k_1 - q_1)^2, \\ t_2 &= (k_1 - p_1)^2, \\ u_1 &= (k_2 - q_1)^2, \\ u_2 &= (k_2 - p_1)^2, \\ t_3 &= (k_1 - p_1)^2 = t_2, \\ t_3' &= (k_2 - p_2)^2 = (k_1 - p_1 - Q)^2, \\ u_3 &= (k_2 - p_1)^2 = u_2, \\ u_3' &= (k_1 - p_2)^2 = (k_2 - p_1 - Q)^2. \end{aligned} \tag{3.11}$$

The vertex factors used in the matrix elements are as follows: the $l\nu W$ vertex has an $\frac{ig}{\sqrt{2}}\gamma^\mu P_L \epsilon_\mu^Q$, the $\chi\eta l$ vertex is $if P_L$, and the coupling between the W^- and the $\eta^+ - \eta^0$ is taken to be of the form $-ig(p + p')/\sqrt{2}$ from Ref. [169].

We have explicitly checked the gauge invariance of our set of Feynman diagrams. Writing the matrix element as

$$\mathcal{M} = \mathcal{M}^\mu \epsilon_\mu^Q, \tag{3.12}$$

the Ward identity

$$Q_\mu \mathcal{M}^\mu = 0, \tag{3.13}$$

is satisfied for the sum of the diagrams. The Ward identity takes the same form as for photon bremsstrahlung provided we take the lepton masses to be zero, since the axial vector current is conserved in this limit. Note that diagrams (a)+(c)+(e) form a gauge invariant subset, as do (b)+(d)+(f). The full amplitude is the sum of the partial amplitudes, properly weighted by a minus sign when two fermions are interchanged. Thus we have $\mathcal{M} = (\mathcal{M}_a + \mathcal{M}_c + \mathcal{M}_e) - (\mathcal{M}_b + \mathcal{M}_d + \mathcal{M}_f)$.

In performing the sum over spins and polarizations, we note the standard polarization sum,

$$\sum_{\text{pol.}} \epsilon_\mu^Q \epsilon_\nu^Q = -\left(g_{\mu\nu} - \frac{Q_\mu Q_\nu}{m_W^2}\right), \tag{3.14}$$

can be replaced with $-g_{\mu\nu}$ alone. The Ward identity of Eq. 3.13 ensures the second term in Eq. 3.14 does not contribute once the contributions from all diagrams are summed (and squared). The following traces contribute to $\sum_s |\mathcal{M}|^2$

$$\begin{aligned}
\sum_s \mathcal{M}_a \mathcal{M}_a^\dagger &= \alpha_{aa} \mathrm{Tr}[(\not{k}_2 - m_\chi) P_L \not{p}_2 P_R] \mathrm{Tr}[\not{p}_1 \gamma^\mu P_L \not{q}_1 (\not{k}_1 + m_\chi) \not{q}_1 P_R \gamma_\mu], \\
\sum_s \mathcal{M}_a \mathcal{M}_b^\dagger &= \alpha_{ab} \mathrm{Tr}[\not{p}_2 P_L (\not{k}_2 + m_\chi) \not{q}_1 P_R \gamma_\mu \not{p}_1 \gamma^\mu P_L \not{q}_1 (\not{k}_1 + m_\chi) P_R], \\
\sum_s \mathcal{M}_a \mathcal{M}_c^\dagger &= \alpha_{ac} \mathrm{Tr}[(\not{k}_2 - m_\chi) P_L \not{p}_2 \gamma^\mu \not{q}_2 P_R] \mathrm{Tr}[(\not{k}_1 + m_\chi) P_L \not{p}_1 \gamma_\mu P_L \not{q}_1], \\
\sum_s \mathcal{M}_a \mathcal{M}_d^\dagger &= \alpha_{ad} \mathrm{Tr}[\not{p}_2 P_L (\not{k}_2 + m_\chi) P_L \not{p}_1 \gamma^\mu P_L \not{q}_1 (\not{k}_1 + m_\chi) P_R \not{q}_2 \gamma_\mu], \\
\sum_s \mathcal{M}_a \mathcal{M}_e^\dagger &= \alpha_{ae} \mathrm{Tr}[(\not{k}_2 - m_\chi) P_L \not{p}_2 P_R] \mathrm{Tr}[(\not{k}_1 + m_\chi) P_L \not{p}_1 (2\not{k}_1 - 2\not{p}_1 - \not{Q}) P_L \not{q}_1], \\
\sum_s \mathcal{M}_a \mathcal{M}_f^\dagger &= \alpha_{af} \mathrm{Tr}[(\not{k}_1 + m_\chi) P_R \not{p}_2 P_L (\not{k}_2 + m_\chi) P_L \not{p}_1 (2\not{k}_2 - 2\not{p}_1 - \not{Q}) P_L \not{q}_1], \\
\sum_s \mathcal{M}_c \mathcal{M}_c^\dagger &= \alpha_{cc} \mathrm{Tr}[\not{p}_1 P_R (\not{k}_1 + m_\chi) P_L] \mathrm{Tr}[(\not{k}_2 - m_\chi) P_L \not{q}_2 \gamma^\mu \not{p}_2 \gamma_\mu \not{q}_2 P_R], \\
\sum_s \mathcal{M}_c \mathcal{M}_d^\dagger &= \alpha_{cd} \mathrm{Tr}[(\not{k}_2 - m_\chi) P_L \not{q}_2 \gamma^\mu (\not{p}_2 - m_l) \gamma_\mu \not{q}_2 P_R (\not{k}_1 - m_\chi) P_R \not{p}_1 P_L], \\
\sum_s \mathcal{M}_c \mathcal{M}_e^\dagger &= \alpha_{ce} \mathrm{Tr}[(\not{k}_1 + m_\chi) P_L \not{p}_1 P_R] \mathrm{Tr}[(\not{k}_2 - m_\chi) P_L \not{q}_2 (2\not{k}_1 - 2\not{p}_1 - \not{Q}) \not{p}_2 P_R], \\
\sum_s \mathcal{M}_c \mathcal{M}_f^\dagger &= \alpha_{cf} \mathrm{Tr}[(\not{k}_2 - m_\chi) P_L \not{q}_2 (2\not{k}_2 - 2\not{p}_1 - \not{Q}) \not{p}_2 P_R (\not{k}_1 - m_\chi) P_R \not{p}_1 P_L], \\
\sum_s \mathcal{M}_e \mathcal{M}_e^\dagger &= \alpha_{ee} \mathrm{Tr}[(\not{k}_2 - m_\chi) P_L \not{p}_2 P_R] \mathrm{Tr}[(\not{k}_1 + m_\chi) P_L \not{p}_1 P_R], \\
\sum_s \mathcal{M}_e \mathcal{M}_f^\dagger &= \alpha_{ef} \mathrm{Tr}[(\not{k}_2 - m_\chi) P_L \not{p}_2 P_R (\not{k}_1 - m_\chi) P_R \not{p}_1 P_L],
\end{aligned} \tag{3.15}$$

in which

$$
\begin{aligned}
\alpha_{aa} &\equiv -\frac{g^2 f^4}{2}\frac{1}{q_1^4}\frac{1}{(t_1-M_\eta^2)^2}, \\
\alpha_{ab} &\equiv -\frac{g^2 f^4}{2}\frac{1}{q_1^4}\frac{1}{(t_1-M_\eta^2)}\frac{1}{(u_1-M_\eta^2)}, \\
\alpha_{ac} &\equiv \frac{g^2 f^4}{2}\frac{1}{q_1^2 q_2^2}\frac{1}{(t_1-M_\eta^2)}\frac{1}{(t_2-M_\eta^2)}, \\
\alpha_{ad} &\equiv \frac{g^2 f^4}{2}\frac{1}{q_1^2 q_2^2}\frac{1}{(t_1-M_\eta^2)}\frac{1}{(u_2-M_\eta^2)}, \\
\alpha_{ae} &\equiv -\frac{g^2 f^4}{2}\frac{1}{q_1^2}\frac{1}{(t_1-M_\eta^2)}\frac{1}{(t_3-M_\eta^2)}\frac{1}{(t_3'-M_\eta^2)}, \\
\alpha_{af} &\equiv -\frac{g^2 f^4}{2}\frac{1}{q_1^2}\frac{1}{(t_1-M_\eta^2)}\frac{1}{(u_3-M_\eta^2)}\frac{1}{(u_3'-M_\eta^2)}, \\
\alpha_{cc} &\equiv -\frac{g^2 f^4}{2}\frac{1}{q_2^4}\frac{1}{(t_2-M_\eta^2)^2}, \\
\alpha_{cd} &\equiv -\frac{g^2 f^4}{2}\frac{1}{q_2^4}\frac{1}{(t_2-M_\eta)}\frac{1}{(u_2-M_\eta^2)}, \\
\alpha_{ce} &\equiv \frac{g^2 f^4}{2}\frac{1}{q_2^2}\frac{1}{(t_2-M_\eta^2)}\frac{1}{(t_3-M_\eta^2)}\frac{1}{(t_3'-M_\eta^2)}, \\
\alpha_{cf} &\equiv \frac{g^2 f^4}{2}\frac{1}{q_2^2}\frac{1}{(t_2-M_\eta^2)}\frac{1}{(u_3-M_\eta^2)}\frac{1}{(u_3'-M_\eta^2)}, \\
\alpha_{ee} &\equiv -\frac{g^2 f^4}{2}\frac{(2k_1-2p_1-Q)^2}{(t_3-M_\eta^2)^2(t_3'-M_\eta^2)^2}, \\
\alpha_{ef} &\equiv -\frac{g^2 f^4}{2}\frac{(2k_1-2p_1-Q)\cdot(2k_2-2p_1-Q)}{(t_3-M_\eta^2)(t_3'-M_\eta^2)(u_3-M_\eta^2)(u_3'-M_\eta^2)}.
\end{aligned}
\tag{3.16}
$$

The remaining cross terms $\mathcal{M}_b\mathcal{M}_b$, $\mathcal{M}_b\mathcal{M}_c$, $\mathcal{M}_b\mathcal{M}_d$, $\mathcal{M}_b\mathcal{M}_e$, $\mathcal{M}_b\mathcal{M}_f$, $\mathcal{M}_d\mathcal{M}_d$, $\mathcal{M}_d\mathcal{M}_e$, $\mathcal{M}_d\mathcal{M}_f$, and $\mathcal{M}_f\mathcal{M}_f$ are obtained by interchanging k_1 and k_2 for all terms in Eqs. 3.15 and 3.16.

3.2.2 Three Body Kinematics

Following Ref. [160], the cross section for the process' in Fig. 3.1 is given by

$$v\, d\sigma = \frac{1}{2s}\int \frac{1}{4}\sum_{\text{spin, pol.}} |\mathcal{M}|^2\, dLips^3, \tag{3.17}$$

in which $v = \sqrt{1-\frac{4m_\chi^2}{s}}$ is the mean DM velocity, and $dLips^3$ represents the Lorentz invariant 3-body phase space, given by

$$dLips^3 = (2\pi)^4 \frac{d^3\vec{p}_1}{2E_1}\frac{d^3\vec{p}_2}{2E_2}\frac{d^3\vec{Q}}{2E_W}\frac{\delta^4(P-p_1-p_2-Q)}{(2\pi)^9}. \tag{3.18}$$

where $P = k_1 + k_2$. The factor of 1/4 in Eq. 3.17 arises from the average over initial state spins. Eq. 3.18 can be expressed as the convolution of two Lorentz invariant phase space integrals, integrated over the square of fermion propagator 4-momentum q_1^2 ($q_1 = p_1 + Q$). That is, if we define

$$dLips^2(P^2, q_1^2, p_2^2) \equiv \frac{d^3\vec{q}_1}{2E_{q_1}}\frac{d^3\vec{p}_2}{2E_2}\frac{\delta^4(P-q_1-p_2)}{(2\pi)^2}, \tag{3.19}$$

then

$$dLips^3 \;=\; \int_{m_W^2}^{s}\frac{dq_1^2}{2\pi} dLips^2(P^2, q_1^2, p_2^2) dLips^2(q_1^2, Q^2, p_1^2). \tag{3.20}$$

Each 2-body phase space integral can now be evaluated in its respective CoM frame, that is $\vec{P} = 0$ for $dLips^2(P^2, q_1^2, p_2^2)$, and $\vec{q_1} = 0$ for $dLips^2(q_1^2, Q^2, p_1^2)$. These will be referred to as the P and q frames respectively. It can be easily shown that

$$dLips^2(P^2, q_1^2, p_2^2) = \frac{2|\vec{p}_2|}{E_P}\frac{1}{8\pi}\left(\frac{d\overline{\Omega}_P}{4\pi}\right), \tag{3.21}$$

where $\overline{\Omega}_P$ is the solid angle in the P frame. In this frame $|\vec{p}_2|^2 = E_2^2 - p_2^2 = E_{q_1}^2 - q_1^2$, and conservation of energy requires $\sqrt{P^2} = E_P = E_2 + E_{q_1}$, thus

$$E_2 = \frac{P^2 + p_2^2 - q_1^2}{2\sqrt{P^2}}. \tag{3.22}$$

Combining Eqs. 3.21 and 3.22

$$\begin{aligned} dLips^2(P^2, q_1^2, p_2^2) &= \frac{2|\vec{p}_2|}{E_P}\frac{1}{8\pi}\left(\frac{d\overline{\Omega}_P}{4\pi}\right) = \frac{2\sqrt{E_2^2 - p_2^2}}{E_P}\frac{1}{8\pi}\left(\frac{d\overline{\Omega}_P}{4\pi}\right) \\ &= \frac{\sqrt{\left(P^2 + p_2^2 - q_1^2\right)^2 - 4P^2p_2^2}}{P^2}\frac{1}{8\pi}\left(\frac{d\overline{\Omega}_P}{4\pi}\right) \\ &= \frac{\sqrt{\lambda(P^2, q_1^2, p_2^2)}}{P^2}\frac{1}{8\pi}\left(\frac{d\overline{\Omega}_P}{4\pi}\right), \end{aligned} \tag{3.23}$$

where $\lambda(x, y, z)$ is the triangle function, defined by

$$\lambda(x, y, z) = x^2 + y^2 + z^2 - 2xy - 2xz - 2yz. \tag{3.24}$$

Therefore, by applying the same procedure to $dLips^2(q_1^2, Q^2, p_1^2)$, noting that $Q^2 = m_W^2$, P^2 is just the invariant quantity s, and taking the limit $p_1^2/p_2^2 \to 0$, Eq. 3.20 becomes

$$\begin{aligned} dLips^3 &= \frac{1}{2^6(2\pi)^5}\int^{\overline{\Omega}_q}\int^{\overline{\Omega}_P}\int_{m_W^2}^{s} dq_1^2 d\overline{\Omega}_P d\overline{\Omega}_q \frac{\sqrt{\lambda(s, q_1^2, 0)\lambda(q_1^2, m_W^2, 0)}}{sq_1^2} \\ &= \frac{1}{2^6(2\pi)^4}\int_{m_W^2}^{s} dq_1^2 \frac{(s - q_1^2)(q_1^2 - m_W^2)}{sq_1^2} d\phi\, d\cos\theta_P\, d\cos\theta_q, \end{aligned} \tag{3.25}$$

where θ_P and θ_q are defined in the P and q frames respectively, and ϕ is the angle of intersection between the plane defined by $\chi\chi \to e^+(e^-)^*$ with that defined by $e^+\nu W^-$.

We wish to evaluate the cross section in the CoM frame of the DM particles (P frame). In order to do so we require all 4-momenta to be evaluated in this frame, and expressed as a function of invariant quantities s and m_W, dark matter velocity v, and integration variables q_1^2, θ_P, θ_q, and ϕ. The 4-momenta of the initial state $\chi\chi$ in the P frame are given by

$$\begin{aligned} k_1^\mu &\overset{P}{=} \frac{\sqrt{s}}{2}\left\{1, v(\sin\theta_P\cos\phi, \sin\theta\sin\phi, \cos\theta_P)\right\}, \\ k_2^\mu &\overset{P}{=} \frac{\sqrt{s}}{2}\left\{1, -v(\sin\theta_P\cos\phi, \sin\theta\sin\phi, \cos\theta_P)\right\}, \end{aligned} \tag{3.26}$$

where v is the magnitude of the DM velocity. Given that $p_2^2 \simeq 0$, and using Eq. 3.22, the final state momenta are given by

$$\begin{aligned} q_1^\mu &\overset{P}{=} \frac{1}{2\sqrt{s}}\left\{(s+q_1^2), 0, 0, (s-q_1^2)\right\}, \\ p_2^\mu &\overset{P}{=} \frac{1}{2\sqrt{s}}\left\{(s-q_1^2), 0, 0, -(s-q_1^2)\right\}. \end{aligned} \tag{3.27}$$

To obtain the 4-momenta p_1 and Q, we evaluate them in the q frame, then boost into the P frame. In the q frame

$$q_1^\mu \overset{q}{=} \left\{\sqrt{q_1^2}, 0, 0, 0\right\}, \tag{3.28}$$

and

$$\begin{aligned} p_1^\mu &\overset{q}{=} \frac{q_1^2 - m_W^2}{2\sqrt{s}}\left\{1, \sin\theta_q, 0, \cos\theta_q\right\}, \\ Q^\mu &\overset{q}{=} \frac{q_1^2 - m_W^2}{2\sqrt{s}}\left\{(q_1^2 + m_W^2)/(q_1^2 - m_W^2), -\sin\theta_q, 0, -\cos\theta_q\right\}. \end{aligned} \tag{3.29}$$

Boosting Eq. 3.28 from the q frame into the P frame we obtain the boost factors

$$\gamma = \frac{s + q_1^2}{2\sqrt{s}\sqrt{q_1^2}}, \quad \text{and} \quad \gamma\beta = \frac{s - q_1^2}{2\sqrt{s}\sqrt{q_1^2}}. \tag{3.30}$$

Applying the same boost to 4-momenta in Eq. 3.29 we find

$$p_1^\mu \overset{P}{=} \frac{q_1^2 - m_W^2}{2\sqrt{s}}\{[\gamma + \gamma\beta\cos\theta_q]\,,\, \sin\theta_q\,,\, 0\,,\, [\gamma\beta + \gamma\cos\theta_q]\}, \tag{3.31}$$

$$Q^\mu \overset{P}{=} \frac{q_1^2 - m_W^2}{2\sqrt{s}}\left\{\left[\gamma\frac{q_1^2 + m_W^2}{q_1^2 - m_W^2} - \gamma\beta\cos\theta_q\right], -\sin\theta_q\,,\, 0\,,\, \left[\gamma\beta\frac{q_1^2 + m_W^2}{q_1^2 - m_W^2} - \gamma\cos\theta_q\right]\right\}.$$

The 4-momenta in Eqs. 3.26, 3.27, and 3.31 can now be substituted into the traces in Eq. 3.15, to evaluate $|\mathcal{M}|^2$. Before doing so, a few things must be said about the contribution from longitudinal polarization states.

3.2.3 Longitudinal Polarization States

Electroweak gauge bosons differ from photons in that they have a mass. An important consequence of this fact is the possession of longitudinal polarization

states, and the possibility of zero spin projections. As pointed out in Section 3.2.1, despite the presence of a longitudinal polarization, the Ward identity ensures that the spin summation rule for W^- gauge bosons is identical to that of photons. With this in mind, in this section we explicitly check the contribution to the cross section from longitudinally polarized Ws.

A massive vector boson in its rest frame has a polarization vector ϵ, that can be decomposed into a linear combination of 3 orthogonal basis vectors

$$\epsilon_1^\mu \equiv \{0,1,0,0\}, \quad \epsilon_2^\mu \equiv \{0,0,1,0\}, \quad \epsilon_3^\mu \equiv \{0,0,0,1\}. \tag{3.32}$$

The polarization ϵ must satisfy the properties

$$\epsilon \cdot Q = 0, \qquad \epsilon^2 = -1, \tag{3.33}$$

where Q^μ is the 4-momentum of the vector boson in any given frame. Boosting from the rest frame into the frame in which the W has momentum Q^μ, we obtain boost parameters

$$\gamma = \frac{Q^0}{m_W}, \quad \beta_x = -\frac{Q^1}{Q^0}, \quad \beta_y = -\frac{Q^2}{Q^0}, \quad \beta_z = -\frac{Q^3}{Q^0}. \tag{3.34}$$

In this new frame the polarization basis vectors in Eq.3.32 become

$$\begin{aligned}
\epsilon_1^\mu &= \left\{-\gamma\beta_x,\, 1+(\gamma-1)\frac{\beta_x^2}{\beta^2},\, (\gamma-1)\frac{\beta_x\beta_y}{\beta^2},\, (\gamma-1)\frac{\beta_x\beta_z}{\beta^2}\right\},\\
\epsilon_2^\mu &= \left\{-\gamma\beta_y,\, (\gamma-1)\frac{\beta_y\beta_x}{\beta^2},\, 1+(\gamma-1)\frac{\beta_y^2}{\beta^2},\, (\gamma-1)\frac{\beta_y\beta_z}{\beta^2}\right\},\\
\epsilon_3^\mu &= \left\{-\gamma\beta_z,\, (\gamma-1)\frac{\beta_z\beta_x}{\beta^2},\, (\gamma-1)\frac{\beta_z\beta_y}{\beta^2},\, 1+(\gamma-1)\frac{\beta_z^2}{\beta^2}\right\},
\end{aligned} \tag{3.35}$$

and satisfy the same properties as the prior set, including orthogonality.

The longitudinal polarization state, by definition, has a 3-vector component that is parallel to the 3-vector $\vec{Q}$. We obtain the longitudinal polarization vector by rotating the vectors in Eq. 3.35 into a new basis, in which one of the three

basis vectors satisfies this criterion. We perform an Euler rotation on the basis set, using the x-convention for rotation defined by

$$\begin{pmatrix} \epsilon^{\mu}_{T1} \\ \epsilon^{\mu}_{T2} \\ \epsilon^{\mu}_{L} \end{pmatrix} = \begin{pmatrix} \cos\psi & \sin\psi & 0 \\ -\sin\psi & \cos\psi & 0 \\ 0 & 0 & 1 \end{pmatrix} \begin{pmatrix} 1 & 0 & 0 \\ 0 & \cos\theta & \sin\theta \\ 0 & -\sin\theta & \cos\theta \end{pmatrix} \times \begin{pmatrix} \cos\phi & \sin\phi & 0 \\ -\sin\phi & \cos\phi & 0 \\ 0 & 0 & 1 \end{pmatrix} \begin{pmatrix} \epsilon^{\mu}_{1} \\ \epsilon^{\mu}_{2} \\ \epsilon^{\mu}_{3} \end{pmatrix}, \tag{3.36}$$

We then use the conditions $\vec{\epsilon_{T1}} \cdot \vec{Q} = 0$ and $\vec{\epsilon_{T2}} \cdot \vec{Q} = 0$ to determine Euler angles θ and ϕ. The solutions are

$$\theta = \pm\cos^{-1}\left(\pm \frac{\vec{\epsilon_3} \cdot \vec{Q}}{\sqrt{(\vec{\epsilon_1} \cdot \vec{Q})^2 + (\vec{\epsilon_2} \cdot \vec{Q})^2 + (\vec{\epsilon_3} \cdot \vec{Q})^2}} \right). \tag{3.37}$$

and

$$\phi = \pm\cos^{-1}\left(\pm \frac{\vec{\epsilon_2} \cdot \vec{Q}}{\sqrt{(\vec{\epsilon_1} \cdot \vec{Q})^2 + (\vec{\epsilon_2} \cdot \vec{Q})^2}} \right). \tag{3.38}$$

These angles, as well as the 4-vector ϵ^{μ}_{L}, are independent of the third Euler angle ψ, which represents rotations in the transverse plane. We can now calculate the longitudinal polarization vector in any reference frame.

As discussed in the previous section, the cross section 3.17 is being evaluated in the P, or CoM frame. Therefore, to evaluate the contribution from ϵ_L, we must boost Eq. 3.32 from the rest frame of the W to the P frame. The W momentum, Q (Eq. 3.31), has non-zero components in all but the y-direction in momentum space. From the rest frame, we therefore need to boost in both the x and z directions, that is, $\beta_y = 0$, $\beta_z \neq 0$ and $\beta_x \neq 0$. In this frame the polarization basis

vectors are

$$\begin{aligned}\epsilon_1^\mu &= \left\{-\gamma\beta_x,\, 1+(\gamma-1)\frac{\beta_x^2}{\beta^2}, 0,\, (\gamma-1)\frac{\beta_x\beta_z}{\beta^2}\right\},\\ \epsilon_2^\mu &= \{0,\, 0, 1, 0\}\,,\\ \epsilon_3^\mu &= \left\{-\gamma\beta_z,\, (\gamma-1)\frac{\beta_z\beta_x}{\beta^2}, 0,\, 1+(\gamma-1)\frac{\beta_z^2}{\beta^2}\right\}. \end{aligned} \tag{3.39}$$

Thus using Eq. 3.34, $\vec{\epsilon_1}\cdot\vec{Q} = -\gamma^2\beta_x m_W$ and $\vec{\epsilon_3}\cdot\vec{Q} = -\gamma^2\beta_z m_W$. In this frame Eq. 3.37 becomes

$$\theta \,=\, \cos^{-1}\left(\frac{-\beta_z}{\beta}\right) \,=\, \sin^{-1}\left(\frac{-\beta_x}{\beta}\right), \tag{3.40}$$

and Eq. 3.38 is simply $\phi = \pi/2$. The longitudinal polarization vector is therefore given by

$$\begin{aligned}\epsilon_L^\mu &= -\frac{\beta_x}{\beta}\epsilon_1^\mu - \frac{\beta_z}{\beta}\epsilon_3^\mu\\ &= \frac{1}{\beta}\left(\gamma\beta^2,\, -\gamma\beta_x, 0, -\gamma\beta_z\right)\\ &= \frac{Q^0}{m_W|\vec{Q}|}\left\{\frac{|\vec{Q}|^2}{Q^0},\, \vec{Q}\right\}. \end{aligned} \tag{3.41}$$

As $\gamma \to \infty$ Eq. 3.41 approaches Q^μ/m_W, satisfying the Goldstone equivalence principle, relating the longitudinal polarization of the W to a massless Goldstone mode of the Higgs boson [170–172].

Using Eqs. 3.5-3.10 and Eq. 3.41, we evaluate the longitudinal contribution to the s-wave amplitude, finding that

$$\mathcal{M}^\mu \epsilon_{L\,\mu} = 0, \tag{3.42}$$

that is, the spin zero projection of the W does not contribute to the purely s-wave cross section for the processes pictured in Fig. 3.1. The W, therefore, behaves exactly as a massive transverse photon in this context, as hinted by the Ward identity in Eq. 3.13. This implies that a good test of our calculation should be that it reproduces that for photon bremsstrahlung in the limit $m_W \to 0$.

3.2.4 The W-strahlung Cross Section

Evaluating the traces in Eq. 3.15, using 4-momenta in Eqns. 3.26, 3.27 and 3.31, and expanding around $v = 0$, to leading order the amplitude squared is given by

$$\begin{aligned}\sum_s |\mathcal{M}|^2 = \quad & (\cos\theta_q + 1)(q_1^2 - m_W^2)(q_1^2 - 4m_\chi^2) \times \Big[8q_1^2 m_\chi^2 \big(q_1^4(\cos^2\theta_q - 1) \\ & + 2q_1^2(\cos\theta_q - \cos^2\theta_q + 2)m_W^2 + (\cos^2\theta_q - 1)m_W^4\big) \\ & - q_1^4\big(q_1^4((\cos\theta_q - 2)\cos\theta_q + 5) - 2q_1^2(\cos\theta_q - 1)^2 m_W^2 + (\cos\theta_q - 1)^2 m_W^4\big) \\ & - 16m_\chi^4\big(q_1^2 - q_1^2\cos\theta_q + (\cos\theta_q + 1)m_W^2\big)^2\Big] \Big/ \\ & \Big(\big(q_1^2 - 2(m_\eta^2 + m_\chi^2)\big)^2\big(4m_\chi^2((\cos\theta_q + 1)m_W^2 - q_1^2\cos\theta_q) \\ & + q_1^2(\cos\theta_q - 1)(q_1^2 - m_W^2) - 4q_1^2 m_\eta^2\big)^2\Big). \end{aligned} \tag{3.43}$$

Substituting this into Eq. 3.17, and performing integrations over q_1^2, $\cos\theta_q$, $\cos\theta_P$ and ϕ, results in the following cross section

$$\begin{aligned}\sigma v \simeq \quad & \frac{\alpha_W f^4}{256\pi^2 m_\chi^2}\Bigg\{(\mu+1)\left[\frac{\pi^2}{6} - \ln^2\left(\frac{2m_\chi^2(\mu+1)}{4m_\chi^2\mu - m_W^2}\right) - 2\mathrm{Li}_2\left(\frac{2m_\chi^2(\mu+1) - m_W^2}{4m_\chi^2\mu - m_W^2}\right)\right. \\ & + 2\mathrm{Li}_2\left(\frac{m_W^2}{2m_\chi^2(\mu+1)}\right) - \mathrm{Li}_2\left(\frac{m_W^2}{m_\chi^2(\mu+1)^2}\right) - 2\mathrm{Li}_2\left(\frac{m_W^2(\mu-1)}{2(m_\chi^2(\mu+1)^2 - m_W^2)}\right) \\ & + 2\ln\left(\frac{4m_\chi^2\mu - m_W^2}{2m_\chi^2(\mu-1)}\right)\ln\left(1 - \frac{m_W^2}{2m_\chi^2(\mu+1)}\right) \\ & \left. + \ln\left(\frac{m_W^2(\mu-1)^2}{4(m_\chi^2(\mu+1)^2 - m_W^2)}\right)\ln\left(1 - \frac{m_W^2}{m_\chi^2(\mu+1)^2}\right)\right] \\ & + \frac{(4\mu+3)}{(\mu+1)} - \frac{m_W^2\left(4m_\chi^2(\mu+1)(4\mu+3) - (m_W^2 - 4m_\chi^2)(\mu-3)\right)}{16m_\chi^4(\mu+1)^2} \\ & + \frac{m_W^2\left(4m_\chi^4(\mu+1)^4 - 2m_W^2 m_\chi^2(\mu+1)(\mu+3) - m_W^4(\mu-1)\right)}{4m_\chi^4(\mu+1)^3\left(m_\chi^2(\mu+1)^2 - m_W^2\right)}\ln\left(\frac{m_W^2}{4m_\chi^2}\right) \\ & + \ln\left(\frac{2m_\chi^2(\mu-1)}{2m_\chi^2(\mu+1) - m_W^2}\right)\frac{(\mu-1)\left(2m_\chi^2(\mu+1) - m_W^2\right)}{4m_\chi^4(\mu+1)^3(4m_\chi^2\mu - m_W^2)\left(m_\chi^2(\mu+1)^2 - m_W^2\right)} \\ & \times\left(4m_\chi^6(\mu+1)^4(4\mu+1) - m_\chi^4 m_W^2(\mu+1)^2\left(3\mu(\mu+6)+7\right)\right. \\ & \left.\left. + 2m_\chi^2 m_W^4\left(\mu(\mu+4)+1\right) - m_W^6\right)\right\}, \end{aligned} \tag{3.44}$$

where $\alpha_W \equiv g^2/(4\pi)$. The Spence function (or "dilogarithm") is defined as $\mathrm{Li}_2(z) \equiv -\int_0^z \frac{d\zeta}{\zeta} \ln|1-\zeta| = \sum_{k=1}^{\infty} \frac{z^k}{k^2}$.

If we take the limit $m_W \to 0$ and replace α_W with $2\alpha_{\mathsf{em}}$, then Eq. 3.44 reproduces the cross section for bremsstrahlung of photons, namely[2]

$$\sigma v \simeq \frac{\alpha_{\mathsf{em}} f^4}{128\pi^2 m_\chi^2} \quad \left\{ (\mu+1)\left[\frac{\pi^2}{6} - \ln^2\left(\frac{\mu+1}{2\mu}\right) - 2\mathrm{Li}_2\left(\frac{\mu+1}{2\mu}\right)\right] + \frac{4\mu+3}{\mu+1} + \frac{4\mu^2-3\mu-1}{2\mu}\ln\left(\frac{\mu-1}{\mu+1}\right)\right\}. \qquad (3.45)$$

The successful recovery of the photon bremsstrahlung result in the massless W limit provides a check[3] on the rather complicated expression for massive W bremsstrahlung given above in Eq. 3.44.

Since we are working in the limits $v = 0$ and $m_f = 0$, the nonzero results in Eqs. 3.44 and 3.45 imply that the leading terms are neither helicity nor velocity suppressed. Not clear from the mathematical expressions is the sensible fact that the cross sections fall monotonically with increasing m_η (or μ). This monotonic fall is shown in Fig. 3.2, where we plot the ratio of the W-strahlung cross section to that of the lowest order process, $R = v\,\sigma(\chi\chi \to e^+\nu W^-)/v\,\sigma(\chi\chi \to e^+e^-)$. The lowest order process itself falls as μ^{-2}, so the W-strahlung process falls as μ^{-4}. This latter dependence is expected for processes with two propagators each off-shell by $1/\mu$, thereby signaling leading order cancellations among Fig. 3.1 diagrams (a)-(d).

Importantly, the effectiveness of the W-strahlung processes in lifting suppression of the annihilation rate is evident in Fig. 3.2. The ratio is maximized for μ close to 1, where m_χ and m_η are nearly degenerate. However, the W-strahlung

[2]Note that Eq.2. of Ref. [155] is larger by an overall factor of two, and also has the opposite sign for the $(1+\mu)[...]$ term, while Eq.1. of Ref. [155] is consistent with our results.

[3]A related work [173] appeared on the arXiv nearly simultaneously with ours. In this related work there appears analytic expressions for the $M_Z,\ M_W = 0$ limits of the cross-section which we calculate, thereby providing another calculational check.

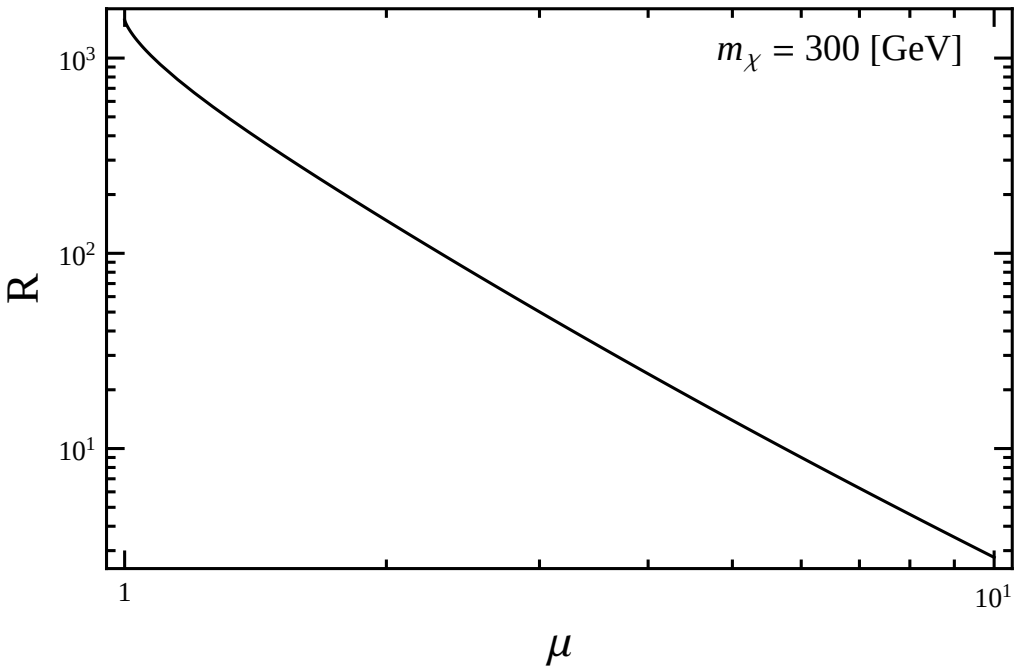

Figure 3.2: The ratio $R = v\,\sigma(\chi\chi \to e^+\nu W^-)/v\,\sigma(\chi\chi \to e^+e^-)$ as a function of $\mu = (m_\eta/m_\chi)^2$, for $m_\chi = 300$ GeV. We have used $v = 10^{-3}c$, appropriate for the Galactic halo.

process dominates over the tree level annihilation even if a mild hierarchy between m_χ and m_η is assumed. The ratio exceeds 100 for $\mu \lesssim 2$.

Fig. 3.3 illustrates that the ratio R is insensitive to the DM mass, except for low m_χ where the W mass significantly impacts phase space. From the figure one gleans that for $m_\chi \gtrsim 3\,m_W$, the ratio R is already near to its asymptotic value. Incidentally, the asymptotic value may be obtained analytically by dividing Eq. 3.45 with Eq. 3.4 and rescaling α_{em} with $\alpha_W/2$.

In Fig. 3.4 we compare the W-strahlung cross section with that for photon bremsstrahlung. For high dark matter masses where the W mass is negligible, the two cross sections are identical except for the overall normalization, which is higher by factor of $1/(2\sin^2\theta_W) = 2.17$ for W-strahlung. For lower DM mass, the

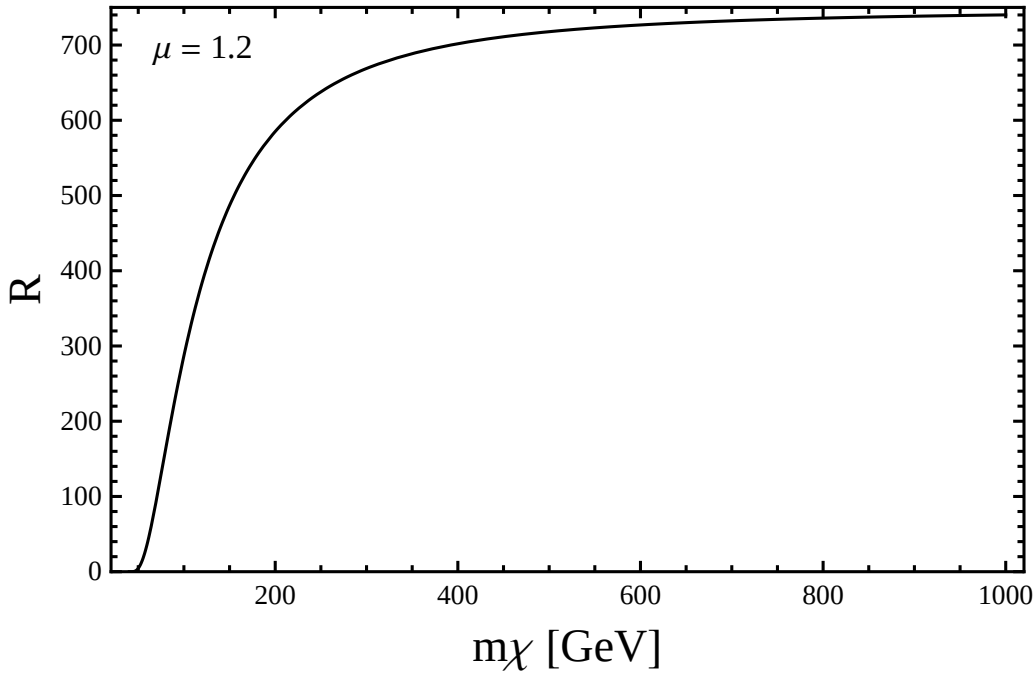

Figure 3.3: The ratio $R = v\,\sigma(\chi\chi \to e^+\nu W^-)/v\,\sigma(\chi\chi \to e^+e^-)$ as a function of the DM mass m_χ, for $\mu = 1.2$ GeV. We have used $v = 10^{-3}c$, appropriate for the Galactic halo.

available phase space is reduced due to W mass effects, thus the W-strahlung cross section falls below that for photons. This can be seen in Fig. 3.4 for $m_\chi \lesssim 150$ GeV (this number is fairly insensitive to μ). Another factor of two is gained for W-strahlung when the W^+ mode is added to the W^- mode shown here.

Nominally, the correct dark matter energy fraction is obtained for early-Universe thermal decoupling with an annihilation cross section of $3 \times 10^{-26}\mathrm{cm}^3/\mathrm{s}$. It is seen in Fig. 3.4 that the W-strahlung mode falls 2-3 orders of magnitude below this value. Note that at freeze-out DM was semi-relativistic, with $v^2 \sim 10^{-1}$, whereas today it is non-relativistic with $v^2 \sim 10^{-6}$, implying substantially less velocity suppression of the p-wave cross section in the early Universe than today. Thus the ratio in Fig. 3.2 was scaled down by 5 orders of magnitude. From this scaling

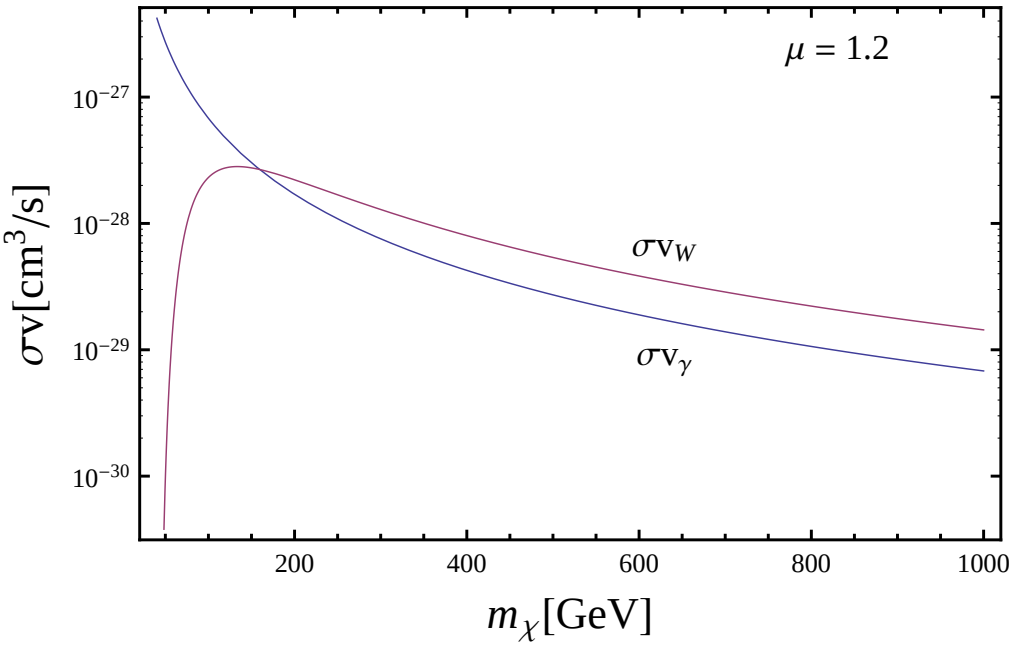

Figure 3.4: The cross sections for $\chi\chi \to e^+\nu W^-$ (red) and $\chi\chi \to e^+e^-\gamma$ (blue), for $\mu = 1.2$ and coupling $f = 1$. For large DM mass, the cross sections differ by a factor of $1/(2\sin^2\theta_W) = 2.17$ while for m_χ comparable to m_W the W bremsstrahlung cross section is suppressed by phase space effects.

it is clear that $\chi\chi \to e^-e^+$ could have been significant near freezeout, while the W-strahlung process was sub-dominant, at best achieving a contribution of order 1% as μ approaches 1. As μ approaches 1 coannihilations become important. In the coannihilation region, discussed in detail in Section 1.3.2, the cross section for the process $\chi\chi \to q\overline{q}$ only constitutes a small fraction of $\langle\sigma v\rangle_{eff}$, and hence the contribution from W-strahlung drops well below 1%. In fact in no region of parameter space do bremsstrahlung processes make as high as a 1% contribution to $\langle\sigma v\rangle_{eff}$. It can therefore be concluded that despite potentially being important for annihilations in the Galactic Center today, bremsstrahlung processes are almost irrelevant in determining the relic abundance.

3.2.5 W and Lepton Spectra

To obtain the energy spectrum of the W, we compute the differential cross section in terms of E_W by making the transformation

$$d\cos(\theta_q) \to \frac{-4\sqrt{s}q^2}{(s-q^2)(q^2-m_W^2)} dE_W. \tag{3.46}$$

The energy spectrum of the primary leptons is calculated in similar fashion.

The W spectrum per $\chi\chi \to e\nu W$ event is given in Fig. 3.5. We use the scaling variable $x_W \equiv E_W/m_\chi$, and plot $dN/dx_W \equiv (\frac{1}{\sigma_{e^+\nu W^-}})\frac{d\sigma_{e^+\nu W^-}}{dx_W}$, where we find $\frac{d\sigma_{e^+\nu W^-}}{dx_W}$ to be given by Eq. 3.47. The kinematic range of x_W is $[\frac{m_W}{m_\chi}, (1+\frac{m_W^2}{4m_\chi^2})]$, with the lower limit corresponding to a W produced at rest, and the upper limit corresponding to parallel lepton momenta balancing the opposite W momentum. As evident in Fig. 3.5, the W boson spectrum has a broad energy distribution, including a significant high energy component.

$$\begin{aligned} v\frac{d\sigma}{dx_W} = \quad & \frac{\alpha_W f^4}{128\pi^2 m_\chi^2}\left((1-x_W)+\frac{m_W^2}{4m_\chi^2}\right) \\ & \left\{\sqrt{x_W^2-\frac{m_W^2}{m_\chi^2}}\left[\frac{2}{\left((\mu+1)(\mu+1-2x_W)+\frac{m_W^2}{m_\chi^2}\right)}-\frac{1}{(\mu+1-x_W)^2}\right]\right. \\ & \left.-\frac{\left((\mu+1)(\mu+1-2x_W)+\frac{m_W^2}{m_\chi^2}\right)}{2(\mu+1-x_W)^3}\ln\left(\frac{\mu+1-x_W+\sqrt{x_W^2-m_W^2/m_\chi^2}}{\mu+1-x_W-\sqrt{x_W^2-m_W^2/m_\chi^2}}\right)\right\}. \end{aligned} \tag{3.47}$$

For the lepton energy spectrum, shown in Fig. 3.6, the range of the scaling variable $x_\ell \equiv E_\ell/m_\chi$ is $[0, 1-\frac{m_W^2}{4m_\chi^2}]$. The differential cross section $\frac{d\sigma}{dx_l}$ is given in Eq. 3.48. Both limits arise when one lepton has zero energy and the other is produced back-to-back with the W. Note that this spectrum is valid for either the e^+ or the ν from the annihilation $\chi\chi \to e^+\nu W^-$, and for either e^- or $\overline{\nu}$ from the annihilation $\chi\chi \to e^-\overline{\nu}W^+$.

$$
\begin{aligned}
v\frac{d\sigma}{dx_l} = \quad & \frac{\alpha_W f^4}{512\pi^2 m_\chi^2}\frac{1}{(\mu-1+2x_l)^2} \\
& \left\{\left(4(1-x_l)^2 - 4x_l(\mu+1) + 3(\mu+1)^2 - \frac{m_W^2}{m_\chi^2}(\mu+3)\right)\right. \\
& \times \ln\left(\frac{2m_\chi^2(\mu+1)(1-x_l) - m_W^2}{\left(2m_\chi^2(\mu+1-2x_l) - m_W^2\right)(1-x_l)}\right) \\
& - \frac{x_l\left(4m_\chi^2(1-x_l) - m_W^2\right)}{\left(2m_\chi^2(1-x_l)(\mu+1) - m_W^2\right)(1-x_l)^2} \\
& \times \left[(1-x_l)^2\left(4(1-x_l)^2 - x_l(\mu+1) + 3(\mu+1)^2\right)\right. \\
& \left.\left. + \frac{m_W^2}{4m_\chi^2}(1-x_l)\left(x_l(\mu+11) - 4(\mu+3)\right) - x_l\frac{m_W^2}{8m_\chi^2}\right]\right\}. \qquad (3.48)
\end{aligned}
$$

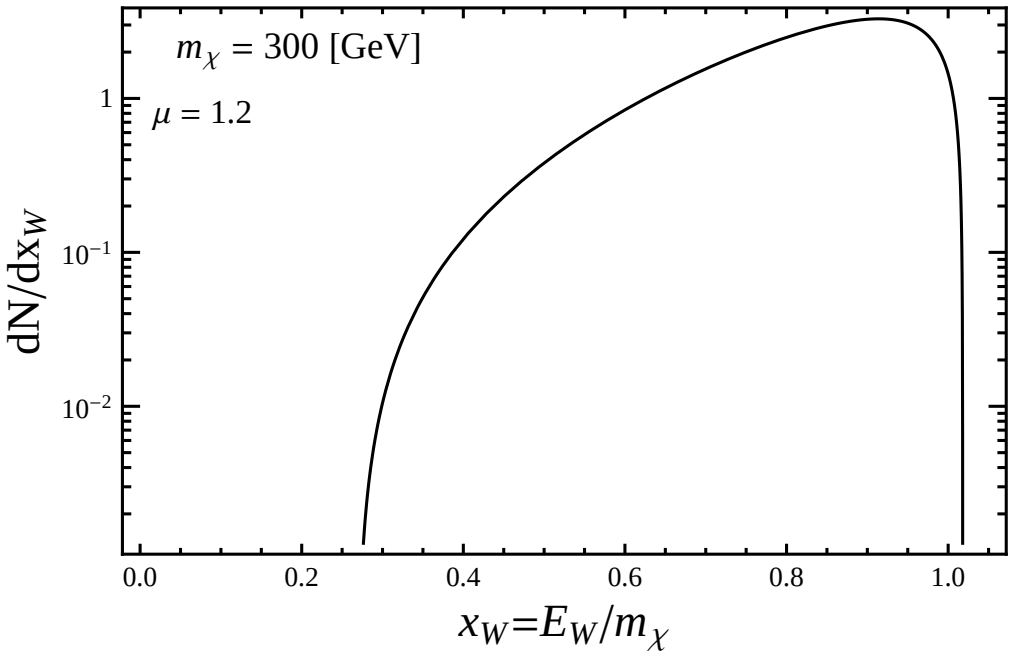

Figure 3.5: The W spectrum per $\chi\chi \to e\nu W$ annihilation for $m_\chi = 300$ GeV and $\mu = 1.2$.

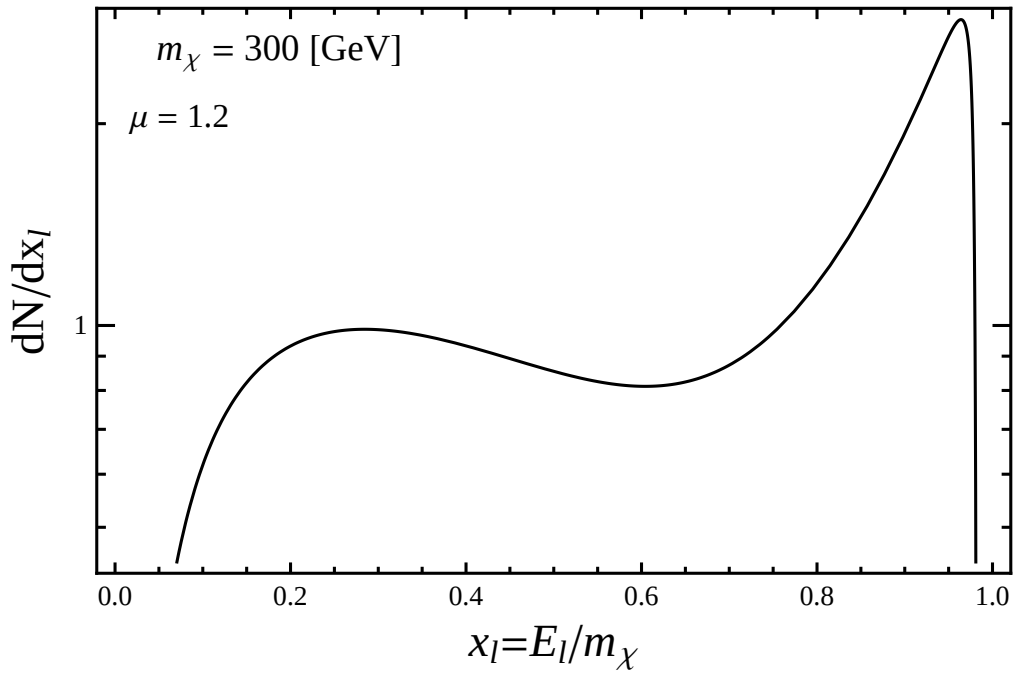

Figure 3.6: The primary lepton spectrum per $\chi\chi \to e\nu W$ annihilation, for $m_\chi = 300$ GeV and $\mu = 1.2$.

3.2.6 Z-strahlung

Consider the processes with a $\overline{\nu}\nu Z$ final state. The cross sections for the Z-strahlung processes are related to those for W-strahlung in a simple way: The amplitudes producing $\overline{\nu}\nu Z$ arise from the same six graphs of Fig.3.1, where e, W and η^+ are replaced everywhere by ν and Z and η_0, respectively. The calculation of the amplitudes, and their interferences, proceeds in an identical fashion. After making the replacement $m_W \to m_Z$, the cross section for the annihilation process $\chi\chi \to \nu\bar{\nu}Z$ differs from that for $\chi\chi \to e^+\nu W^-$ by only an overall normalization

factor,

$$\begin{aligned} v\,\sigma_{\nu\bar{\nu}Z} &= \frac{1}{(2\cos^2\theta_W)} \times v\,\sigma_{e^+\nu W^-}\Big|_{m_W\to m_Z} \\ &\simeq 0.65 \times v\,\sigma_{e^+\nu W^-}\Big|_{m_W\to m_Z}. \end{aligned} \tag{3.49}$$

Consider now the e^+e^-Z final state. Again, the amplitudes arise from the same six basic graphs of Fig.3.1. Since only the left-handed leptons couple to the dark matter via the SU(2) doublet η, only the left handed component of e^- participates in the interaction with the Z. Therefore, the couplings of the charged leptons to Z and W take the same form, up to a normalization constant. We thus find

$$\begin{aligned} v\,\sigma_{e^+e^-Z} &= \frac{2\left(\sin^2\theta_W - \frac{1}{2}\right)^2}{\cos^2\theta_W} \times v\,\sigma_{e^+\nu W^-}\Big|_{m_W\to m_Z} \\ &\simeq 0.19 \times v\,\sigma_{e^+\nu W^-}\Big|_{m_W\to m_Z}. \end{aligned} \tag{3.50}$$

Adding the four contributions to W/Zstrahlung, we find

$$v\,\sigma_{W/Z-\text{strahlung}} = 2.84 \times v\,\sigma_{e^+\nu W^-}\,. \tag{3.51}$$

3.2.7 The Total Bremsstrahlung Cross-Section

There are clear advantages and disadvantages of seeking photon- versus W/Z-bremsstrahlung as an indirect signature of dark matter. With photon bremsstrahlung, the photon itself is easily detected. It's energy spectrum may then be readily compared to model predictions. With W-strahlung, it is the decay products of the W decay which must be sought. Their spectra are less attributable to the model of dark matter annihilation. However, the total rate for W/Z-strahlung exceeds that of photon-strahlung. Photons couple with strength e, W's couple with strength $g/\sqrt{2} = e/(\sqrt{2}\sin\theta_W)$, and Z's couple to neutrinos with strength $g/(2\cos\theta_W) = e/(2\cos\theta_W\sin\theta_W)$. Therefore in the high energy limit where the

W and Z masses can be neglected, we expect

$$\sigma_{e^+\nu W^-} = \frac{1}{2\sin^2\theta_W}\sigma_{e^+e^-\gamma} = 2.17\sigma_{e^+e^-\gamma}. \quad (3.52)$$

So, in the high energy limit where $m_\chi \gtrsim 300\,\mathrm{GeV} \gg m_W$, the total cross section becomes

$$\begin{aligned}\sigma_{\text{brem, total}} &= \sigma_{e^+\nu W^-} + \sigma_{\bar{\nu}e^- W^+} \\ &\quad + \sigma_{\bar{\nu}\nu Z} + \sigma_{e^+e^- Z} + \sigma_{e^+e^-\gamma} \\ &= 7.16\,\sigma_{e^+e^-\gamma}. \end{aligned} \quad (3.53)$$

Furthermore, the varied decay products of the W/Z allow more multi-messenger experiments to engage in the dark matter search. Charged leptons, protons and antiprotons, neutrinos, and even deuterons are expected, at calculable rates and with predictable spectra. Importantly, hadronic decay products are unavoidable, despite a purely leptonic tree-level annihilation. The tens of millions of Z events produced at CERN's e^+e^- collider show in detail what the branching fractions and spectra are for each kind of decay product. In Ref. [168] the authors explore the favorable prospects for using W-strahlung decay products as indirect signatures for dark matter.

3.3 Conclusions

Certain classes of models for Majorana dark matter contain helicity suppression of the s-wave annihilation cross section. This results in the velocity suppressed p-wave processes being the dominant mode for dark matter annihilation today. The most notable example of this type of model are SUSY models which contain bino-like dark matter.

It has long been known that the bremsstrahlung of a photon can lift helicity suppression in these models [151–156]. In this work, as in Refs. [160–168], we

considered the possibility of electroweak bremsstrahlung. By explicitly calculating the W-strahlung cross section, we demonstrated that helicity suppression is lifted for this process, causing it to dominate over $\chi\chi \to e^- e^+$ for annihilations occurring today. We found that W/Z behave as massive photons in this context, with longitudinal polarization states making zero contribution to the cross section.

We found the dominance of electroweak bremsstrahlung processes to be most pronounced in the limit where the mass of the boson mediating dark matter annihilation does not greatly exceed the mass of the dark matter particle. The region of parameter space where χ and η are approximately degenerate is of great interest in many models, since it coincides with the coannihilation region where both $\chi\chi$ and $\chi\eta$ annihilations are important in determining the relic dark matter density, often a favored parameter region in SUSY scenarios.

By re-scaling our result for W-strahlung, we calculated the cross section for the Z-strahlung process. Adding contributions from W, Z, and γ bremsstrahlung processes, we show the total bremsstrahlung cross section to be $7.16\sigma_{e^+e^-\gamma}$ for values of m_χ above the threshold for W/Z production, highlighting the significance of electroweak processes in this context.

4

Electroweak Bremsstrahlung as a Probe for Dark Matter in Colliders

One of the most exciting possibilities in the search for dark matter involves producing and detecting such particles at the LHC.

The focus of this work is to investigate collider signatures of dark matter through purely electroweak bremsstrahlung. These processes can lead to either a mono-W [92] or mono-Z [93] signal, in which an electroweak gauge boson recoils against $\not{E}_T$. Specifically, we consider a mono-Z process, $q\bar{q} \to \chi\chi Z$, and highlight some unique kinematical features of this channel which make it an interesting and important complement to jet and photon based searches. Because of this unique kinematics, signals may be distinguished from backgrounds even if rates are not as large as for other bremsstrahlung processes. As a result, depending upon the model, this new signal provides either new discovery potential for dark matter at the LHC, or, equally interestingly, information supplemental to other observable channels to further pin down dark matter model-dependent parameters.

We examine the expected signatures of the mono-Z process $q\bar{q} \to \chi\chi Z$ at the

LHC, relative to the SM backgrounds. We demonstrate these signatures by implementing a specific DM model in which the DM couples directly to quarks. This is used to demonstrate proof of principle for a mono-Z dark matter search, rather than being proposed as a fully self-contained particle physics model. However, many of the features discussed will be generically applicable in all WIMP models.

Electroweak bremsstrahlung has recently received considerable attention in the context of dark matter annihilation and indirect detection [160, 162, 165, 167, 168, 173–181]. As discussed in Chapter 3, in certain models, bremsstrahlung can play an important role in lifting a helicity suppression of the lowest order annihilation process, thus becoming the dominant annihilation mode. The possibility that lifting helicity suppression might enhance electroweak bremsstrahlung associated with dark matter production at the LHC motivated our initial investigations. However, we find that helicity unsuppression negligibly affects rates in the kinematically accessible detection regimes which we consider. Nevertheless, signals rise above standard model backgrounds.

In Section 4.1 we describe the dark matter – mono-Z signatures at the LHC, and outline the dominant SM backgrounds. In Section 4.2 we introduce a simple DM model for which we examine the mono-Z signal, and calculate the production cross section. Here we also present a set of kinematic cuts designed to largely eliminate the SM backgrounds while preserving an observable number of signal events. Existing observational constraints on the model are discussed in Section 4.3, our main results are presented in Section 4.4, and we conclude in Section 4.5.

4.1 LHC Signatures and Backgrounds

The $\chi\chi Z$ production process is pictured schematically in Fig. 4.1. In Section 4.2 we will introduce a specific DM model in order to explore this process in more

detail. Here we will outline some of the general features of the $\chi\chi Z$ final state, along with the relevant SM backgrounds.

4.1.1 The $Z\chi\chi$ final state

Key to the discovery of the $\chi\chi\,(Z \to f\bar{f})$ final state from within the myriad of SM backgrounds is the correct reconstruction of a Z boson from the invariant mass of its decay products. We consider the muonic decay mode which, while having a low branching fraction ($\sim 3\%$), provides for a very clean invariant mass reconstruction. It also has the benefit of having few backgrounds relative to hadronic decay modes.

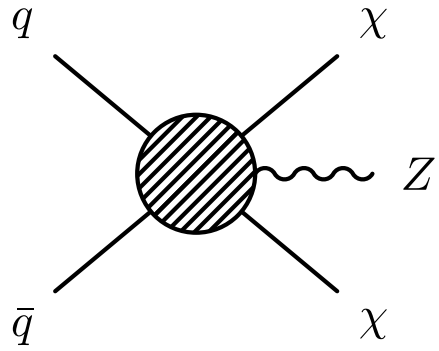

Figure 4.1: Generic electroweak bremsstrahlung process, $q\bar{q} \to \chi\chi Z$, which leads to a mono-Z signal at the LHC.

The recoil of the Z against the heavy dark matter particles results in decay muons with large transverse momentum. The signal of interest will therefore be a pair of high p_T muons, with an invariant mass that reconstructs to that of the Z, and a momentum sum which reveals a large amount of $\not{E}_T$.

We simulate both the signal and background process in the MadEvent [182] event generator. The MadEvent output is then fed into PYTHIA [183] to simulate higher order initial state and propagator radiation effects. A detailed detector simulation is beyond the scope of this work, as our goal is to demonstrate the potential for mono-Z dark matter processes to be observed above background

at the LHC, rather than to calculate precise constraints on specific dark matter models.

4.1.2 Backgrounds

The backgrounds for our process come from channels producing a dimuon pair and $\not{E}_T$. The dominant backgrounds are the leptonic decays of gauge boson producing processes, specifically ZZ, $ZW^{\pm}$, W^+W^- and $t\bar{t} \to b\bar{b}W^+W^-$.

Production of $Z + jets$ can also contribute a $\not{E}_T$ background through jet mismeasurement in the hadronic calorimeter. To test the importance of this background, we used MadEvent to simulate the dominant contribution, Z plus a single jet. Hadronization was performed in PYTHIA, and fast detector simulation was carried out (for $Z + jet$ background alone) in Delphes [184] (using ATLAS parameters), which simulates calorimeter smearing and reconstructs $\not{E}_T$. As expected, this background was found to be sub-dominant to the other backgrounds after the cuts described in Section 4.2.2. At leading order, and in the absence of full detector simulation and pile-up effects, the accuracy of our treatment of this background is obviously limited. Our simulations should, however, be accurate to within an order of magnitude of the true background, which is adequate for our purposes.

As in the $Z + jet$ case, mismeasurement of b jets will contribute to the $\not{E}_T$ spectrum for the process $t\bar{t} \to b\bar{b}W^+W^-$. This contribution is expected to be small compared to neutrinos from $W^{\pm}$ decay, and is therefore neglected. Similarly, mismeasurement of initial state radiation (ISR) in the form of gluon jets can contribute a $\not{E}_T$ background. Given the limited accuracy of PYTHIA in simulating these higher order process, we do not consider these effects. However, we expect their contributions to $\not{E}_T$ will be small, based on our simulations of the $Z + jet$ background.

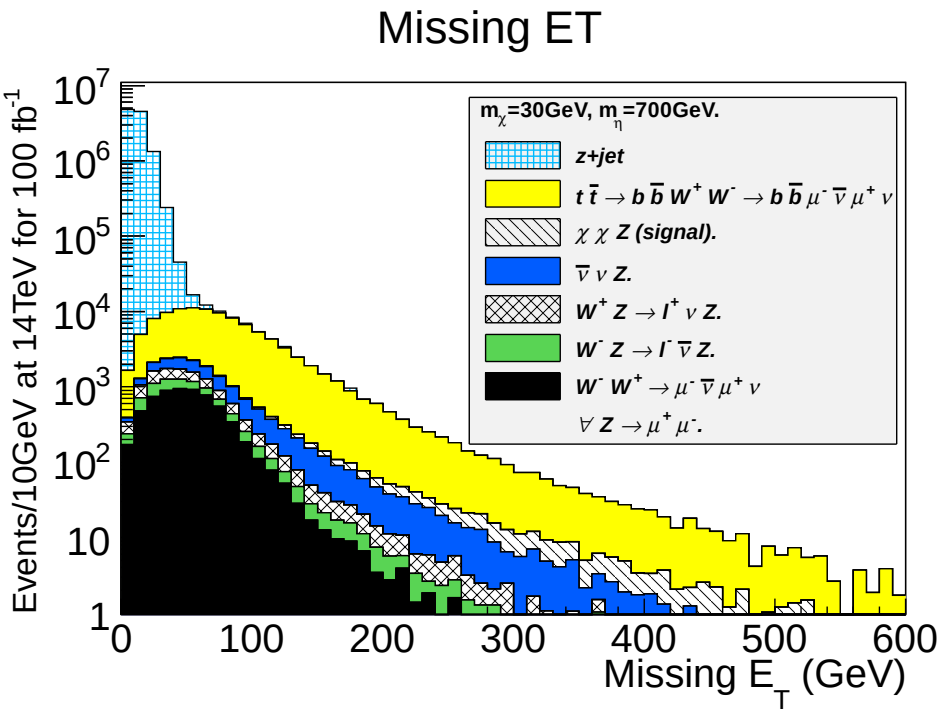

Figure 4.2: Modes contributing to full $\not{E}_T$ spectrum for signal and background for $m_\chi = 30$ GeV and $m_\eta = 700$ GeV, after inclusive p_T and invariant mass cuts. The signal cross section ($\rightarrow \chi\chi Z$) is calculated with a coupling that produces the observed relic abundance.

The relative contributions of various backgrounds before the implementation of the full set of cuts employed in this work can be seen in Fig. 4.2. Cuts on the invariant mass of the muon pairs ensure that NLO contributions from $\gamma \rightarrow \mu^+\mu^-$ are negligible in these processes. The NNLO process $gg \rightarrow ZZ$ can modify the ZZ background by up to 15% [185]; given the level of accuracy desired in this work, we neglect these contributions. These backgrounds are further reduced or eliminated through cuts described in Section 4.2.2.

As evident from Fig. 4.2, the $Z + jet$ background is substantial. This same final state is also the dominant background for the related mono-jet DM search channel. However, we expect this background can be removed more easily for

mono-Z's than for mono-jets. For a mono-jet search the invisible decays $Z \to \nu\bar{\nu}$ provide a large $\not{E}_T$ background, with kinematics very similar to the $\chi\chi + jet$ signal searched for. In contrast, $Z + jets$ contributes to the mono-Z background through $Z + jet \to \mu^+\mu^- + jet$, with $\not{E}_T$ arising only via jet mismeasurement. This is kinematically very different from our $\chi\chi + Z$ signal and, as we will show below, can be removed relatively easily with selection cuts. The sub-dominance of high cross section QCD backgrounds relative to electroweak processes is an appealing aspect of the mono-Z signal.

4.2 The Model and Event Selection

To illustrate the potential for observing a mono-Z dark matter signal at the LHC, we introduce a toy model in which this process has a significant rate. We will then detail event selection criteria that allow the backgrounds to be largely removed.

4.2.1 An Example DM Model

We take the DM to be a gauge-singlet Majorana fermion, χ, which couples to the quark doublet, $Q_{\rm L}$, via the interaction term

$$\begin{aligned} \mathcal{L}_{\rm int} &= f_{ud}\bar{Q}_{\rm L}\eta\chi_{\rm R} + h.c. \\ &= f_{ud}\left(\eta_u\overline{u}_{\rm L} + \eta_d\overline{d}_{\rm L}\right)\chi_{\rm R} + h.c., \end{aligned} \tag{4.1}$$

where f_{ud} is a coupling constant and η is a scalar field that that transforms as $\eta \sim (3, 2, 1/3)$ under the SM gauge groups. (This model is a related to the one considered in the previous chapter, modified such that the scalar is charged under $SU(3)_C$.)

Such couplings are also present in SUSY models, with χ identified as a neutralino and η a squark doublet. An obvious difference, however, is that we have

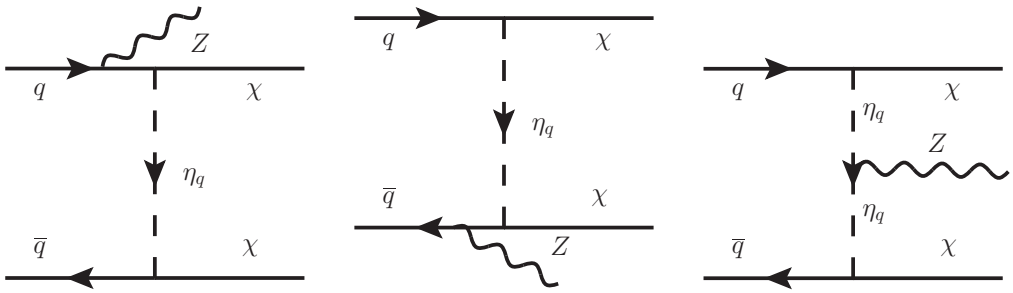

Figure 4.3: t-channel processes contributing to electroweak bremsstrahlung in annihilations to dark matter. Not shown are the three corresponding u-channel diagrams.

no gluino analogue in our model. In some sense this model is analogous to a SUSY model in which the gluinos are too heavy to be kinematically accessible at the LHC. As a consequence, despite this model being substantially simpler than many SUSY models, both in couplings and free parameters, the LHC signatures presented in this work may still be of relevance for some SUSY searches (especially if the parameter space of more minimal SUSY models is increasingly ruled out), perhaps providing a complementary signal to further constrain models.

The interactions in Eq. 4.1 allow for direct annihilation of quarks into a $\chi\chi$ pair via t-channel and u-channel η exchange. Of interest to this work are processes to the next order in α_W, in which a Z boson is radiated from the initial state quarks or the internal propagator. Contributing to the mono-Z process $q\bar{q} \to \chi\chi Z$ are the three t- and u-channel diagrams shown in Fig. 4.3.

The Mathematica package FeynRules [186] was used to formulate the Feynman rules for the model of Eq. 4.1. The rules were interfaced with the MadGraph package [182] to calculate the scattering amplitudes for the processes in Fig. 4.3. These amplitudes were then input into the MadEvent event generator, which calculated the LHC-relevant cross section $pp \to \chi\chi Z$ for a given f_{ud}, and for various

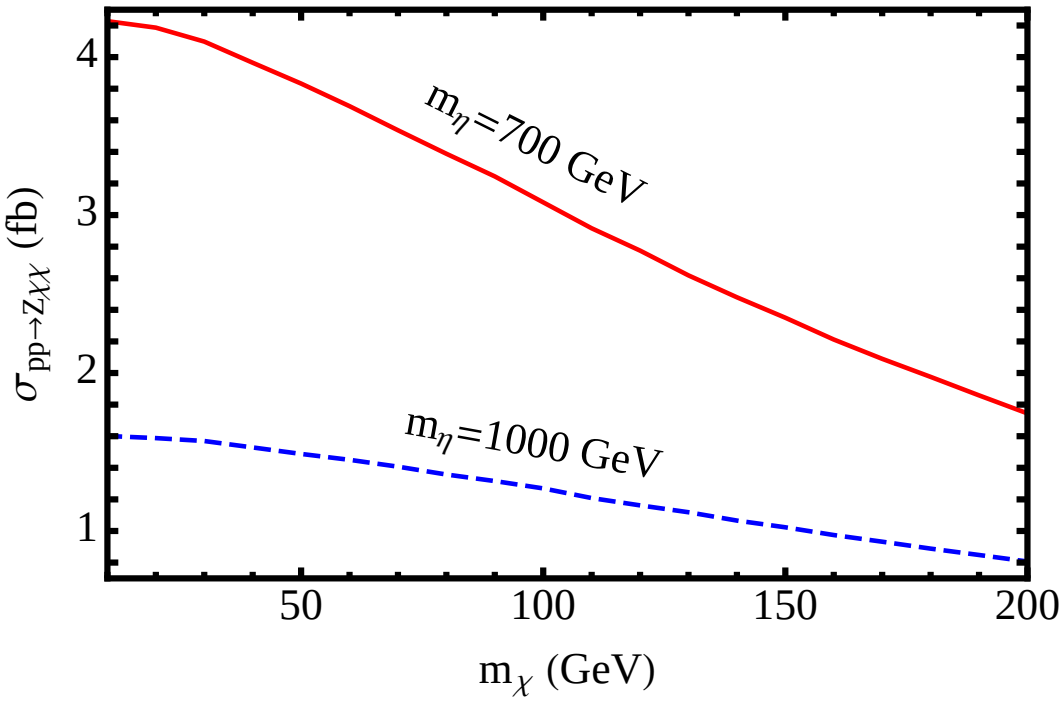

Figure 4.4: Cross section for process $pp \to \chi\chi Z$ at CoM of 14 TeV as a function of DM mass. Red line (upper) corresponds to $m_\eta = 700$ GeV, blue (lower) to $m_\eta = 1$ TeV. Both cross sections calculated for $f_{ud} = 1$, and using CTEQ6L1 PDF's.

choices of m_χ and m_η . All cross section calculations were performed in the proton center of momentum frame. The probability amplitudes were integrated over the CTEQ6L1 [187] parton distribution functions (PDF). Given that the LHC is a proton-proton collider, the valence quarks contribute to the q distributions, while the sea-quarks of course contribute to both the q and $\bar{q}$ distributions.

Cross sections at 14 TeV CoM are displayed in Fig. 4.4 as a function of m_χ, for values of m_η relevant to electroweak-scale physics.

4.2.2 Event Selection

Now that we have a model which produces DM along with a Z-boson, we will examine how this channel may be detected at a hadron collider. While the backgrounds presented in Section 4.1.2 have rates much larger than our signal, they can be substantially reduced with an educated set of cuts on measured events. We make cuts on the invariant mass of the muon pair within a 60 GeV window centered on the Z mass, which greatly reduces the contribution from non-Z backgrounds, namely W^+W^- and $t\bar{t}$ production.

The presence of the heavy χ in our signal process ensures large amounts of $\not{E}_T$. This can be seen clearly in Fig. 4.2, which shows the number of expected collider events as a function of missing energy, in 10 GeV bins. As expected, the number of signal events with large $\not{E}_T$ are at least comparable to all SM backgrounds. We choose a missing energy cut of $\not{E}_T > 150$ GeV to remove a large fraction of the background events, including the bulk of the $Z + jet$ background. It is important to note that due to the very large cross sections for $t\bar{t}$ and $Z + jet$ before the implementation of cuts, the statistics in these two contributions lead to evident fluctuations at high $\not{E}_T$ in Fig. 4.2.

The Z in the final state can be highly boosted by its recoil off the heavy DM particles; we therefore expect its decay products to have large p_T. We apply the conservative inclusive cut of $p_T > 50$ GeV on the muon transverse momentum (i.e. require at least one muon in the final state with $p_T > 50$ GeV).

A further consequence of the Z being produced relativistically is that the muons from the decay process will be produced nearly co-linear with each other. This co-linearity ensures a low ΔR between the pair, where ΔR is defined to be

$$\Delta R \equiv \sqrt{\Delta\phi^2 + \Delta\eta^2}, \tag{4.2}$$

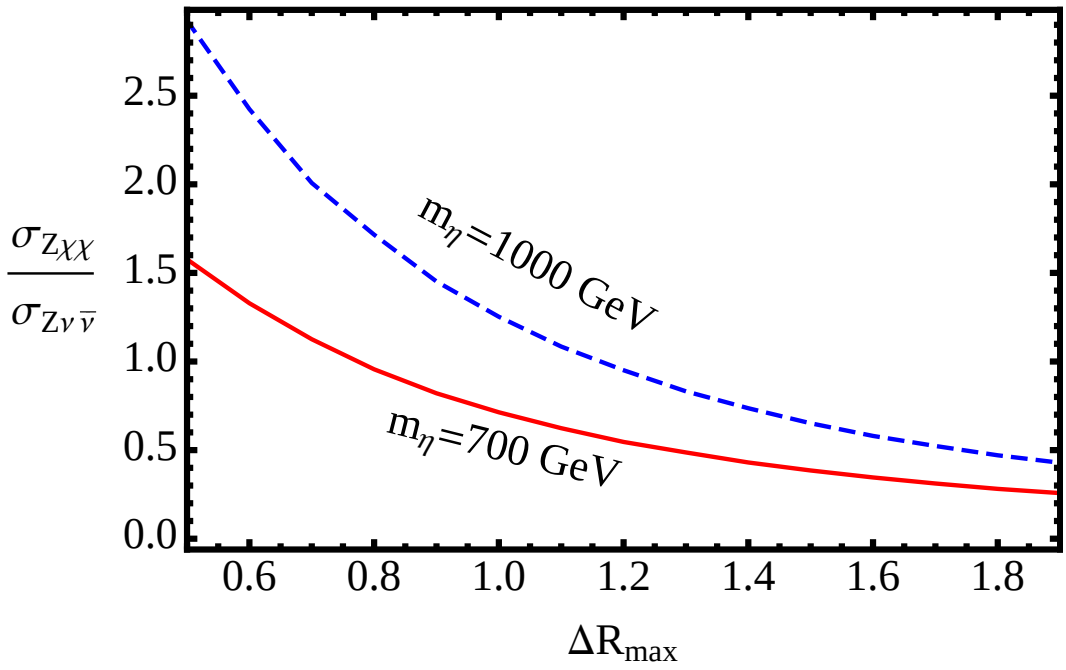

Figure 4.5: Ratio $\sigma_{\chi\chi Z}/\sigma_{Z\nu\bar{\nu}}$ at 14 TeV CoM and for $m_\chi = 30$ GeV, as a function of the cut on maximum $\Delta R = \sqrt{\Delta\phi^2 + \Delta\eta^2}$ between muons in the final state. Red line (lower) corresponds to $m_\eta = 700$ GeV, blue (upper) to $m_\eta = 1$ TeV.

where ϕ is the azimuthal angle and η is the pseudo-rapidity of a particle in the detector.

Figure 4.5 shows the ratio of signal cross section to the $\nu\bar{\nu}\,(Z \to \mu^+\mu^-)$ background as a function of cut on maximum ΔR, after p_T and dimuon invariant mass cuts, for selective points in the model parameter space. This background is useful for comparisons, as it is the dominant $\not{E}_T$ background in the region of interest. The signal to background is maximized for lower ΔR, with both cross-sections becoming equal around $\Delta R_{max} \sim 1$. To preserve signal events, we choose the conservative cut of $\Delta R < 1$. This cut should effectively discriminate against the W^+W^- and $t\bar{t}$ backgrounds, which produce muon pairs with a broad ΔR distribution. The effectiveness of this choice of cut can be seen in the top right

hand panel of Fig. 4.11, which displays the same data as Fig. 4.2 but with full set of cuts applied, including the cut on ΔR.

The missing energy in the background $Z+jet$ is a result of jet mismeasurement in the hadronic calorimeter, thus a large amount of $\not{E}_T$ is present in events with high jet p_T. These types of events typically have a highly boosted Z, and subsequently produce muon pairs with lower ΔR separation than low $\not{E}_T$ events.

We note that the detector simulation program Delphes requires that muons counted individually be isolated within a cone of $\Delta R < 0.5$. A consequence of these two factors is that in the majority of $Z + jet$ events with $\not{E}_T > 150$ GeV, muons from Z decay do not pass Delphes' isolation criterion and are subsequently rejected, reducing this background significantly. Aside from necessarily using Delphes for producing the $\not{E}_T$ spectrum of the $Z + jet$ background, we do not use detector simulation in this work. Instead, we enforce $\Delta R > 0.5$ between the paired muons.

In this work we have been conservative in that we have not applied any jet related cuts, despite their obvious utility in distinguishing real $\not{E}_T$ from jet mismeasurement. It is possible to further improve signal relative to QCD backgrounds by removing events in which jet and $\not{E}_T$ directions are correlated. Tagging of b jets may also be used to reduce the $t\bar{t}$ background. Below we show that such additional cuts, while no doubt useful, are not necessary to obtain an observable signal to background ratio.

4.3 Model Constraints

When calculating LHC signals, we adopt model parameters that produce the correct DM relic abundance. We also ensure the parameters are in accordance with current direct detection and collider bounds. These constraints are described in detail here.

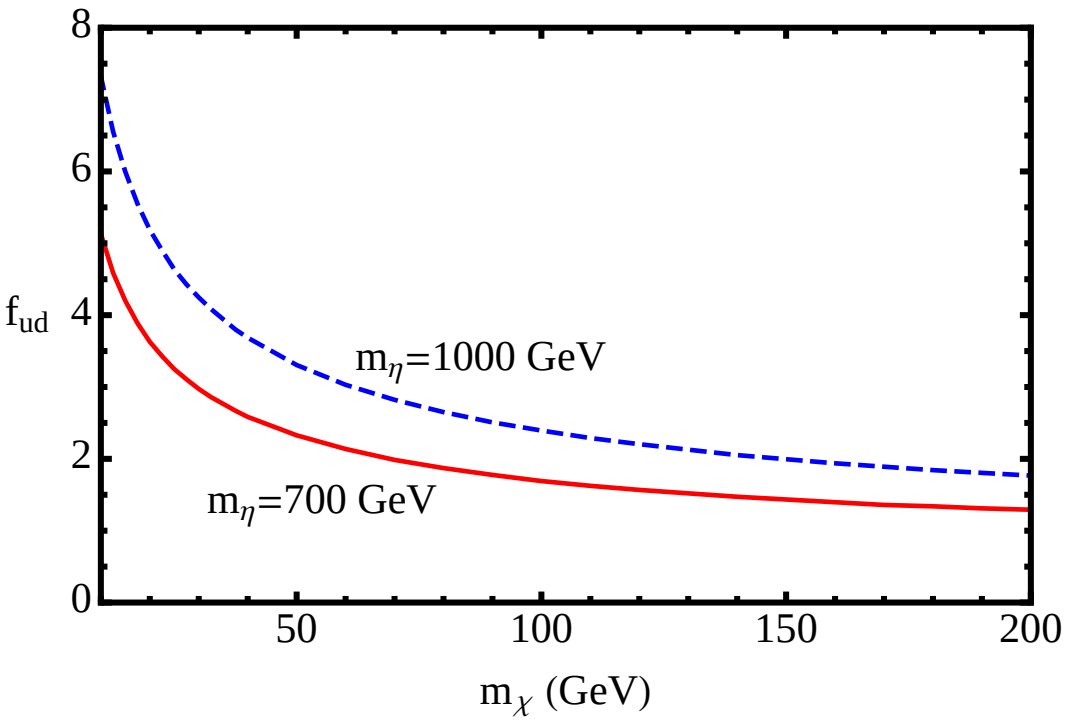

Figure 4.6: The minimum allowed coupling constant f_{ud} in order to satisfy the requirement that the contribution to the DM relic density from this model be less than or equal to the total DM relic density, $\Omega_{DM}h^2 \simeq 0.11$. Red line (lower) corresponds to $m_\eta = 700$ GeV, blue (upper) to $m_\eta = 1$ TeV. Note that the expansion parameter $f^2/4\pi$ remains perturbative for $f \lesssim 4\pi \sim 12.5$.

4.3.1 Freezeout

We work in the context of the standard WIMP scenario, in which the DM was in thermal equilibrium in the early Universe up until the time of thermal freezeout, at which point the relic abundance was set. For a given DM mass, we wish to choose values of the coupling constant f_{ud}, and η mass, such that the DM freezes out with the correct relic abundance.

The process which kept χ in equilibrium before thermal freezeout was $q\bar{q} \to \chi\chi$. The relic density of χ was therefore determined by parameters f_{ud}, m_χ

and m_η. Following [94, 95], we use a semi-analytic solution to the co-moving Boltzmann equation, and the inferred value $\Omega_{DM}h^2 \simeq 0.11$ to place constraints on f_{ud} for given values of m_χ and m_η. Results are displayed in Fig. 4.6. If the coupling were any smaller than the constraints in Fig. 4.6, then the DM would have been overproduced in the early universe, yielding an abundance greater than that observed today. On the other hand, if it were any larger, then the relic abundance would be smaller than observed. If there are other DM species contributing to the relic abundance, then the constraints on f_{ud} serve as lower limits, since the DM candidate under consideration need not contribute the entire relic abundance.

4.3.2 Direct Detection

In the model under discussion, quarks couple to the beyond-SM sector via a $q\chi\eta$ vertex with strength f_{ud}. Consequently, care is required to avoid direct detection constraints. The operator in Eq. 4.1 allows for χ-quark scattering via the s and u-channel η exchange graphs in Fig. 4.7, which can in turn be related to χ-nucleon scattering.

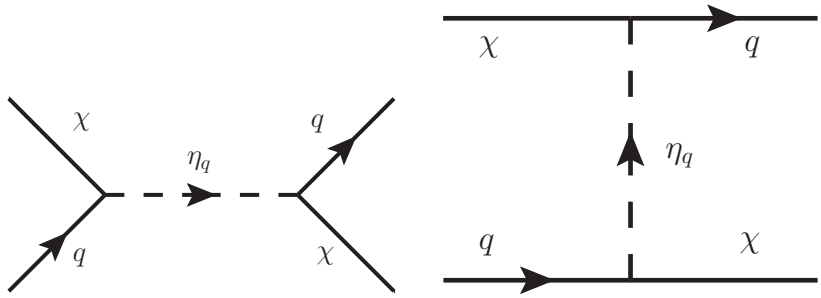

Figure 4.7: Fundamental processes contributing to DM–nucleon scattering.

The couplings in Eq. 4.1 Fierz transform into couplings to nucleons that have both spin-dependent and spin-independent contributions. The strongest constraints on our model come from the spin-independent limits from the XENON100

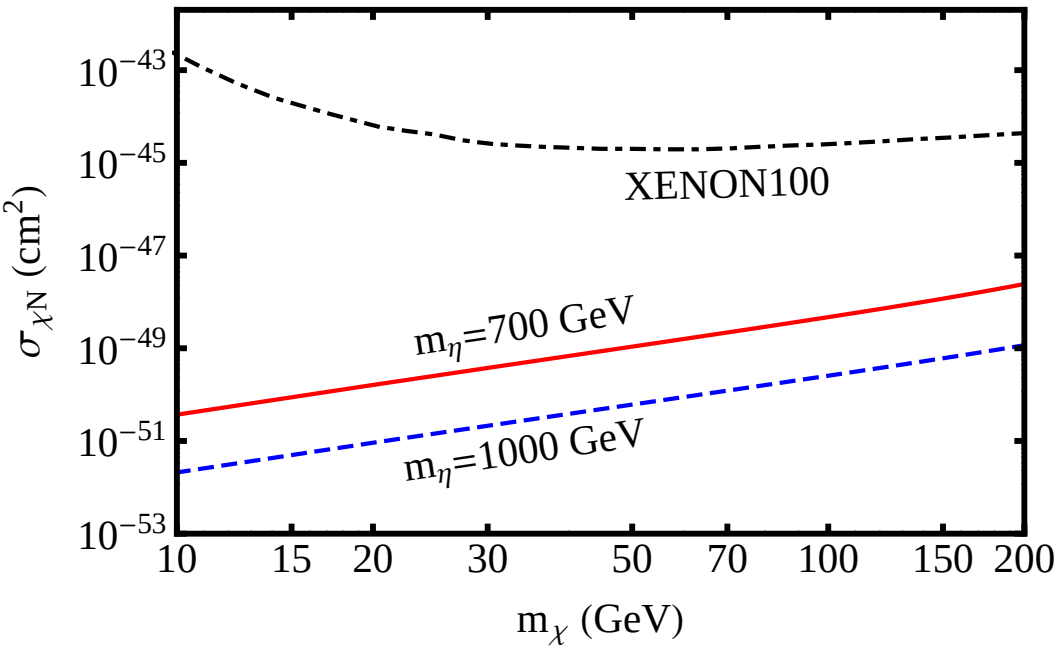

Figure 4.8: The spin-independent $\chi-$nucleon scattering cross section. Red line (upper) corresponds to $m_\eta = 700$ GeV, blue (lower) to $m_\eta = 1$ TeV. Shown in dashed is the upper limit on the SI cross section from XENON100 experiment.

experiment [60], which looks for excitations in ultra-cold liquid Xe resulting from DM scattering events. We performed the calculation of the SI χ-nucleon cross section in the current model using the MicrOMEGAs [188] software package, taking the Lagrangian in Eq. 4.1 as input. The calculation was done for values of f_{ud} that produce the correct relic abundance (Fig. 4.6) for various values of m_η and a range of DM masses. The results are displayed in Fig. 4.8, alongside the upper bound on the cross section allowed by XENON100. Clearly the model parameters considered in this work are allowed by the XENON100 constraint. Note that if there are additional DM particles, and the DM candidate considered here is not required to contribute the entire relic density, the curves in Fig. 4.8 denote lower

limits on the scattering cross section.

4.3.3 Collider Constraints

Through the early part of 2012, roughly 5 fb^{-1} of data were analyzed by both the ATLAS and CMS collaborations. Thus far no significant discrepancies with Standard Model predictions have been found. Discrepancies not seen at present include large missing energy signals and new particles such as those predicted in numerous extensions of the SM.

The absence of novel signals has put ever tighter constraints on models of physics beyond the SM. As discussed in Section 4.2.1, the model described in the present work is purely phenomenological, but does possess some similarities to a SUSY model (with obvious differences being an absence of gluinos and only first generation quark couplings). This makes it somewhat difficult to directly compare existing bounds with our model. However, we have chosen values of parameters such as the η masses and $\eta - \chi$ mass differences which are not currently ruled out by squark mass and squark-neutralino mass difference constraints, respectively, for a simplified model spectra (SMS) of SUSY.

Examples of these constraints for an SMS from CMS data are given in [74–77]. The SMS are motivated by popular SUSY frameworks such as the constrained minimal supersymmetric standard model (cMSSM) and the general gauge mediation model (GGM). Of particular relevance are the constraints derived in [75], in which the authors consider a simplified model with a heavy gluino and two squark generations. This very closely resembles the model at hand, the only effective difference being the number of scalar degrees of freedom present in the model. A lower bound of 780 GeV was placed on the squark mass, which maps to the constraint $m_\eta \gtrsim 600$ GeV in the model considered here. Conservatively, we only

consider η masses above 700 GeV.

4.4 Results

The results of our simulations can be seen in Figs. 4.9 – 4.13. These figures sample a range of model parameters, LHC energies and integrated luminosities, and use values of f_{ud} adherent to the constraints in Fig. 4.6. Plotted are expected signal and background events per 10 GeV bin as a function of missing energy and the p_T of the μ^-, after the application of cuts outlined in Section 4.2.2. The p_T distributions for μ^+ and μ^- differ due to the CP-breaking valance quark contribution to the parton distributions of the proton. However, given the high CoM energy of LHC collisions, this is a small effect. We thus do not show the μ^+ p_T distributions, being nearly indistinguishable from those of μ^-.

In order to get accurate statistics in regions with low numbers of events, all of our simulations except those of $Z+jet$ have at least four times as many simulated events as expected LHC events for the given integrated luminosity. For the $Z+jet$ background there are ~ 1.3 simulated events per LHC event. All event numbers are then rescaled for our figures, to the number of events expected at the LHC.

All backgrounds have been significantly reduced by our choice of cuts, and the remaining background is dominated by $Z\nu\bar{\nu}$. This can be understood given that it passes Z selection criteria, and contains a pair of neutrinos, implying larger amounts of $\not{E}_T$ than other backgrounds, and a greater resilience to our missing energy cut.

Fig. 4.9 shows event numbers corresponding to an integrated luminosity of 5 fb^{-1} and a CoM energy of 7 TeV. It is clear that our selection cuts are effectively distinguishing signal from background. Results for $m_\chi = 10$ GeV and $m_\eta = 700$ GeV indicate an excess of a few events after integration across all bins, demon-

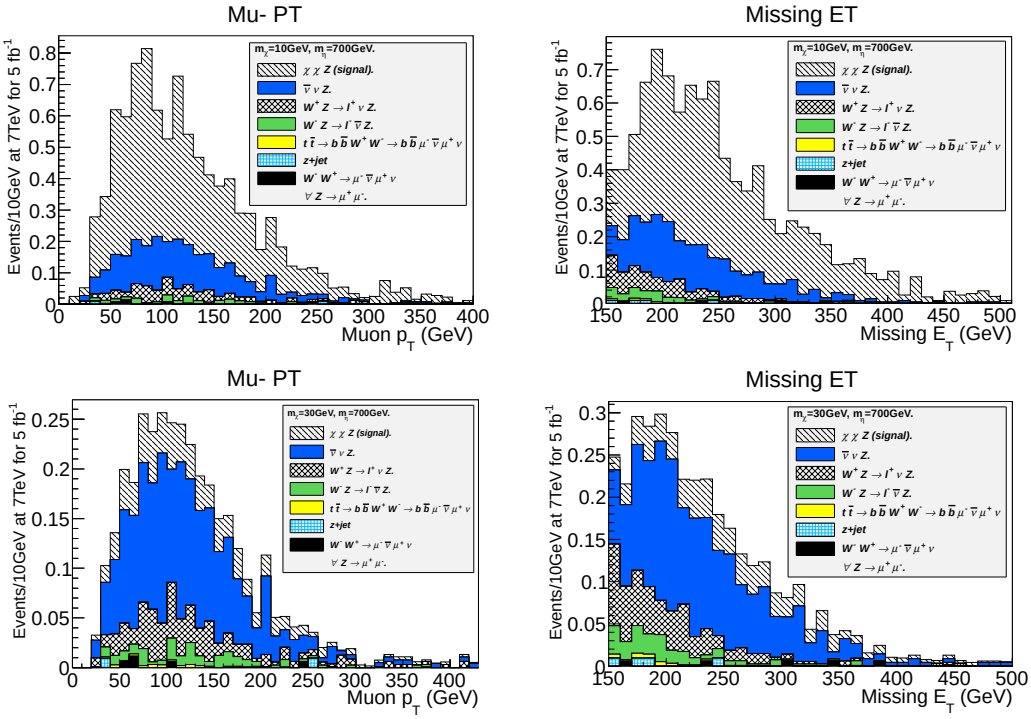

Figure 4.9: Events passing selection criteria in Section 4.2.2, at $\sqrt{s} = 7$ TeV and 5 fb^{-1} of data, for $m_\eta = 700$ GeV, comparing $m_\chi = 10$ GeV and 30 GeV.

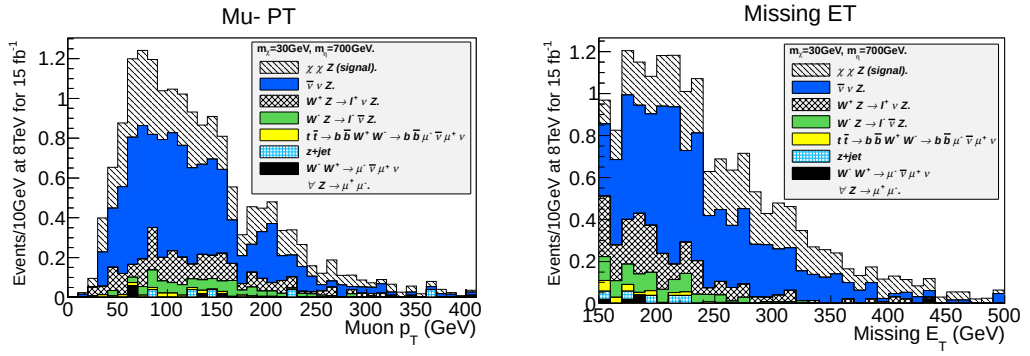

Figure 4.10: As Fig 4.9, with $\sqrt{s} = 8$ TeV and 15 fb^{-1} of data, for $m_\chi = 30$ GeV and $m_\eta = 700$ GeV.

strating the potential for constraining the model using current data. For $m_\chi = 30$ GeV the signal strength is significantly weaker. In this case, a CoM energy of 8 TeV and an integrated luminosity of 15fb^{-1} are required for the signal to be visible, as demonstrated in Fig. 4.10. With the intention of studying heavier dark matter masses, we focus primarily on the higher integrated luminosities and CoM energies, for which the expected signal is significantly enhanced.

Looking to the future, we turn our attention to the LHC's design CoM energy of 14 TeV, and a larger integrated luminosity of 100fb^{-1}. Figs. 4.11 - 4.12 show the expected signal for varying model parameters m_χ and m_η. For the regions of parameter space considered, most bins have a signal to background which exceeds 10%, reaching up to 70% in some bins for the parameter choices $m_\chi = 30$ GeV and $m_\eta = 1$ TeV. We expect such an excess, if it exists, to be clearly visible in future data. Consequently, the non-observation of this signal has the potential to place strong constraints on this type of model.

The signal strength decreases as the dark matter mass increases, approaching invisibility as m_χ approaches 100 GeV. Though not implemented here, this decrease in signal to background with increasing m_χ could potentially be offset by fine tuning cuts on measured events for a given dark matter mass. Alternatively, one could relax the requirement that χ constitute all of the dark matter, allowing an increase in f_{ud}, which would in turn scale the production cross section. An example of such non-saturating dark matter can be seen in Fig. 4.13. Here, f_{ud} is taken to be 3, in contrast to the value of 1.67 required to satisfy the relic abundance constraint. With $f_{ud} = 3$, χ contributes only $\sim 10\%$ to the total dark matter abundance.

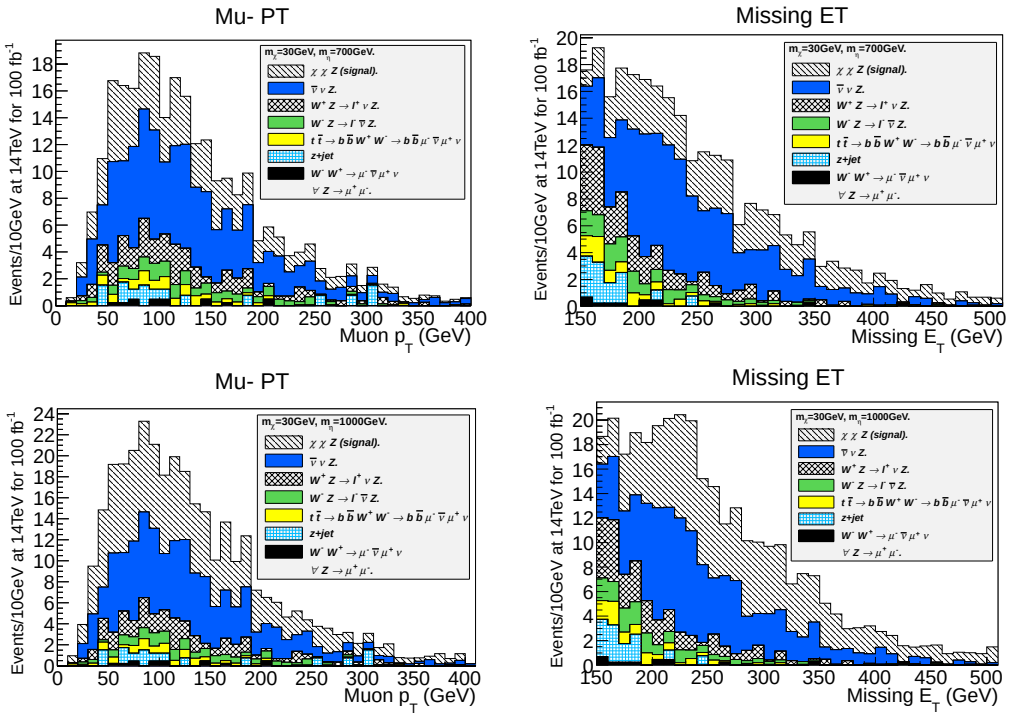

Figure 4.11: As Fig. 4.9, with $\sqrt{s} = 14$ TeV and 100 fb^{-1} of data, for $m_\chi = 30$ GeV, comparing $m_\eta = 700$ GeV and 1000 GeV.

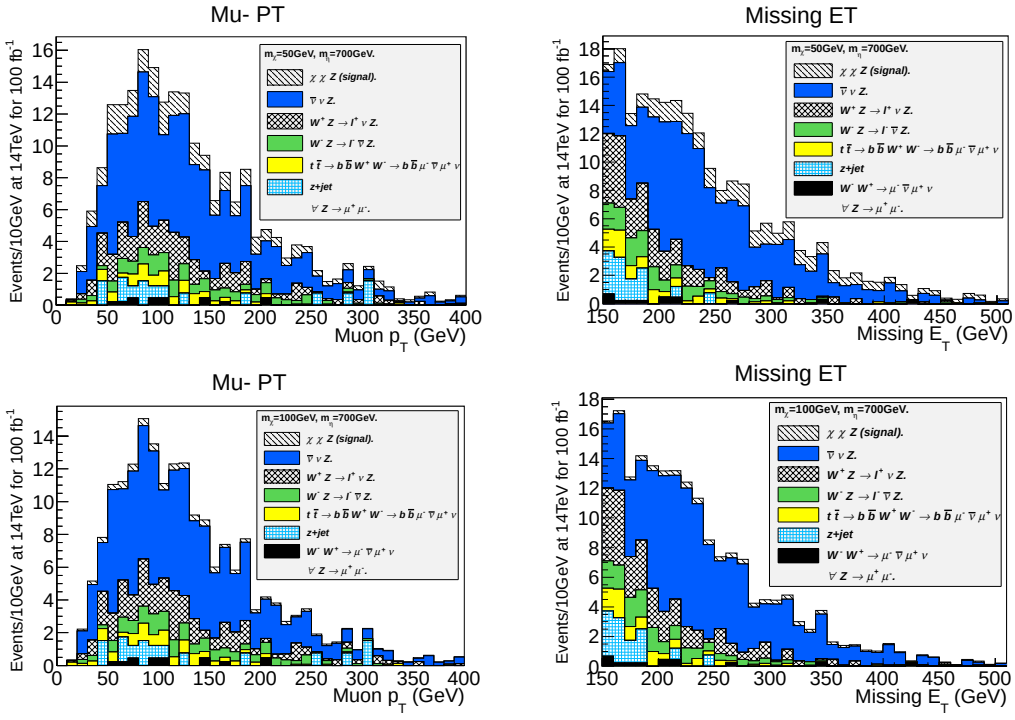

Figure 4.12: As Fig. 4.9, with $\sqrt{s} = 14$ TeV and 100 fb^{-1} of data, for $m_\eta = 700$ GeV, comparing m_χ =50 GeV, and 100 GeV.

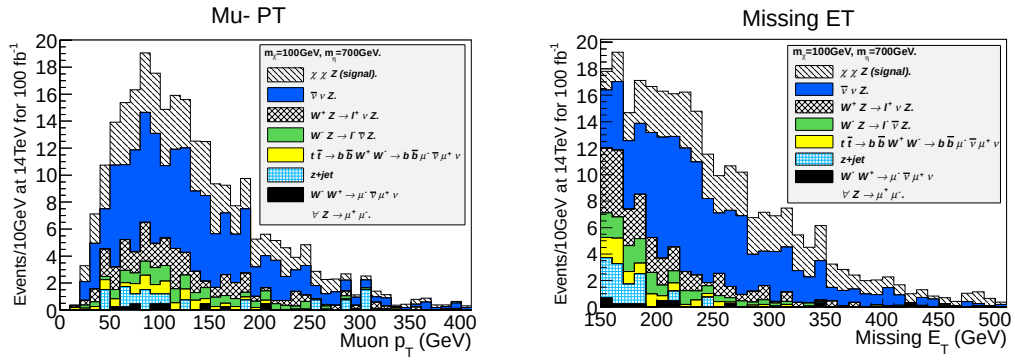

Figure 4.13: As Fig. 4.12, with $m_\chi = 100$ GeV and $m_\eta = 700$ GeV, for $f_{ud} = 3$, which corresponds to 10% of present relic abundance.

4.5 Conclusions

There are many different search channels for dark matter at the LHC, most of those being dependent on the specifics of the model under consideration, supersymmetric or otherwise. A key hallmark of any of these searches are some set of high p_T events, against whose momentum large amounts of $\not{E}_T$ can be reconstructed. A complete dark matter search must take into account signatures in all possible channels. In this work, we have pointed out the relevance of mono-Z (electroweak bremsstrahlung) processes as a search channel for dark matter. In particular, we advance the process $pp \to \chi\chi Z$, where the Z decays muonically. The final state appears as a pair of high p_T muons, with an invariant mass in the Z window, and large amounts of $\not{E}_T$. Despite having a cross section which is low relative to processes with jets in the final state, this process has few Standard Model backgrounds, and these can be tamed by modest event cuts. By applying a specific model for dark matter, with direct dark matter coupling to quarks, we have demonstrated that this process in principle could be highly visible in future data from LHC upgrades. A dedicated study by the ATLAS or CMS collaboration with full background and detector simulation could confirm this. We have found that for certain choices of model parameters an excess of events may be visible across a broad range of energy bins; some bins contain up to a 70% signal to background ratio. Although the signal becomes weaker with rising dark matter mass, becoming negligible near $m_\chi \simeq 100$ GeV, our method may continue to prove valuable for larger dark matter masses by optimization of the choice of cuts. As a result, this mono-Z search can at the very least provide important complementary information to jet and photon based dark matter searches. This mono-Z search is relevant whether or not its discovery potential is competitive with mono-jets and mono-photons, due to the unique kinematic aspects of Z decay in distinguishing

mono-Z's from other bremsstrahlung based search channels.

5

Conclusion

Though dark matter makes up the dominant fraction of matter in the Universe, little is known about its internal properties. It is unclear if it is absolutely stable, whether or not it has interactions with the SM, and how such interactions might manifest observationally. In this work we have looked in detail at some of these possibilities.

In Chapter 2 we investigated models for dark matter decay, implemented as a solution to the small scale structure problems inherent to ΛCDM. We reviewed constraints on the lifetime for decays into photons or e^+e^- pairs, and derived constraints on processes involving neutrinos in the decay products. We then went on to demonstrate the theoretical feasibility of the decaying dark matter scenario by constructing explicit particle physics models designed to satisfy the criteria necessary for the desired modification of structure formation. We introduced a real scalar field and two Majorana dark matter candidates, one of which was meta-stable, decaying into the lighter of the two plus a relativistic final state. We explored two scenarios, one in which the decay products contained visible particles, and the other in which they contained invisible states only. We found both scenarios to be feasible from a theoretical/model-building standpoint, though constrained by

observation. We found decays into e^+e^- pairs to be tightly constrained, with dark matter lifetimes between 1-30 Gyr (as preferred by [8] to solve the dwarf halo deficit problem) completely excluded in the context of this model. We found decays into Dirac neutrinos disfavored in this model, whereas decays into Majorana neutrinos allowed for a broad range of DM lifetimes.

For a certain class of models for Majorana dark matter, the cross section for purely s-wave annihilation into light fermions is helicity suppressed. For these models the annihilation cross section contains p-wave contributions at leading order, and is v^2 suppressed. Though it has been long established that the bremsstrahlung of a photon during annihilation can lift helicity suppression, until recently the possibility of electroweak bremsstrahlung has been largely ignored. In Chapter 3 we considered the W-strahlung process. Within the context of a toy model we explicitly performed the calculation of this cross section, and demonstrated that it contained neither helicity nor velocity suppression. We found the process $\chi\chi \to e^+\nu W^-$ to dominate over $\chi\chi \to e^+e^-$ for annihilations occurring in the galactic halo today, approaching a relative enhancement of 10^3 as the mediator mass approached that of the DM. By re-scaling our result for W-strahlung, we calculated the cross section for the Z-strahlung process, and showed the total bremsstrahlung cross section to be significantly larger than for γ bremsstrahlung alone, with $\sigma_{\text{brem, total}} = 7.16$ $\sigma_{e^+e^-\gamma}$ in the limit $m_\chi \gg m_W$.

The potential significance of electroweak bremsstrahlung during dark matter annihilation highlights the possibility that it is significant in a collider context. In Chapter 4 we explored the signatures of DM at the LHC through the mono-Z search channel. In the context of a toy model, we explored the possibility of a mono-Z being produced via the process $q\overline{q} \to \chi\chi Z$. We considered muonic decays of the Z, looking for a pair of high p_T muons with an invariant mass in the Z window accompanied by large amounts of $\not{E}_T$, attributed to the dark matter χ.

We carried out simulations of LHC collisions at both current and future center of mass energies, proposing a set of cuts tailored to effectively distinguish this signal from SM backgrounds. We found that for certain regions of parameter space there may be a visible excess above backgrounds across a broad range of energy bins, finding that for certain parameter choices up to 70% signal to background could be visible at the LHC's design CoM energy of 14 TeV. Although we would expect the signal to become weaker with rising dark matter mass, approaching negligibility near $m_\chi \simeq$ 100 GeV, it may be bolstered by fine tuning the choice of cuts, or sacrificing the requirement that χ make up the entirety of the relic abundance. In demonstrating its visibility we have demonstrated importance of the mono-Z search channel, and shown it to be an important compliment to the well established mono-jet and mono-photon searches.

Publications

1. **"Lifetime Constraints for Late Dark Matter Decay"**

   N. F. Bell, A. J. Galea, K. Petraki.

   Phys.Rev. D82 (2010) 023514, [arXiv:1004.1008].

2. **"A Model for Late Dark Matter Decay"**

   N. F. Bell, A. J. Galea, R. R. Volkas.

   Phys.Rev. D83 (2011) 063504, [arXiv:1012.0067].

3. **"W/Z Bremsstrahlung as the Dominant Annihilation Channel for Dark Matter, Revisited."**

   N. F. Bell, A. J. Galea, J. B. Dent, T. D. Jacques, L. M. Krauss, T. J. Weiler.

   Phys.Lett. B706 (2011) 6-12, [arxiv:1104.3823].

4. **"Searching for Dark Matter at the LHC with a Mono-Z"**

   N. F. Bell, A. J. Galea, J. B. Dent, T. D. Jacques, L. M. Krauss, T. J. Weiler.

   Phys.Rev. D86 (2012) 096011, [arXiv:1209.0231].

Bibliography

[1] M. Persic, P. Salucci, and F. Stel, Mon.Not.Roy.Astron.Soc. **281**, 27 (1996), arXiv:astro-ph/9506004.

[2] D. Clowe *et al.*, Astrophys.J. **648**, L109 (2006), arXiv:astro-ph/0608407.

[3] M. Markevitch, (2005), arXiv:astro-ph/0511345.

[4] H. Yuksel and M. D. Kistler, Phys. Rev. **D78**, 023502 (2008), arXiv:0711.2906.

[5] N. F. Bell, A. J. Galea, and K. Petraki, Phys. Rev. **D82**, 023514 (2010), arXiv:1004.1008.

[6] A. H. G. Peter, (2010), arXiv:1001.3870.

[7] A. H. G. Peter, C. E. Moody, and M. Kamionkowski, (2010), arXiv:1003.0419.

[8] M. Abdelqader and F. Melia, Mon. Not. Roy. Astron. Soc. **388**, 1869 (2008), arXiv:0806.0602.

[9] J. L. Feng, M. Kaplinghat, and H.-B. Yu, Phys. Rev. Lett. **104**, 151301 (2010), arXiv:0911.0422.

[10] W. Tucker *et al.*, (1998), arXiv:astro-ph/9801120.

[11] A. Mahdavi, H. Hoekstra, A. Babul, D. Balam, and P. Capak, Astrophys.J. **668**, 806 (2007), arXiv:0706.3048.

[12] Z. Silagadze, ICFAI U.J.Phys. **2**, 143 (2009), arXiv:0808.2595.

[13] J.-W. Lee, S. Lim, and D. Choi, (2008), arXiv:0805.3827.

[14] D. Clowe *et al.*, Astrophys.J. **758**, 128 (2012), arXiv:1209.2143.

[15] V. F. Mukhanov, H. Feldman, and R. H. Brandenberger, Phys.Rept. **215**, 203 (1992).

[16] D. H. Lyth and A. Riotto, Phys.Rept. **314**, 1 (1999), arXiv:hep-ph/9807278.

[17] A. R. Liddle and D. H. Lyth, Phys.Rept. **231**, 1 (1993), arXiv:astro-ph/9303019.

[18] K. A. Olive, Phys.Rept. **190**, 307 (1990).

[19] A. D. Linde, (2005), arXiv:hep-th/0503203.

[20] N. Jarosik *et al.*, Astrophys.J.Suppl. **192**, 14 (2011), arXiv:1001.4744.

[21] SDSS Collaboration, W. J. Percival *et al.*, Mon.Not.Roy.Astron.Soc. **401**, 2148 (2010), arXiv:0907.1660.

[22] A. G. Riess *et al.*, Astrophys.J. **699**, 539 (2009), arXiv:0905.0695.

[23] WMAP Collaboration, E. Komatsu *et al.*, Astrophys.J.Suppl. **192**, 18 (2011), arXiv:1001.4538.

[24] V. Springel *et al.*, Nature **435**, 629 (2005), arXiv:astro-ph/0504097.

[25] L. Bergstrom, P. Ullio, and J. H. Buckley, Astropart.Phys. **9**, 137 (1998), arXiv:astro-ph/9712318.

[26] J. N. Bahcall and R. Soneira, Astrophys.J.Suppl. **44**, 73 (1980).

[27] A. V. Kravtsov, A. A. Klypin, J. S. Bullock, and J. R. Primack, Astrophys.J. **502**, 48 (1998), arXiv:astro-ph/9708176.

[28] J. F. Navarro, C. S. Frenk, and S. D. White, Astrophys.J. **462**, 563 (1996), arXiv:astro-ph/9508025.

[29] B. Moore, T. R. Quinn, F. Governato, J. Stadel, and G. Lake, Mon.Not.Roy.Astron.Soc. **310**, 1147 (1999), arXiv:astro-ph/9903164.

[30] A. W. Graham, D. Merritt, B. Moore, J. Diemand, and B. Terzic, Astron.J. **132**, 2685 (2006), arXiv:astro-ph/0509417.

[31] J. F. Navarro *et al.*, (2008), arXiv:0810.1522.

[32] E. W. Kolb and M. S. Turner, Front. Phys. **69**, 1 (1990).

[33] W. Blok, A. Bosma, and S. McGaugh, (2002), arXiv:astro-ph/0212102.

[34] G. Jungman, M. Kamionkowski, and K. Griest, Phys.Rept. **267**, 195 (1996), arXiv:hep-ph/9506380.

[35] G. D'Amico, M. Kamionkowski, and K. Sigurdson, (2009), arXiv:0907.1912.

[36] D. Hooper, p. 709 (2009), arXiv:0901.4090.

[37] L. Bergstrom, (2012), arXiv:1205.4882.

[38] J. L. Feng, Ann.Rev.Astron.Astrophys. **48**, 495 (2010), arXiv:1003.0904.

[39] G. Bertone, D. Hooper, and J. Silk, Phys.Rept. **405**, 279 (2005), arXiv:hep-ph/0404175.

[40] LAT collaboration, T. F.-. M. Ackermann *et al.*, (2012), arXiv:1205.6474.

[41] E. Storm, T. E. Jeltema, S. Profumo, and L. Rudnick, (2012), arXiv:1210.0872.

[42] D. Hooper, C. Kelso, and F. S. Queiroz, (2012), arXiv:1209.3015.

[43] S. Blanchet and J. Lavalle, JCAP **1211**, 021 (2012), arXiv:1207.2476.

[44] A. Geringer-Sameth and S. M. Koushiappas, Phys.Rev. **D86**, 021302 (2012), arXiv:1206.0796.

[45] S. Palomares-Ruiz, (2008), arXiv:0805.3367.

[46] S. Palomares-Ruiz and S. Pascoli, Phys. Rev. **D77**, 025025 (2008), arXiv:0710.5420.

[47] K. Murase and J. F. Beacom, (2012), arXiv:1209.0225.

[48] L. Zhang, G. Sigl, and J. Redondo, JCAP **0909**, 012 (2009), arXiv:0905.4952.

[49] L. Zhang, C. Weniger, L. Maccione, J. Redondo, and G. Sigl, (2009), arXiv:0912.4504.

[50] J. F. Beacom, N. F. Bell, and G. D. Mack, Phys.Rev.Lett. **99**, 231301 (2007), arXiv:astro-ph/0608090.

[51] H. Yuksel, S. Horiuchi, J. F. Beacom, and S. Ando, Phys. Rev. **D76**, 123506 (2007), arXiv:0707.0196.

[52] N. F. Bell and T. D. Jacques, Phys. Rev. **D79**, 043507 (2009), arXiv:0811.0821.

[53] M. Cirelli, P. Panci, and P. D. Serpico, (2009), arXiv:0912.0663.

[54] The Fermi-LAT Collaboration, (2010), arXiv:1002.2239.

[55] G. D. Mack, T. D. Jacques, J. F. Beacom, N. F. Bell, and H. Yuksel, Phys.Rev. **D78**, 063542 (2008), arXiv:0803.0157.

[56] R. M. Crocker, N. F. Bell, C. Balazs, and D. I. Jones, (2010), arXiv:1002.0229.

[57] H. Yuksel, J. F. Beacom, and C. R. Watson, Phys.Rev.Lett. **101**, 121301 (2008), arXiv:0706.4084.

[58] S. Palomares-Ruiz, Phys. Lett. **B665**, 50 (2008), arXiv:0712.1937.

[59] M. Cirelli, E. Moulin, P. Panci, P. D. Serpico, and A. Viana, Phys.Rev. **D86**, 083506 (2012), arXiv:1205.5283.

[60] XENON Collaboration, L. Baudis, (2012), arXiv:1203.1589.

[61] M. Drees and M. Nojiri, Phys.Rev. **D48**, 3483 (1993), arXiv:hep-ph/9307208.

[62] J. Engel, Phys.Lett. **B264**, 114 (1991).

[63] M. Ressell *et al.*, Phys.Rev. **D48**, 5519 (1993).

[64] J. R. Ellis, A. Ferstl, and K. A. Olive, Space Sci.Rev. **100**, 235 (2002), arXiv:hep-ph/0106148.

[65] ZEPLIN-III Collaboration, T. Sumner, p. 882 (2009).

[66] LUX Collaboration, D. Akerib *et al.*, (2012), arXiv:1210.4569.

[67] CDMS and SuperCDMS Collaborations, W. Rau, J.Phys.Conf.Ser. **375**, 012005 (2012).

[68] CoGeNT Collaboration, C. Aalseth *et al.*, (2012), arXiv:1208.5737.

[69] EDELWEISS Collaboration, G. Gerbier, p. 125 (2010), arXiv:1012.2260.

[70] R. Bernabei *et al.*, J.Phys.Conf.Ser. **375**, 012002 (2012).

[71] R. Strauss *et al.*, p. 11 (2011).

[72] S. P. Martin, (1997).

[73] G. Belanger, M. Heikinheimo, and V. Sanz, (2012), arXiv:1205.1463.

[74] CMS Collaboration, (2012), CMS-PAS-SUS-11-016.

[75] G. D. Kribs and A. Martin, (2012), arXiv:1203.4821.

[76] H. K. Dreiner and M. K. J. Tattersall, (2012), arXiv:1207.1613.

[77] C. Beskidt, W. de Boer, D. Kazakov, and F. Ratnikov, (2012), arXiv:1207.3185.

[78] A. Rajaraman, W. Shepherd, T. M. Tait, and A. M. Wijangco, Phys.Rev. **D84**, 095013 (2011), arXiv:1108.1196.

[79] P. J. Fox, R. Harnik, J. Kopp, and Y. Tsai, Phys.Rev. **D85**, 056011 (2012), arXiv:1109.4398, 22 pages, 10 figures.

[80] M. Beltran, D. Hooper, E. W. Kolb, Z. A. Krusberg, and T. M. Tait, JHEP **1009**, 037 (2010), arXiv:1002.4137.

[81] I. M. Shoemaker and L. Vecchi, Phys.Rev. **D86**, 015023 (2012), arXiv:1112.5457.

[82] ATLAS Collaboration, G. Aad *et al.*, Phys.Lett. **B705**, 294 (2011), arXiv:1106.5327.

[83] CMS Collaboration, S. Chatrchyan *et al.*, (2012), arXiv:1204.0821.

[84] CMS Collaboration, S. Chatrchyan *et al.*, (2012), arXiv:1206.5663.

[85] ATLAS Collaboration, M. Martinez and f. t. A. Collaboration, EPJ Web Conf. **28**, 12015 (2012), arXiv:1202.0158.

[86] K. Hagiwara, D. Marfatia, T. Yamada, D. Marfatia, and T. Yamada, AIP Conf.Proc. **1467**, 302 (2012), arXiv:1207.6857.

[87] U. Haisch, F. Kahlhoefer, and J. Unwin, (2012), arXiv:1208.4605.

[88] A. Friedland, M. L. Graesser, I. M. Shoemaker, and L. Vecchi, Phys.Lett. **B714**, 267 (2012), arXiv:1111.5331.

[89] CMS Collaboration, S. A. Malik and f. t. C. Collaboration, (2012), arXiv:1206.0753.

[90] CDF Collaboration, T. Aaltonen *et al.*, Phys.Rev.Lett. **101**, 181602 (2008), arXiv:0807.3132.

[91] M. T. Frandsen, F. Kahlhoefer, A. Preston, S. Sarkar, and K. Schmidt-Hoberg, (2012), arXiv:1204.3839.

[92] Y. Bai and T. M. Tait, (2012), arXiv:1208.4361.

[93] N. F. Bell *et al.*, (2012), arXiv:1209.0231.

[94] P. Gondolo and G. Gelmini, Nucl. Phys. **B360**, 145 (1991).

[95] G. Steigman, B. Dasgupta, and J. F. Beacom, (2012), arXiv:1204.3622.

[96] J. Edsjo and P. Gondolo, Phys.Rev **D56**, 1879.

[97] J. Diemand, M. Kuhlen, and P. Madau, Astrophys. J. **657**, 262 (2007), arXiv:astro-ph/0611370.

[98] J. F. Navarro *et al.*, Mon. Not. Roy. Astron. Soc. **349**, 1039 (2004), arXiv:astro-ph/0311231.

[99] G. Gentile, P. Salucci, U. Klein, D. Vergani, and P. Kalberla, Mon. Not. Roy. Astron. Soc. **351**, 903 (2004), arXiv:astro-ph/0403154.

[100] P. Salucci *et al.*, Mon. Not. Roy. Astron. Soc. **378**, 41 (2007), arXiv:astro-ph/0703115.

[101] G. Gilmore *et al.*, Nucl. Phys. Proc. Suppl. **173**, 15 (2007), arXiv:astro-ph/0608528.

[102] G. Gilmore *et al.*, Astrophys. J. **663**, 948 (2007), arXiv:astro-ph/0703308.

[103] G. Gilmore *et al.*, (2008), arXiv:0804.1919.

[104] R. F. G. Wyse and G. Gilmore, (2007), arXiv:0708.1492.

[105] F. Governato *et al.*, Astrophys. J. **607**, 688 (2004), arXiv:astro-ph/0207044.

[106] A. A. Klypin, A. V. Kravtsov, O. Valenzuela, and F. Prada, Astrophys. J. **522**, 82 (1999), arXiv:astro-ph/9901240.

[107] N. Metcalfe, T. Shanks, A. Campos, H. J. McCracken, and R. Fong, Mon. Not. Roy. Astron. Soc. **323**, 795 (2001), arXiv:astro-ph/0010153.

[108] P. J. E. Peebles, Astrophys. J. **557**, 495 (2001), arXiv:astro-ph/0101127.

[109] J. Sommer-Larsen and A. Dolgov, Astrophys. J. **551**, 608 (2001), arXiv:astro-ph/9912166.

[110] A. V. Tikhonov, S. Gottloeber, G. Yepes, and Y. Hoffman, (2009), arXiv:0904.0175.

[111] J. D. Simon and M. Geha, Astrophys. J. **670**, 313 (2007), arXiv:0706.0516.

[112] G. Kauffmann, S. D. White, and B. Guiderdoni, Mon.Not.Roy.Astron.Soc. **264**, 201 (1993).

[113] E. D'Onghia, V. Springel, L. Hernquist, and D. Keres, Astrophys. J. **709**, 1138 (2010), arXiv:0907.3482.

[114] A. Schneider, L. Krauss, and B. Moore, Phys. Rev. **D82**, 063525 (2010), arXiv:1004.5432.

[115] D. P. Finkbeiner and N. Weiner, Phys. Rev. **D76**, 083519 (2007), arXiv:astro-ph/0702587.

[116] N. Arkani-Hamed, D. P. Finkbeiner, T. R. Slatyer, and N. Weiner, Phys. Rev. **D79**, 015014 (2009), arXiv:0810.0713.

[117] D. Tucker-Smith and N. Weiner, Phys. Rev. **D64**, 043502 (2001), arXiv:hep-ph/0101138.

[118] S. Chang, G. D. Kribs, D. Tucker-Smith, and N. Weiner, Phys. Rev. **D79**, 043513 (2009), arXiv:0807.2250.

[119] K. M. Zurek, Phys. Rev. **D79**, 115002 (2009), arXiv:0811.4429.

[120] D. Feldman, Z. Liu, P. Nath, and G. Peim, Phys. Rev. **D81**, 095017 (2010), arXiv:1004.0649.

[121] S. Profumo, K. Sigurdson, and L. Ubaldi, JCAP **0912**, 016 (2009), arXiv:0907.4374.

[122] J. M. Cline, A. R. Frey, and F. Chen, (2010), arXiv:1008.1784.

[123] F. Borzumati, T. Bringmann, and P. Ullio, Phys.Rev. **D77**, 063514 (2008), arXiv:hep-ph/0701007.

[124] J. A. R. Cembranos, J. L. Feng, A. Rajaraman, and F. Takayama, Phys. Rev. Lett. **95**, 181301 (2005), arXiv:hep-ph/0507150.

[125] M. Kaplinghat, Phys. Rev. **D72**, 063510 (2005), arXiv:astro-ph/0507300.

[126] F. J. Sanchez-Salcedo, Astrophys. J. **591**, L107 (2003), arXiv:astro-ph/0305496.

[127] A. H. G. Peter and A. J. Benson, (2010), arXiv:1009.1912.

[128] M.-Y. Wang and A. R. Zentner, (2010), arXiv:1011.2774.

[129] Super-Kamiokande, Y. Ashie *et al.*, Phys. Rev. **D71**, 112005 (2005), arXiv:hep-ex/0501064.

[130] Frejus., K. Daum *et al.*, Z. Phys. **C66**, 417 (1995).

[131] The AMANDA Collaboration, J. Ahrens *et al.*, Phys. Rev. **D66**, 012005 (2002), arXiv:astro-ph/0205109.

[132] The IceCube Collaboration, (2007), arXiv:0711.0353.

[133] MACRO, M. Ambrosio *et al.*, Eur. Phys. J. **C36**, 323 (2004).

[134] Soudan-2, W. W. M. Allison *et al.*, Phys. Rev. **D72**, 052005 (2005), arXiv:hep-ex/0507068.

[135] G. Battistoni, A. Ferrari, T. Montaruli, and P. R. Sala, Astroparticle Physics **19**, 269 (2003).

[136] G. Battistoni, A. Ferrari, T. Montaruli, and P. R. Sala, (2003), arXiv:hep-ph/0305208.

[137] Super-Kamiokande, M. Malek *et al.*, Phys. Rev. Lett. **90**, 061101 (2003), arXiv:hep-ex/0209028.

[138] J. Knodlseder *et al.*, Astron. Astrophys. **441**, 513 (2005), arXiv:astro-ph/0506026.

[139] ATLAS Collaboration, G. Aad *et al.*, Phys.Lett. **B716**, 1 (2012), arXiv:1207.7214.

[140] CMS Collaboration, S. Chatrchyan *et al.*, Phys.Lett. **B716**, 30 (2012), arXiv:1207.7235.

[141] A. Djouadi, Phys. Rept. **459**, 1 (2008), arXiv:hep-ph/0503173.

[142] J. R. Ellis, M. K. Gaillard, and D. V. Nanopoulos, Nucl. Phys. **B106**, 292 (1976).

[143] J. L. Feng, M. Kaplinghat, and H.-B. Yu, (2010), arXiv:1005.4678.

[144] S. Cassel, (2009), arXiv:0903.5307.

[145] T. R. Slatyer, JCAP **1002**, 028 (2010), arXiv:0910.5713.

[146] R. R. Parwani, Phys. Rev. **D45**, 4695 (1992), arXiv:hep-ph/9204216.

[147] L. Dolan and R. Jackiw, Phys. Rev. **D9**, 3320 (1974).

[148] H. A. Weldon, Phys. Rev. **D28**, 2007 (1983).

[149] D. P. Finkbeiner, N. Padmanabhan, and N. Weiner, Phys. Rev. **D78**, 063530 (2008), arXiv:0805.3531.

[150] M. Fukugita and T. Yanagida, Berlin, Germany: Springer (2003) 593 p.

[151] L. Bergstrom, Phys.Lett. **B225**, 372 (1989).

[152] R. Flores, K. A. Olive, and S. Rudaz, Phys.Lett. **B232**, 377 (1989).

[153] E. Baltz and L. Bergstrom, Phys.Rev. **D67**, 043516 (2003), arXiv:hep-ph/0211325.

[154] T. Bringmann, L. Bergstrom, and J. Edsjo, JHEP **0801**, 049 (2008), arXiv:0710.3169.

[155] L. Bergstrom, T. Bringmann, and J. Edsjo, Phys.Rev. **D78**, 103520 (2008), arXiv:0808.3725.

[156] V. Barger, Y. Gao, W. Y. Keung, and D. Marfatia, Phys.Rev. **D80**, 063537 (2009), arXiv:0906.3009.

[157] Q.-H. Cao, E. Ma, and G. Shaughnessy, Phys.Lett. **B673**, 152 (2009), arXiv:0901.1334.

[158] E. Ma, Phys.Rev.Lett. **86**, 2502 (2001), arXiv:hep-ph/0011121.

[159] H. Goldberg, Phys.Rev.Lett. **50**, 1419 (1983).

[160] N. F. Bell, J. B. Dent, T. D. Jacques, and T. J. Weiler, Phys.Rev. **D83**, 013001 (2011), arXiv:1009.2584.

[161] V. Berezinsky, M. Kachelriess, and S. Ostapchenko, Phys.Rev.Lett. **89**, 171802 (2002), arXiv:hep-ph/0205218.

[162] M. Kachelriess and P. Serpico, Phys.Rev. **D76**, 063516 (2007), arXiv:0707.0209.

[163] N. F. Bell, J. B. Dent, T. D. Jacques, and T. J. Weiler, Phys.Rev. **D78**, 083540 (2008), arXiv:0805.3423.

[164] J. B. Dent, R. J. Scherrer, and T. J. Weiler, Phys.Rev. **D78**, 063509 (2008), arXiv:0806.0370.

[165] M. Kachelriess, P. Serpico, and M. A. Solberg, Phys.Rev. **D80**, 123533 (2009), arXiv:0911.0001.

[166] P. Ciafaloni and A. Urbano, Phys.Rev. **D82**, 043512 (2010), arXiv:1001.3950.

[167] P. Ciafaloni *et al.*, JCAP **1103**, 019 (2011), arXiv:1009.0224.

[168] N. F. Bell, J. B. Dent, T. D. Jacques, and T. J. Weiler, Phys.Rev. **D84**, 103517 (2011), arXiv:1101.3357.

[169] H. E. Haber and G. L. Kane, Phys.Rept. **117**, 75 (1985).

[170] J. M. Cornwall, D. N. Levin, and G. Tiktopoulos, Phys.Rev. **D10**, 1145 (1974).

[171] C. Vayonakis, Lett.Nuovo Cim. **17**, 383 (1976).

[172] B. W. Lee, C. Quigg, and H. Thacker, Phys.Rev. **D16**, 1519 (1977).

[173] P. Ciafaloni *et al.*, JCAP **1106**, 018 (2011), arXiv:1104.2996.

[174] N. F. Bell *et al.*, Phys.Lett. **B706**, 6 (2011), arXiv:1104.3823.

[175] M. Garny, A. Ibarra, and S. Vogl, JCAP **1107**, 028 (2011), arXiv:1105.5367.

[176] P. Ciafaloni, D. Comelli, A. De Simone, A. Riotto, and A. Urbano, JCAP **1206**, 016 (2012), arXiv:1202.0692.

[177] M. Garny, A. Ibarra, and S. Vogl, JCAP **1204**, 033 (2012), arXiv:1112.5155.

[178] P. Ciafaloni *et al.*, JCAP **1110**, 034 (2011), arXiv:1107.4453.

[179] V. Barger, W.-Y. Keung, and D. Marfatia, Phys.Lett. **B707**, 385 (2012), arXiv:1111.4523.

[180] N. Baro, M. Beneke, M. Kramer, and M. Rummel, PoS **IDM2010**, 059 (2011).

[181] N. F. Bell, A. J. Brennan, and T. D. Jacques, (2012), arXiv:1206.2977.

[182] J. Alwall, M. Herquet, F. Maltoni, O. Mattelaer, and T. Stelzer, JHEP **1106**, 128 (2011), arXiv:1106.0522.

[183] T. Sjostrand, S. Mrenna, and P. Z. Skands, Comput.Phys.Commun. **178**, 852 (2008), arXiv:0710.3820.

[184] S. Ovyn, X. Rouby, and V. Lemaitre, (2009), arXiv:0903.2225, 36 pages, 13 figures, 7 tables. Corrected typos. Submitted to Comp. Phys. Comm.

[185] T. Binoth, N. Kauer, and P. Mertsch, p. 142 (2008), arXiv:0807.0024.

[186] N. D. Christensen and C. Duhr, Comput.Phys.Commun. **180**, 1614 (2009), arXiv:0806.4194.

[187] H.-L. Lai *et al.*, Phys.Rev. **D82**, 054021 (2010), arXiv:1004.4624.

[188] G. Belanger *et al.*, Comput.Phys.Commun. **182**, 842 (2011), arXiv:1004.1092, 24 pages, 6 figures, typos corrected, acknowledgements modified.